AD-A108 032 MONTANA STATE UNIV BOZEMAN DEPT OF CIVIL ENGINEERING--ETC F/G 8/12
AN INVESTIGATION OF THE HIGH RATE VOLUMETRIC PROPERTIES OF SNOW--ETC(U)
NOV 81 R L BROWN DAAG29-78-G-0089
UNCLASSIFIED ARO-15413.9-GS NL

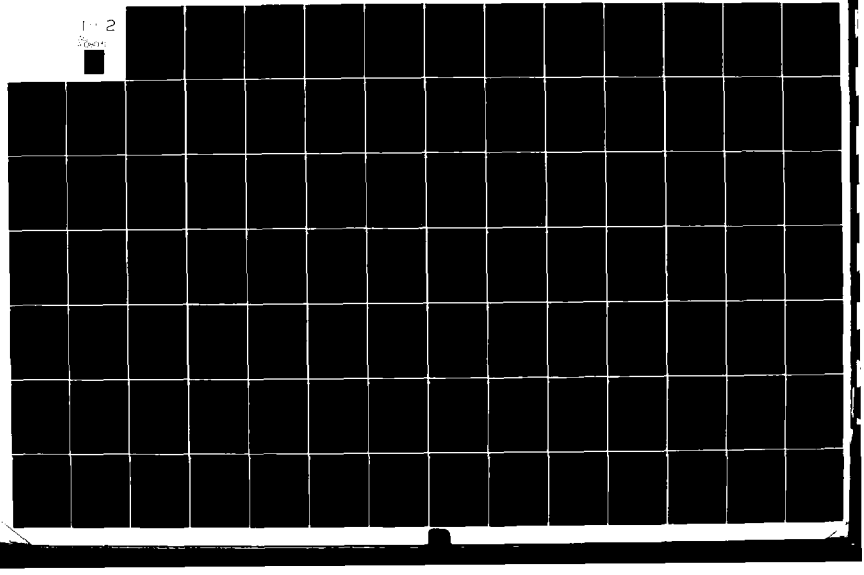

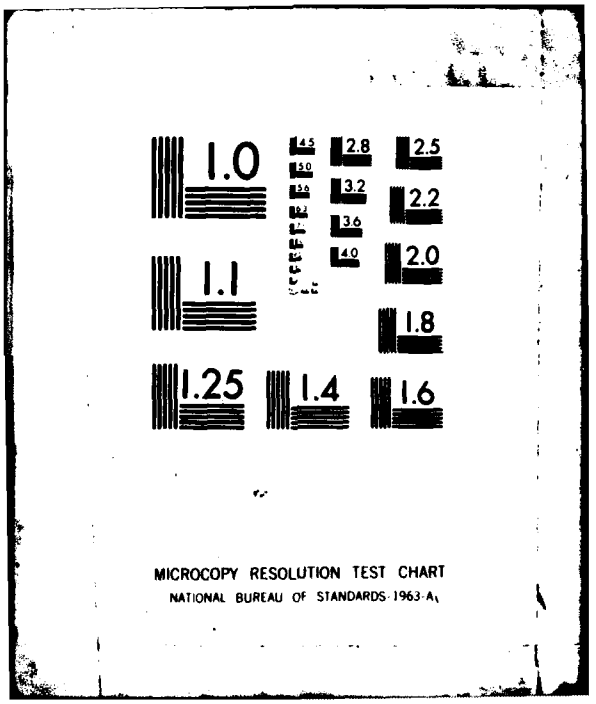
1.0
1.1
1.25
1.4
1.6
1.8
2.0
2.2
2.5
2.8
3.2
3.6
4.0
4.5
5.0
MICROCOPY RESOLUTION TEST CHART
NATIONAL BUREAU OF STANDARDS-1963-A

AD A108032

SECURITY CLASSIFICATION OF THIS PAGE (When Data Entered)

REPORT DOCUMENTATION PAGE	READ INSTRUCTIONS BEFORE COMPLETING FORM
1. REPORT NUMBER: 15413.9-GS	2. GOVT ACCESSION NO: AD-A108 032	3. RECIPIENT'S CATALOG NUMBER
4. TITLE (and Subtitle): An Investigation of the High Rate Volumetric Properties of Snow	5. TYPE OF REPORT & PERIOD COVERED: Final Report: 1 May 78 - 31 Oct 81
	6. PERFORMING ORG. REPORT NUMBER
7. AUTHOR(s): R. L. Brown	8. CONTRACT OR GRANT NUMBER(s): DAAG29 78 G 0089
9. PERFORMING ORGANIZATION NAME AND ADDRESS: Montana State University, Bozeman, MT 59717	10. PROGRAM ELEMENT, PROJECT, TASK AREA & WORK UNIT NUMBERS
11. CONTROLLING OFFICE NAME AND ADDRESS: U. S. Army Research Office, Post Office Box 12211, Research Triangle Park, NC 27709	12. REPORT DATE: Nov 81
	13. NUMBER OF PAGES: 155
14. MONITORING AGENCY NAME & ADDRESS(if different from Controlling Office)	15. SECURITY CLASS. (of this report): Unclassified
	15a. DECLASSIFICATION/DOWNGRADING SCHEDULE

LEVEL II

16. DISTRIBUTION STATEMENT (of this Report)

Approved for public release; distribution unlimited.

DTIC ELECTE DEC 1 1981 S H

17. DISTRIBUTION STATEMENT (of the abstract entered in Block 20, if different from Report)

NA

18. SUPPLEMENTARY NOTES

The view, opinions, and/or findings contained in this report are those of the author(s) and should not be construed as an official Department of the Army position, policy, or decision, unless so designated by other documentation.

19. KEY WORDS (Continue on reverse side if necessary and identify by block number)

20. ABSTRACT (Continue on reverse side if necessary and identify by block number)

In this report, the constitutive behavior of dry snow is analyzed and described mathematically by means of two microdynamical models. These are then evaluated by means of previous experimental data. A number of applications are then investigated. These applications include vehicle mobility in shallow and deep snowpack, steady shockwaves, and nonsteady shockwaves.

DTIC FILE COPY

DD FORM 1 JAN 73 1473 EDITION OF 1 NOV 65 IS OBSOLETE

UNCLASSIFIED

SECURITY CLASSIFICATION OF THIS PAGE (When Data Entered)

FINAL REPORT

AN INVESTIGATION OF THE HIGH RATE VOLUMETRIC PROPERTIES OF SNOW

BY

R. L. Brown*

Prepared for the U. S. Army Research Office,
Research Triangle Park, as the final
report for Grant No. DRXRO-RR-P15413-GS.

DTIC
ELECTE
DEC 1 1981
S D
H

*Professor, CE&EM Department, Montana State University, Bozeman, MT 59717

395384

ABSTRACT

Reported here are the results of a three year study of the high rate volumetric Properties of Snow. In addition to the report presented here, the project resulted with over ten publications (Brown 1979-1981, Bowles 1981, Rosé, 1981) which are included in the list of references. The constitutive behavior of dry snow is analyzed and described mathematically by means of two microdynamical models. These are then evaluated by means of previous experimental data. A number of applications are then investigated. These applications include vehicle mobility in shallow and deep snowpack, steady shockwaves, and nonsteady shockwaves. Finally, an electromagnetic stress wave generator was designed, constructed and used in a shockwave testing program on snow. Experimental results are presented and discussed.

ACKNOWLEDGEMENT: The work reported here was funded by Army Research Office Grant No. DRXRO-RR-P15413-GS. The author expresses his appreciation to the Army Research Office for its support. Special thanks is extended to Dr. Steve Mock of ARO for his encouragement and cooperation on all aspects of the grant.

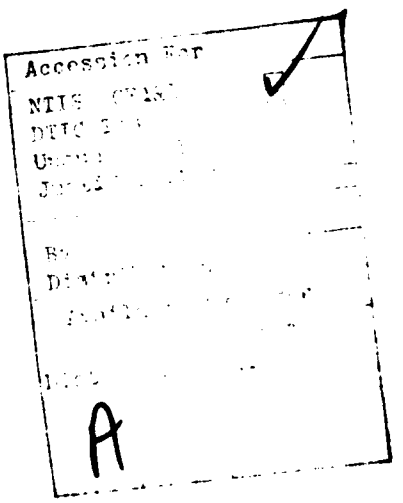

TABLE OF CONTENTS

Topic		Page
I.	INTRODUCTION	1
II.	HIGH RATE VOLUMETRIC PROPERTIES OF SNOW	7
	II.A. A Material Representation of ICE	8
	II.B. Development of Volumetric Constitutive Law for Pore Collapse Model	13
	II.C. Comparison with Experimental Data for Pore Collapse Model	23
	II.D. Development of Constitutive Law for Neck Growth Model	32
	II.E. Comparison with Experimental Data for Neck Growth Model	40
	II.F. Simplified Equation for Neck Growth Model	43
III.	APPLICATION TO PROBLEM OF VEHICLE MOBILITY	48
	III.A. Introductory Remarks	48
	III.B. Tracked Vehicle Mobility in Shallow Snowpack of Medium Density	50
	III.C. Tracked Vehicle Mobility in Deep Snowpack of Medium Density	61
	III.D. Vehicle Performance Under Different Snowpack Conditions	78
IV.	APPLICATION TO SHOCKWAVE PROPAGATION	88
	IV.A. Introductory Remarks	88
	IV.B. Governing Equations for Plane Shockwaves	90
	IV.C. Steady Shockwaves in Snow	94
	IV.D. Nonsteady Shockwaves	113
	IV.E. The Use of Jump Equations for Analyzing Nonsteady Shockwave Propagation	123
V.	EXPERIMENTAL PROGRAM ON STRESSWAVES IN SNOW	138
	V.A. Electromagnetic Theory	141
	V.B. Assessment of Generator Performance	142
	V.C. Test Results with the Electromagnetic stress Wave Generator	144
VI.	CONCLUSIONS	152
VII.	REFERENCES	153

I. INTRODUCTION

This report is concerned primarily with the high strain rate volumetric properties of snow. This work was originally oriented toward the analysis of shockwaves in snow, but as the project progressed, it became apparent that the study would have to include a major effort to evaluate the volumetric properties of snow. This property of snow must be known before a number of probems involving snow can be studied.

The mechanical properties of snow have been under active investigation for over forty years. Mellor (1974, 1977) has made thorough reviews of past investigative work on the properties of snow. Salm (1981) has recently made a more up to date review and has described the current state of the art.

Early work (1940-1960) was directed at evaluating the linear properties of snow. Work typical of this period includes work by Kinosita (1967). Later work by Lee (1961,1963), and Salm (1974) extended the earlier work on the linear properties of snow. Most of this work concentrated on the linear viscoelastic properties. At low enough strain rates, say at rates less than $10^{-7}s^{-1}$, snow does exhibit linear properties, although the deformation is generally inelastic. Most linear constitutive relations used to describe the behavior of snow have the forms

$$\underset{\sim}{T} = 2\int_{-\infty}^{t} G(t-\tau)\,\dot{\underset{\sim}{D}}(\tau)d\tau + \int_{-\infty}^{t} \lambda(t-\tau)\underset{\sim}{1}\,\mathrm{tr}\,\dot{\underset{\sim}{E}}(\tau)d\tau \qquad (I.1)$$

where $\underset{\sim}{T}$ is the stress tensor, $\underset{\sim}{E}$ is the strain tensor and G and λ are respectively the shear and volumetric relaxation moduli. The above equation can be inverted to describe the strain in terms of the history of the stress. These forms of the constitutive laws are valid only so long as the material behaves as a linear viscoelastic material. Figure 1 shows the typical uniaxial rate of

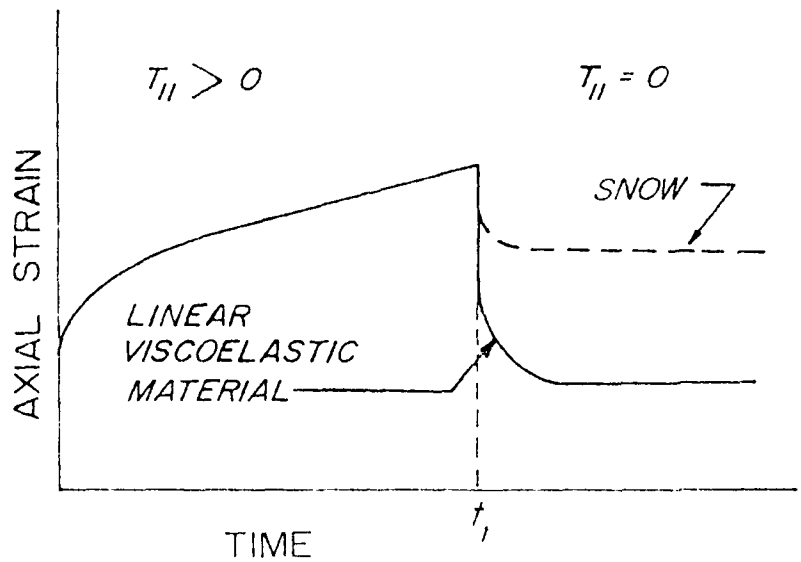

(a) CREEP TEST

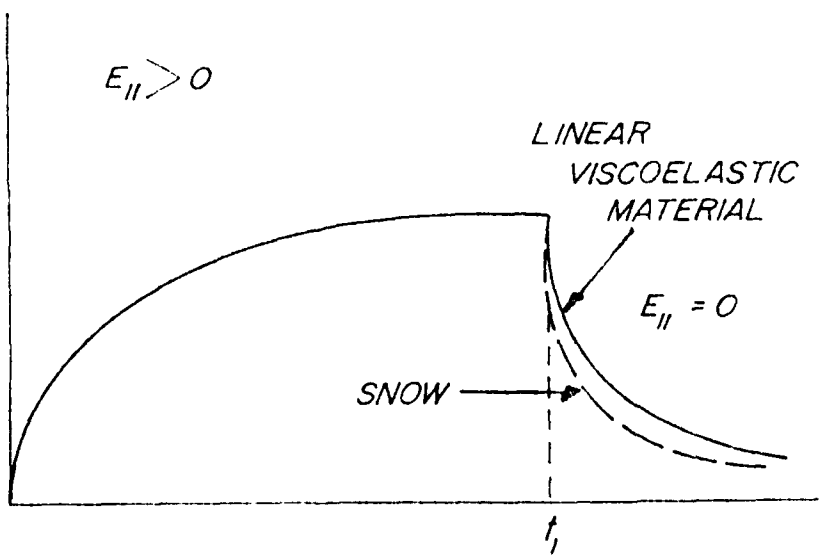

(b) DEFORMATION – RATE TEST

Figure 1. Typical test curves for snow and linear viscoelastic materials.

deformation and creep response curves that result with linear viscoelastic materials. This is shown in the case of solid lines. Actual response curves for snow are shown with the broken lines. In order for a material to be truly viscoelastic, the creep curve must show the characteristics of the solid line. For instance, in Figure 1(a), the creep curve consists of two parts. The first part represents the strains which develop when the constant axial stress T_{11} is applied. The second part represents the recovery which occurs when the load is released. A viscoelastic rebound which equals the initial elastic strain occurs immediately upon load application.

Snow does not show this true viscoelastic behavior. The strongest evidence of this is demonstrated in the creep curve when the stress is released. In the case of snow, the instantaneous elastic response may be but a small fraction of the initial elastic strain. Aside from this case the creep and deformation rate tests do not readily show this particular behavior. In particular the deformation rate tests do not show any significant differences between the behavior of snow and that of a linear viscoelastic material. By observing the deformation rate tests, one may erroneously conclude that snow is indeed a linear viscolastic material. The rate curves shown in Figure 1 consists of two parts. The first part of the curve shows the buildup of stress as the material is subjected to a constant uniaxial strain rate, whereas the second part gives the relaxation of stress after the strain rate is stopped and maintained at a constant value. Some differences do emerge in the relaxation curves, but generally it is not very significant.

The actual behavior of snow exhibits some characteristics of an elastic-viscoplastic material, since some of the initial elastic response when loaded is gradually dissipated away. However, snow does also exhibit some very definite viscoelastic characteristics. This makes snow a difficult material to model

with a single constitutive equation even in the small strain-low strain-rate region. As a matter of pragmatism, most past investigators have chosen to model snow with a linear viscoelastic representation similar to that of Eq. (1). For most applications, such representations have been found to be acceptable.

The above is seen to be particularly true when one considers other problems with characterizing snow properties. Snow is a highly variable material. Its properties change drastically with temperature, density, and the effects of temperature gradient metamorphism. Such properties as fracture stress and compliance can go through an order of magnitude variation, and correctly defining these properties is quite difficult.

When finite strains or large strain rates ($|E| \geq 10^{-1}$, $|\dot{E}| \geq 10^{-1}$) are involved, snow exhibits definite nonlinear properties. Salm (1974), Brown et al (1973, 1974, 1977), Desrues and others (1981) have characterized these properties. Salm considered primarily the response of snow to uniaxial deformations and subsequently developed a nonlinear viscoelastic model. Brown's later work was essentially a thermodynamic formulation in which compression, tension and shear test data was used to develop a three dimensional constitutive equation for snow. This formulation was shown to be quite accurate for a wide range of deformation conditions. However, the constitutive equation was complicated and cumbersome. Therefore the applicability to engineering problems is limited. Desrues and others have recently formulated an incremental constitutive equation, and this work should show good promise for solving some important engineering problems.

The above nonlinear formulations are still quite limited in the range of strain rates for which they are valid. All of the theories incur rather large errors for strain rates above $10^{-4}s^{-1}$. Under tension and shear these strain rates cause

fracture (Brown, 1974, 1977), but under some compressive deformations, sustained loading can be applied to snow without causing fracture.

There are a large number of problems in which the above discussed constitutive equations do not apply. This includes deformations which produce extremely high strain rates ($|\dot{\underset{\sim}{E}}| \geq 10^{-4} s^{-1}$) and large strains ($|\underset{\sim}{E}| \geq 0.2$). Problems involving shockwaves, vehicle travel, projectile impact or penetration, among others are examples of such situations. For instance vehicles traveling over a low density snowpack can produce strain rates in excess of $10\ s^{-1}$ and increases in density of 100%. Harrison (1981) reports on vehicle mobility studies of tracked vehicles in snowpack. In instances where little vehicle slippage occurs, the deformation of the snow under the track is largely volumetric, and this problem can be analyzed with a relatively simple volumetric constitutive law (Brown 1979, 1981a, 1981b). In cases where the vehicle incurs significant slippage, then a multiaxial constitutive law is needed.

Explosives are used to initiate avalanches in recreational areas and along highways exposed to steep open slopes. These explosives produce intense, high frequency shockwaves which propagate into the snowpack. Depending on the explosive speed, snowpack properties and placement, the shockwave spreads and attenuates. Strain rates on the order of $10^{5} s^{-1}$ and volumetric strains as large as 200% can be induced. In order to analyze these problems, very specialized constitutive relations are required.

The military is also concerned about several problems concerning impact loading of snow. These include fuse action, ballistic penetration, and effectiveness of artillery explosives in snow. For instance, artillery fuses which work well in mud fail to detonate properly in snow. Also rifle fire has been shown to penetrate much less deeply into snowpack then origin-

ally thought. The unique properties of snow are responsible for these surprising results.

Prior to the results reported here and the papers published by the author (Brown 1979-81), many of these problems could not be analyzed analytically. In order to do so, appropriate constitutive relations are needed. This report brings together the work of the author on the high rate volumetric properties of snow. Also included are applications to several problems. Finally recommendations to further work are also given.

The work reported here concerns only the high rate volumetric properties of snow. Deviatoric properties are not considered here. The reason for this is that very little is known about the high rate properties of snow, and a good starting point would be volumetric properties. In addition some important problems can be studied if only the volumetric properties are known. Once the volumetric properties are known, it is felt that these results can be used to help evaluate the deviatoric properties. A complete multiaxial constitutive equation is necessarily qute complicated, and it would appear to be best to approch this development in a systematic manner.

II. HIGH RATE VOLUMETRIC PROPERTIES OF SNOW

Practially all of the previous work cited in the introduction used purely phenomonalogical methods of characterizing snow. This method uses creep data or deformation rate data to determine material coefficients in the constitutive equation chosen to represent the material. The form of the constitutive equation is chosen after the test data is observed to determine if the material is elastic, viscoelastic, linear, nonlinear, etc. In this approach, little or no concern is given to the microstructural deformation processes and their effect on the properties of the material.

One reason that the phenomonalogical approach is used so much is that it is a relatively straight forward method. Curve fitting techniques such as the linear and nonlinear least squares methods are commonly used in conjunction with statistical analysis to determine just how well a constitutive equation works. This approach is very straight forward for elastic and linear viscoelastic materials, but for elastic-viscoplastic materials this approach can become much more difficult, since very intricate mathematical models (Brown, 1977) must be used.

More recently Brown (1979, 1980), and St. Lawrence (1977) have utilized microdynamical models to formulate constitutive theories for snow. This approach considers deformation mechanisms at the crystalline level which are important in determining the macroscopic behavior. This method of studying the material is justifiable in the sense that the behavior of the parent material (ice) and the deformation mechanisms at the granular level must be responsible for the properties of the granular material. Also this method results with constitutive laws which give much insight into what microstructural changes occur during deformation. Microdynamical approaches would consequently appear to be preferable to phenomenalogical

formulations. However, the microdynamical approach usually yields constitutive relations which are mathematically complicated. In fact these methods have to date not found a lot of engineering use for this very reason. Jenkins (1981), and Brown (1980) are examples of recent work for granular materials such as sand and grain. The next decade should see much progress in this area.

Presented here are two formulations developed by the author. The first method is applicable to medium-to-high density snow, and the second is valid for lower density snow. Both formulations use the microdynamical approach and hence are based on the material properties of ice and the granular texture of the porous material, snow.

II A. A MATERIAL REPRESENTATION OF ICE

Previous studies by Dillon and Andersland (1967) and Hawkes and Mellor (1972) have indicated that polycrystalline ice under uniaxial tension and compression possesses a rate-dependent yield stress. Additional experimental work by Haynes (private communication) has extended the previous work to strain rates in excess of $1.0s^{-1}$. In tension, ice generally fractures at high strain rates, and this critical stress is not strongly rate dependent. However, under compression, the critical stress shows a definite rate dependency, even at the rates studied by Haynes. The present study primarily concerns the compressive properties of ice for intermediate-to-high deformation rates.

Based on the experimental results indicated in Figure 2 (Dillon and Andersland (1967), and Haynes), the following constitutive relation is assumed for polycrystalline ice:

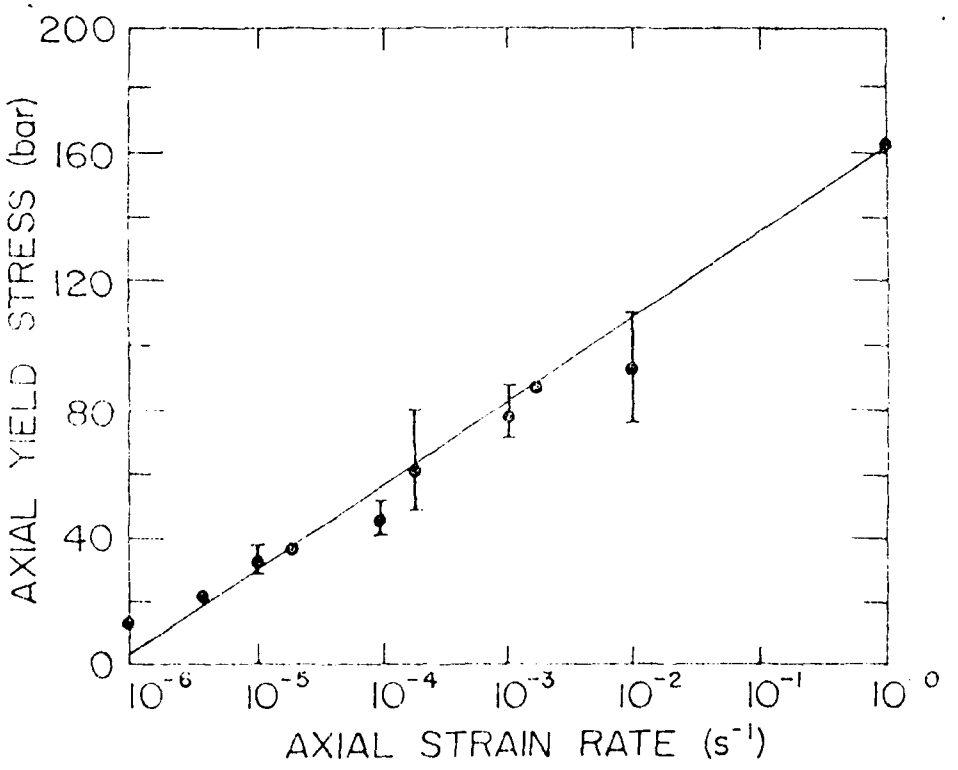

Figure 2. Uniaxial test results for polycrystalline ice.

$$S = 2G\dot{e} \qquad S < Y \tag{II.A.1}$$

$$S = Y \tag{II.A.2}$$

where

$$Y = S_o + C\ln(AD) \qquad AD > 1 \tag{II.A.3}$$

S_o, C, and A are material constants; S, e, and D are the principal difference values of the deviatoric stress tensor, deviatoric strain tensor, and deviatoric rate of deformation tensor. Similar definitions hold for D and e. The matrix material, ice, is assumed to be incompressible, so that the deviatoric values of the strain tensor and the deformation rate tensors equal the total strain and deformation rate tensors.

The above equations are essentially those of an elastic-viscoplastic material, so that the material behaves elastically until a rate-dependent yield condition is reached, whereupon plastic deformation ensues. These equations are somewhat different from Glen's flow law,

$$\tau = C\dot{\gamma}^n \tag{II.A.4}$$

where τ and $\dot{\gamma}$ are, respectively, the shear stress and shear strain rate, C is a material constant and n is a scalar. Equations 2-3 were chosen, since they acquire a straight-line form on Figure 1 and fit the data better than Glen's law. Glen's law does work well at lower strain rates, however, and in many cases is mathematically more tractable than the form of eqs. 2-3.

Consider now a compression test on polycrystalline ice. The only nonzero stress component is σ_{xx}, where the x-direction is the axial direction of the compression test. The deviatoric stress sensor is

$$\underset{\sim}{S} = \underset{\sim}{\sigma} - \frac{1}{3}(\mathrm{tr}\,\underset{\sim}{\sigma})\,\underset{\sim}{1} \tag{II.A.5}$$

where tr implies the trace of the tensor, $\underset{\sim}{1}$ is the identity tensor, and $\underset{\sim}{\sigma}$ is the Cauchy stress tensor. $\underset{\sim}{S}$ therefore has the components

$$s_{ij} = \begin{bmatrix} \frac{2\sigma_{xx}}{3} & 0 & 0 \\ 0 & -\frac{\sigma_{xx}}{3} & 0 \\ 0 & 0 & -\frac{\sigma_{xx}}{3} \end{bmatrix} \qquad \text{(II.A.6)}$$

The rate of deformation tensor is

$$D = \frac{1}{2}\left(\nabla \underline{v} + \nabla \underline{v}^T\right) \qquad \text{(II.A.7)}$$

where ∇ is the gradient operator and $\underline{v}$ is the velocity vector. Since the material is incompressible, the divergence of the velocity field is zero,

$$\nabla \cdot \underline{v} = 0 \qquad \text{(II.A.8)}$$

and it can be shown that D has the components

$$D_{ij} = \begin{bmatrix} \frac{\partial v_x}{\partial x} & 0 & 0 \\ 0 & -\frac{1}{2}\frac{\partial v_x}{\partial x} & 0 \\ 0 & 0 & -\frac{1}{2}\frac{\partial v_x}{\partial x} \end{bmatrix} \qquad \text{(II.A.9)}$$

The principal difference values, S and D, are, respectively,

$$S = \sigma_{xx}$$

$$D = \frac{3}{2}\frac{\partial v_x}{\partial x} \qquad \text{(II.A.10)}$$

In the results reported in Figure 2, strains were all small, so that the axial rate of deformation component D_{xx} is approximately equal to the axial strain rate $\dot{\epsilon}_{xx}$. For uniaxial compression, eq. 2.3 becomes

$$\sigma_{xx} = S_0 + C\ln\left(\frac{3A}{2}D_{xx}\right) \qquad \text{(II.A.11)}$$

By adjusting eq. 11 to fit the compression data represented in Figure 2

$$S_0 = 1\times10^{6}\ \text{N m}^{-2}$$

$$C = 1.16\times10^{6}\ \text{N m}^{-2} \qquad \text{(II.A.12)}$$

$$A = 3.3\times10^{+6}\ \text{s}.$$

As can be seen in Figure 2, this equation represents the test results quite well. There is an appreciable amount of scatter indicated by the vertical lines. This is to be expected, as there may be a good degree of variability in freezing the ice, in forming the specimens, and in testing. However, the average results appear to be well approximated by the constitutive law.

The constitutive law does not involve a work-hardening term. Previous experimental studies on ice by Dillon and Andersland (1962), among others, have not indicated strong work-hardening* characteristics for ice. However, there are no published data on ice involving large strains in excess of several hundred percent. Therefore, it is quite possible that at large strains ice does exhibit work-hardening properties. Such strains certainly do occur during finite compaction of snow, particularly in the very critical grain bonds where massive localized deformations take place. Thus, the constitutive equation finally formulated for snow may have to be empirically adjusted with a work-hardening term.

This problem has also been encountered in the field of powder metallurgy where a porous metal with an elastic, perfectly plastic matrix material shows considerable work-hardening characteristics. Quite possibly the large strains occurring in high stress regions such as grain bonds are of such an order of magnitude that the matrix material does work harden. Also, quite

---

*A work-hardening material is one that stiffens under plastic deformation.

possibly the actual description of the deformation process is incomplete. At any rate, the work-hardening characteristics of porous materials such a powdered aluminum are not predicted by experiments that have been run on the solid Matrix material.

II.B. DEVELOPMENT OF THE VOLUMETRIC CONSTITUTIVE LAW FOR PORE COLLAPSE MODEL

Consider now the deformation of a thick-walled hollow sphere of an incompressible viscoplastic material with the constitutive relation given by eqs. II.A.1 - II.A.3. The geometry is given in Figure 3. The initial internal and external radii of the sphere, a_o and b_o, are chosen so that the correct material porosity results. In this paper, the density ratio is defined as

$$\rho = \frac{\rho_m}{\rho} \tag{II.B.1}$$

where ρ and ρ_m are, respectively, the mass density of the porous material and the matrix material, ice.

Under an external time-dependent pressure loading, the internal and external radii a(t) and b(t) change with time. The deformation is spherically symmetric, so the deformed coordinates of a generic point can be expressed as:

$$\begin{aligned} r &= r(r_o,t) \\ \theta &= \theta_o \\ \phi &= \phi_o \end{aligned} \tag{II.B.2}$$

where r_o, θ_o, ϕ_o are the undeformed spherical coordinate positions, and r, θ, ϕ denote the deformed coordinate positions.

Incompressibility of the matrix material requires the Jacobian of the deformation to equal unity; i.e.

$$\frac{r^2}{r_o^2}\frac{\partial r}{\partial r_o} = 1 \tag{II.B.3}$$

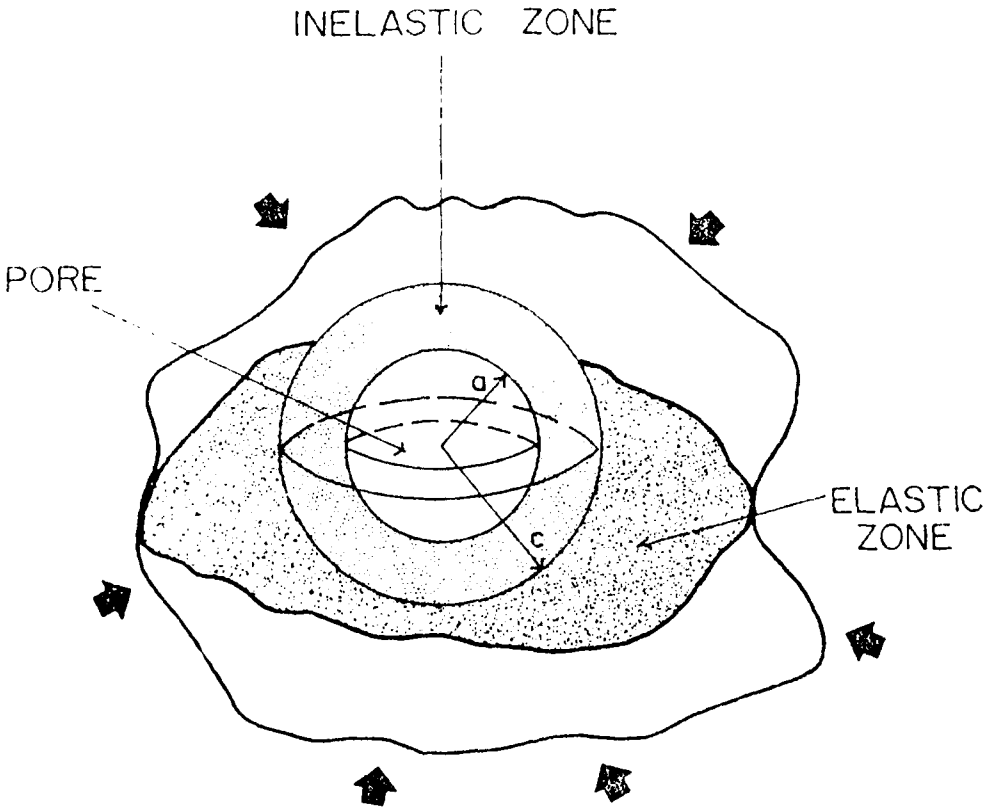

Figure 3. Pore collapse model.

Integration yields

$$r^3 = r_0^3 - B(t) \tag{II.B.4}$$

where B is an unknown function of time. This equation can be differentiated twice. This results in

$$\ddot{r} = -\left(\frac{\dot{B}^2}{r^5} + \frac{\ddot{B}}{3r^2}\right) \tag{II.B.5}$$

for the radial acceleration. The acceleration can be expressed in terms of an acceleration potential $\phi(r,t)$:

$$\ddot{r} = \frac{\partial \phi}{\partial r}. \tag{II.B.6}$$

By doing this, the following can be arrived at for all $a \leq r \leq b$:

$$\phi = \frac{\dot{B}^2}{18r^4} + \frac{\ddot{B}}{3r}. \tag{II.B.7}$$

The above results are strictly of a kinematical nature and depend only on the constraint of material incompressibility. In addition, material incompressibility may be used to arrive at the following relations:

$$c = \frac{b^3}{(b^3-a^3)}, \quad \alpha_0 = b_0^3/(b_0^3-a_0^3) \tag{II.B.8a}$$

$$a^3 = \frac{a_0^3(\alpha-1)}{(\alpha_0-1)}, \quad b^3 = \frac{a_0^3\alpha}{(\alpha_0-1)} \tag{II.B.8b}$$

$$B(t) = \frac{a_0^3(\alpha_0-\alpha)}{(\alpha_0-1)} \tag{II.B.8c}$$

As the external pressure P increases, the deformation proceeds in three distinct phases:

(1) an initial purely elastic phase

(2) an elastic-plastic phase with an elastic/plastic interface at r = c, where $a \leq c \leq b$, and

(3) A fully plastic phase. During the first two phases, the strains are assumed to be small, but during the fully plastic phase, large strains can be incurred. Each phase is now considered separately.

Fully Elastic Phase:

In this phase, the strains are assumed to be infinitesimal. Therefore the three strain components are

$$\epsilon_r = \frac{\partial u}{\partial r}, \quad \epsilon_\theta = \epsilon_\phi = u/r \tag{II.B.9}$$

where u is the radial displacement; and if u is small compared with r, $u = r - r_0$ may be approximated by the expression

$$u = -\frac{b(t)}{3r_0^2} . \tag{II.B.10}$$

For small strains, r_0 differs by a small amount from r; therefore, in this section the distinction will be dropped. The strains become

$$\epsilon_r = \frac{2}{3}\frac{B}{r^3} \tag{II.B.11}$$

$$\epsilon_\theta = \epsilon_\phi = -\frac{B}{3r^3} \tag{II.B.12}$$

Since the material is assumed to be linearly elastic, the constitutive equation acquires the form

$$S_r = 2Ge_r = 4G\,B/(3r^3) \tag{II.B.13a}$$

$$S_\theta = 2Ge_\theta = -2GB/(3r^3) \tag{II.B.13b}$$

$$S_\phi = 2Ge_\phi = -2GB/(3r^3) \tag{II.B.13c}$$

where S_r, S_θ, S_ϕ and e_r, e_θ, e_ϕ are, respectively, the deviatoric stress and deviatoric strain components. Since the material is incompressible, the volumetric strain is zero, and the hydrostatic pressure p cannot be evaluated with the constitutive equation alone.

The radial equation of motion is

$$\frac{\partial \sigma_r}{\partial r} + \frac{2}{r}(\sigma_r - \sigma_\phi) = \rho_m \ddot{r} \qquad \text{(II.B.14)}$$

which may be put in the modified form

$$-\frac{\partial p}{\partial r} = \rho_m \frac{d\dot{r}}{dr} \qquad \text{(II.B.15)}$$

for which the boundary conditions are:

$$p = 0 \qquad r = a \qquad \text{(II.B.16)}$$

$$\sigma_r = -P(t) \qquad r = b. \qquad \text{(II.B.17)}$$

It should be noted that pore pressure is assumed negligible. Under extremely large rates of loading or near low density ratios (say $1 \leq \alpha \leq 1.2$), the wisdom this assumption may be questionable. *This will be discussed in more detail later.* Integration of eq. 15 results in:

$$-p(r,t) = \rho_m \dot{r}(r,t) + h(t) \qquad \text{(II.B.18}$$

where $h(t)$ is a time function. Since $\sigma_r = \sigma_r - p$,

$$\sigma_r = \rho_m \dot{r} + h + 4GB(3r^3). \qquad \text{(II.B.19)}$$

Applying the boundary conditions gives the solution

$$P(t) = \rho_m(\dot{r}_a - \dot{r}_b) + \frac{4GB}{3}\left(\frac{1}{a^2} - \frac{1}{b^2}\right). \qquad \text{(II.B.20)}$$

$\dot{r}$ can then be expressed directly in terms of P(t) by making appropriate use of eqs. 7 and 8. These, combined with eq. 20, yield

$$P(t) = \tau^2 Q(\ddot{\alpha}, \dot{\alpha}, \alpha) + \frac{4G(\alpha_0 - \alpha)}{3\alpha(\alpha - 1)} \qquad \text{(II.B.21)}$$

where

$$\frac{\dot{P}}{\dot{\rho}} = \frac{\dot{P}}{\dot{\rho}_s} = \frac{\alpha^{2/3}}{3(\alpha-1)^{2/3}}$$

$$\left[\frac{\dot{\alpha}}{\alpha}(\alpha-1)^{-1/3} - \frac{\dot{\alpha}}{\alpha}\alpha^{-1/3} \right] \qquad \text{(II.B.22)}$$

$$+ \frac{1}{6}\frac{\dot{J}}{J}(\alpha-1)^{-4/3} - \alpha^{-4/3})$$

Equation 22 describes the material volumetric response to a hydrostatic pressure loading. The term P(t) represents the actual pressure in the matrix material. Carroll and Holt (1972) have shown that the average pressure in the porous material p(t) is approximately

$$p = P/\alpha \qquad \text{(II.B.23)}$$

As long as the material does not yield, eq. 21 describes the time-dependent response of the material.

This equation is the same as Carroll and Holt's (1972) result in their study of porous aluminum.

Plastic-plastic flow:

Equation 19 indicates that the maximum stress occurs at the inner radius. Yielding then initiates there; and, as the pressure P(t) continues to increase, a yield surface, $r = c(t)$, propagates radially outward. The yield condition given by eq. (II.A.3) is reached at a critical pressure P_1 when the principal deviatoric stress difference, $S_r - S_\theta$, reaches the critical value Y, which itself is rate dependent.

Assume now $P > P_1$ and that yielding has propagated out to a radial distance c, $a < c < b$. For $r \leq c$, an inelastic stress state exists, and for $r > c$, the material is elastic. When analyzing the outer elastic zone, the following boundary conditions apply:

$$\sigma_r = -P(t), \quad r = b \qquad \text{(II.B.24)}$$

$$\sigma_r = P_c(t), \quad r = c \tag{II.B.25}$$

$$S_r - S_\theta = \frac{2\sqrt{3}B}{c^3} = Y, \quad r = c. \tag{II.B.26}$$

At the interface of the elastic zone and plastic zone, the stress must satisfy the yield condition. In the yielded zone, eq II.A.3 gives

$$S_r = \frac{2}{3}Y - \frac{2}{3}(S_0 + C \ln AD) \tag{II.B.27}$$

which remains valid as long as the loading is monotonic.

Consider first the yielded zone, where the constitutive law is defined in terms of the deformation rate tensor. The principal rate components are, if v_θ and v_ϕ are zero,

$$D_{rr} = \partial v_r/\partial r \tag{II.B.28}$$

$$D_{\theta\theta} = v_r/r \tag{II.B.29}$$

$$D_{\phi\phi} = v_r/r \tag{II.B.30}$$

The shearing components are zero. Since the deformation is viscous, a Eulerian description can be used here. Incompressibility requires that the divergence of the velocity vector vanish; i.e.,

$$\frac{\partial v_r}{\partial r} + 2\frac{v_r}{r} = 0$$

or

$$\frac{\partial}{\partial r}(v_r r^2) = 0. \tag{II.B.31}$$

This yields

$$v_r = \frac{F(t)}{r^2} \tag{II.B.32}$$

where F is an undetermined time function. Differentiating the above and equating to the acceleration potential results in

$$\psi = -\frac{\dot{F}}{r} + \frac{1}{2}\frac{F^2}{r^4} \tag{II.B.33}$$

Actually F(t) can be related directly to B(t) defined in eq. 3.7, which can be done by differentiating B to obtain

$$\dot{B}(t) = -3F(t) \qquad \text{(II.B.34)}$$

which should be expected, since F and B have been based on the purely kinematical constraint of material incompressibility.

Utilizing the incompressibility constraints in eq. 8 gives

$$F(t) = \frac{a_0^3 \dot{\alpha}}{3(\alpha_0 - 1)} \qquad \text{(II.B.35)}$$

Now consider the radial equation of motion. In terms of the deviatoric stress components,

$$\frac{\partial S_{rr}}{\partial r} + \frac{2}{r}(S_{rr} - S_{\theta\theta}) = \frac{\partial P}{\partial r} = \rho_m \frac{\partial^2 r}{\partial t^2} \qquad \text{(II.B.36)}$$

The principal deviatoric deformation rate difference is

$$D_{rr} - D_{\theta\theta} = -3F/r^3 \qquad \text{(II.B.37)}$$

and the difference $S_{rr} - S_{\theta\theta}$ can easily be seen to have the value Y. Solution of the equation of motion gives

$$P(r) = \frac{2}{3}S_0 + 2S_0 \ln(r/\beta) + C \ln(\beta/r)\left[\frac{2}{3} + \ln(r/\beta)\right] - \rho_m \frac{r^2}{2} + k(t) \qquad \text{(II.B.38)}$$

where

$$\beta = [-3AF]^{1/3} \qquad \text{(II.B.39)}$$

and k(t) is a time integration function resulting from solution of the equation of motion. If we denote as P_c the value of the radial stress at the interface r = c, application of the stress boundary to eq. 38 gives

$$P_c = 2(S_0 - C)\ln(c/a) + 3C\ln(c/a)\ln\left(\frac{\beta^2}{ac}\right)$$

$$-P_m(\psi_c - \psi_a) \qquad \text{(II.B.40)}$$

where ψ_a and ψ_c denote the value of ψ at r = a and c, respectively. This must then be equated to the radial stress obtained from the solution of the elastic zone c-r-b.

In the elastic zone, a procedure identicial to that followed in the first phase of the deformation can be followed to arrive at the following solution:

$$P_c - P = \frac{4}{3}G(c^{-3} - b^{-3}) - P_m(P_c - P_a). \qquad \text{(II.B.41)}$$

P_c can be eliminated from eqs. 40 and 41 :

$$P(t) = \frac{4}{3}G(c^{-3} - b^{-3}) - \ln\left(\frac{c}{a}\right)[2S_0 - 3C\ln(\frac{c^3}{\alpha c^3 - 1})]$$

$$- P_m(P_a - P_a) \qquad \text{(II.B.42)}$$

a, b and c can subsequently be eliminated by means of eqs. 36, 37, 41 and 42, so that a relationship between t and P can be established. Since, as will be shown later, this intermediate phase is not of much interest, this final equation will not be developed here.

Fully Plastic Phase:

Once c reaches b, the sphere becomes fully viscous, and the full sphere can be considered with one constitutive equation. The equation of motion, once the appropriate substitutions are made, once again yields eq. 38, except that this time the boundary conditions given by eqs. 16 and 17 apply. Application of the boundary conditions results in:

$$P(t) = \ln\left[\left(\frac{\alpha}{\alpha-1}\right)^{1/3}\right]\left\{2(S_0 - C) + 3C\ln\right.$$

$$\left.\left[\frac{(-\dot{\epsilon}(A)^{2/3}}{(\alpha(\alpha-1))^{1/3}}\right]\right\} - P_m(P_b - P_a). \qquad \text{(II.B.43)}$$

As indicated by eq 43, the pressure response of the material consists of two parts: (a) a quasi-static part and (b) a dynamic part as represented by the acceleration potential term $\rho_m(\zeta_b - \zeta_a)/\gamma$.

The acceleration term can easily be shown to be

$$\rho_m(\zeta_b - \zeta_a) = \frac{-\rho_m a_0^3}{3(\alpha_0 - 1)}\left(\frac{1}{b} - \frac{1}{a}\right)\ddot{\gamma} + \frac{\rho_m a_0^6}{14(\alpha_0 - 1)^2}\left(b^{-4} - a^{-4}\right)\dot{\gamma}^2 \qquad \text{(II.E.46)}$$

where a and b are expressible in terms of γ by eqs 7a.

The acceleration term becomes significant only at very high load rates which involve significant inertial effects, including shock waves, impact, etc. Presently we are concerned with quasi-static load situations so that the acceleration terms may be neglected.

As indicated in section II.A, some modification of the constitutive law is needed to reflect work-hardening effects and to provide some correction for some of the simplifying assumptions used. By adding such a work-hardening term, $J\exp(-\phi\zeta/\zeta_0)$, and by making use of eq 24, eq 13 can be put in the following form:

$$p = -\frac{1}{3\zeta}\ln\left(\frac{\gamma}{\gamma - 1}\right)\left\{2(5_0 - 2)\zeta\ln\left[\frac{(\gamma - A)^2}{\zeta(\gamma - 1)}\right] + J\exp\left(-\phi\zeta/\zeta_0\right)\right\} \qquad \text{(II.E.47)}$$

where ϕ and J are material coefficients. This work-hardening term is of a nature consistent with the term used by St. Lawrence and Bradley (1974), who noted that Gilman (1969) used a similar term for lithium fluoride crystals to account for variations in the mobile dislocation velocity. In porous snow, work-hardening may be due to excessive amounts of intergranular motion that would not be present in solid polycrystalline ice. St. Lawrence and Bradley (1974) addressed this question in a more thorough manner. In

addition, the model used here is rather ideal in the sense that isolation of the pores is assumed, so that the effect of one pore on another was neglected.

Simplified Equation:

If Y is considerably smaller than σ, it can be shown that the strain incurred (and therefore $\epsilon - \epsilon_{ij}$) will be quite small during the first two phases of the deformation. If such is the case, these two first phases of deformation can be approximated by representing the material as a rigid-plastic material:

$$\sigma = \sigma_{ij} \text{ for } P_c$$

$$\dot{\epsilon} = 0 \text{ for } \sigma_{ij} \qquad \text{(II.B.46)}$$

$$\sigma_{ij} = \frac{1}{\epsilon_{ij}} \ln\left(\frac{\epsilon}{\epsilon_{ij}}\right) \left\{ \frac{2}{3}(S_{ij} - C) + \ln\left\{\frac{(\dot{\epsilon}/A)^2}{\epsilon(\epsilon-1)}\right\}\right\} J \exp(-\phi\frac{\epsilon}{\epsilon_0}) \quad \text{for } P_c \qquad \text{(II.B.47)}$$

where σ_{ij} is the critical stress at which the material first begins to yield. σ_{ij} is found by setting $\epsilon = 1$ in eq. 46 to yield

$$\sigma_{ij} = \frac{J}{\epsilon_{ij}} \ln\left(\frac{e}{\epsilon_{ij}-1}\right) \left\{\frac{2}{3}(S_{ij} - C)\right.$$

$$\left. + \ln\left(\frac{(\dot{\epsilon}/A)^2}{(\epsilon_{ij}-1)}\right)\right\} e^{-\phi} \qquad \text{(II.B.48)}$$

II.C COMPARISON WITH EXPERIMENTAL DATA FOR PORE COLLAPSE MODEL

ϵ_{ij}, C, and A are given in eq. II.A.12. The only other material constants that need to be evaluated are J and φ, the two-work-hardening coefficients. Based on data supplied by Abelo and Gow (1976), these two coefficients were found to be:

$$J = 3.07$$

$$\phi = 5.28. \qquad \text{(II.C.1)}$$

Eq II.E.48 was adjusted to data (Abele and Gow 1976) for snow of $\rho_0 = 1$ [illegible] and with an initial density of 400 kg m^{-3}.

The variation of the pressure with ϵ can then be calculated by means of eqs II.A.17, II.B.42, and compared with the data supplied by Abele and Gow (1975, 1976). The details of the experimental work are given in the reports of Abele and Gow, and the reader is referred to them for a well involved description of the experimental setup. Briefly, the tests consisted of high-rate axial compression tests in which the specimens were confined laterally in Teflon-lined aluminum cylinders. As a consequence, the deformation resulted in large, easily measured volumetric deformations.

Consider now the problem of the uniaxial compression of snow. If we take the x_1 direction as the axial direction and the x_2 and x_3 directions as the two lateral directions of a cylindrical specimen, the motion can be described by the equations (See Fig. 4):

$$x_1 = X_1 + \lambda t(1 - X_1/h_0)$$

$$x_2 = X_2$$

$$x_3 = X_3 \qquad \text{(II.C.2)}$$

where X_1, X_2, and X_3 are the undeformed coordinate positions, x_1, x_2 and x_3 are the deformed coordinate positions, t is time, λ is the crosshead velocity (constant in this case), and h_0 is the initial specimen height. The Jacobian of the deformation gives

$$J = \frac{\rho_0}{\rho} = 1 - (\lambda/h_0)t \qquad \text{(II.C.3)}$$

and therefore the density is

$$\rho = \rho_0[1 - (\lambda/h_0)t]^{-1}. \qquad \text{(II.C.4)}$$

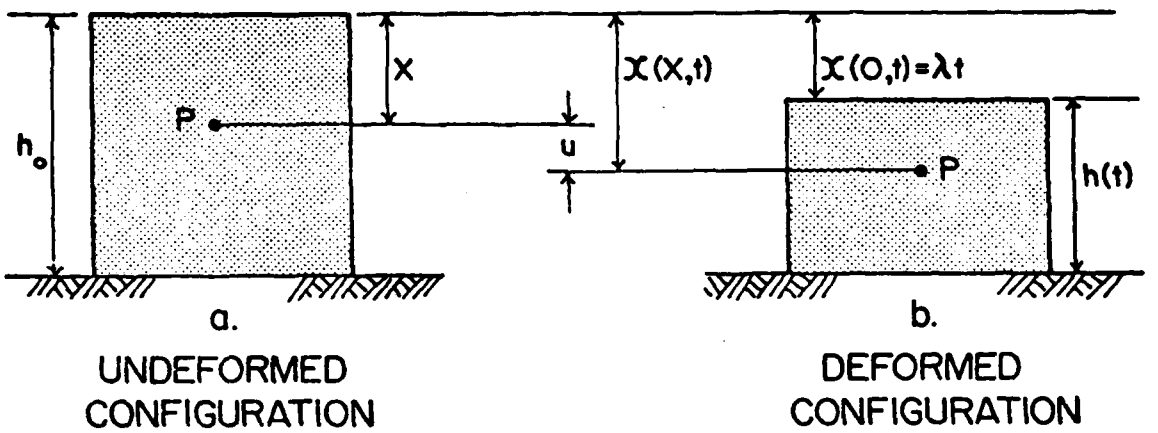

Figure 4. Kinematic representation of confined compression tests.

The density ratio, however, is

$$\alpha = \alpha_0[1-(\lambda/h_0)t] \qquad \text{(II.C.5)}$$

and its rate is

$$\dot{\alpha} = -\frac{\alpha_0\lambda}{h_0}. \qquad \text{(II.C.6)}$$

The constant rate tests do give a constant density ratio rate. Note, however, that the rate of change of density is not constant. For this set of experiments, $\dot{\alpha}$ was readily calcualted by eq 6 and eq II.B.47 was then utilized to find the variation of p and α for a given rate. Figure 5 shows the comparison of theory with experiment for snow at -10°C and for three initial densities. The data acquired by Abele and Gow (1975, 1976) included a variety of strain rates, since different specimen sizes and crosshead speeds were utilized. The data shown here reflect rates in the neighborhood of $\dot{\alpha} \tilde{\sim} 10s^{-1}$.

The data available from Abele and Gow (1975, 1976) measured only σ_1, the major principal stress, whereas the hydrostatic pressure $p = -1/3(\sigma_1+\sigma_2+\sigma_3)$ was needed. Therefore, a series of experiments was run to measure lateral stress as well as axial stress so that Abele's and Gow's data could be adjusted to reflect p rather than σ_1. It was found that

$$0.6\,\sigma_1 < p < 0.98\sigma_1 \qquad \text{(II.C.7)}$$

for all the experiments run, thereby fairly well bracketing the data report by Abele and Gow (1975, 1976).

One interesting result was observed in the testing program. In tests involving "old" snow, the lateral stress was found to be about 90% of the axial stress, but for tests of "new" snow, the lateral stress was only 30-40% of the axial stress. In each case, unbonded snow (sifted within two hours of the time of testing) was used, so that the difference between the

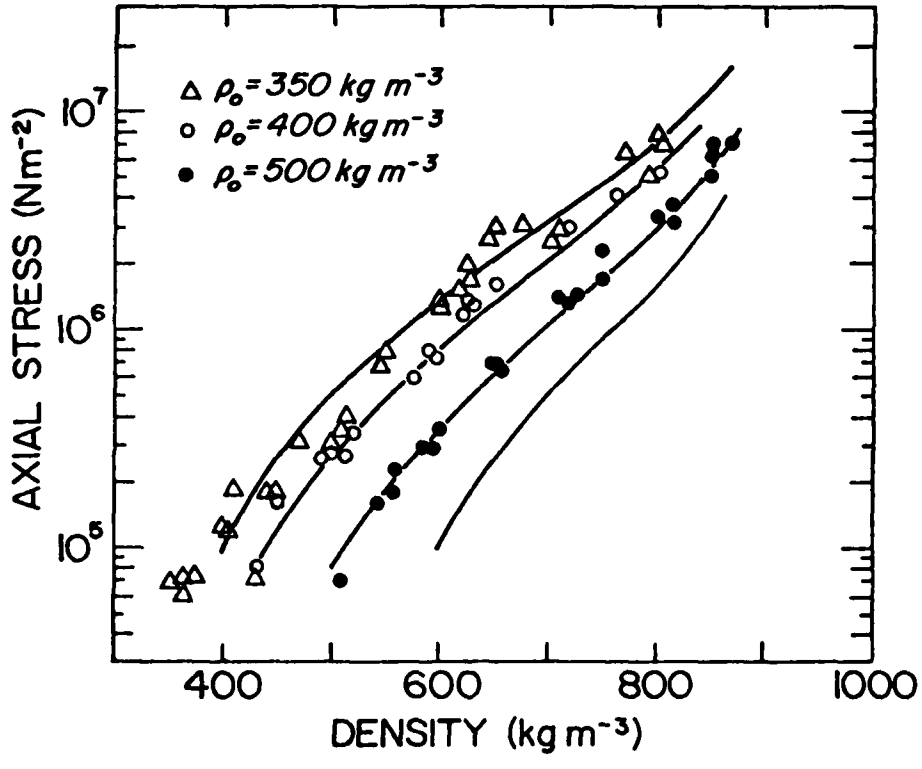

Figure 5. Comparison of pore collapse theory with experimental data.

lateral stress in the old snow and that in the new snow must have been due to differences in crystal structure, primarily crystal shape. The old snow had undergone equitemperature metamorphism, and the crystals had a spherical shape. The grains, therefore, were capable of rolling and sliding relative to each other, thereby accommodating a lateral motion to produce a large lateral stress. New snow, with its complicated grain structure, would not allow this, thereby producing a smaller lateral stress.

As can be observed from Figure 5, the comparison between theory and experiment is quite good, with the essential characteristics of the deformation being represented by the theory.

Figure 6 compares theoretical pressure curves with data collected and summarized by Mellor (1974). This figure contains results of laboratory studies as well as field data relating density to gravity reasonable compared with the data. It should be remembered that some of the data shown in this figure represent uniaxial stress conditions, and that the actual hydrostatic pressures are only one-third the values shown for these data. Therefore, some of the experimental curves would move down vertically relative to the theoretical curves. However, since there is such a diverse range of load histories, temperatures, and time ranges contained in Figure 6, any meticulous adjustments would not necessarily change things that much. What can be said, though, is that eq II.B.48 appears to be functionally correct for snow with initial densities exceeding 300 kg m^{-3}.

Figures 7 and 8 further describe some important properties. The deformation rate dependency is illustrated in Figure 7. For snow with an initial density of 350 kg m^{-3}, the stress response is shown as a function of density-ratio rate at three different instantaneous densities. As can be seen, a rate dependency does exist, but the importance of rate decreases as rate increases. At rates characteristic of stress waves, therefore, one

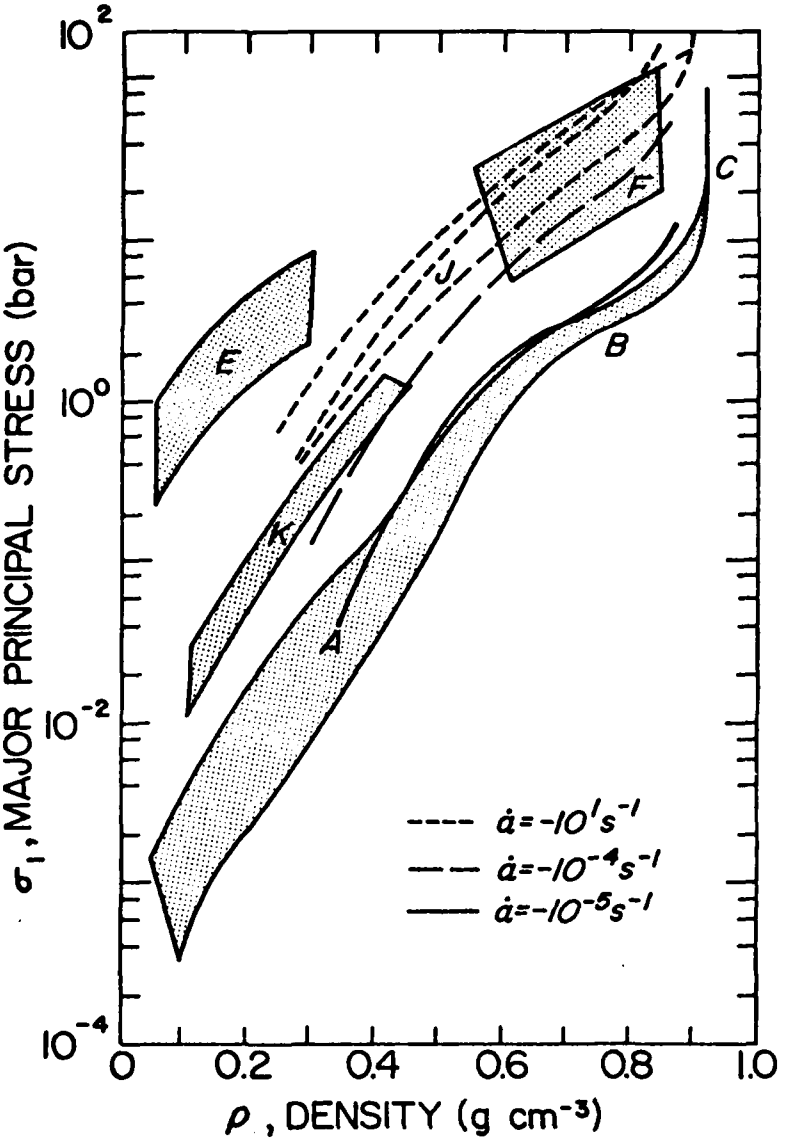

Figure 6. Comparison of pore collapse model with data supplied by Mellor (1974).

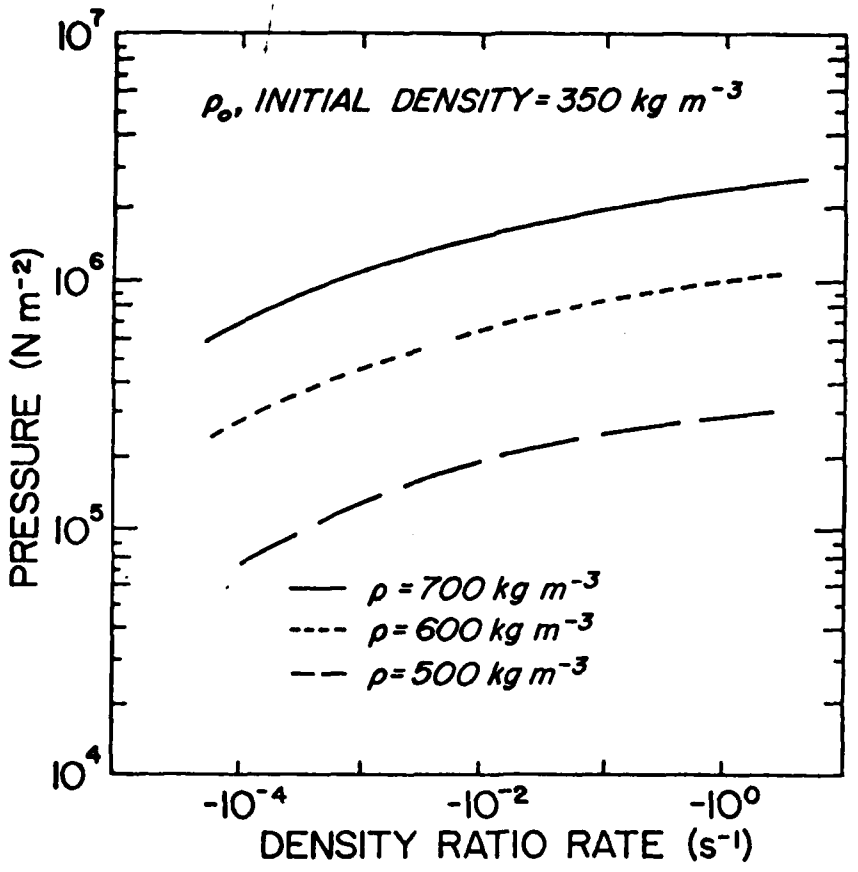

Figure 7. Variation of pressure response with rate of change of density ratio, $\dot{\alpha}$.

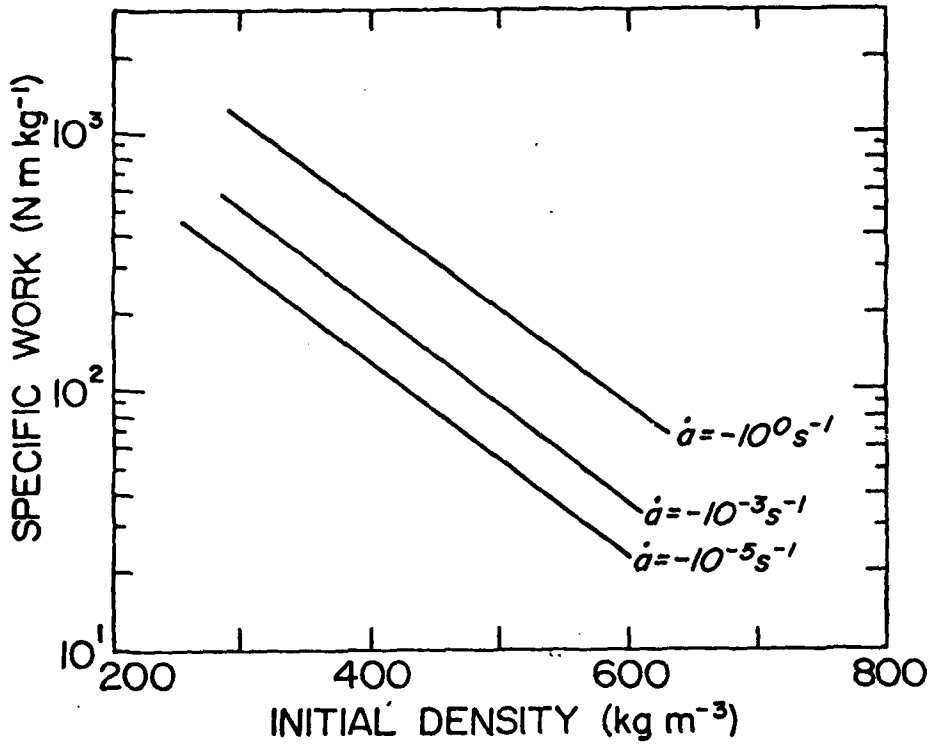

Figure 8. Variation of compaction energy with deformation rate.

might be able to assume a constant yield stress and achieve a simplified version of the constitutive law given in eq. II.B.48. However, for lower rates, say in the range $10^{-5}<|\dot{\alpha}|<10$, the rate dependency is significant enough that such a simplifying procedure would not be recommended.

Figure 8 gives an indication of just how effectively snow can absorb energy during compaction. In particular, this figure shows the work required to compact snow to a terminal density of 700 kg m^{-3} for a range of initial densities and density-ratio rates. One can see immediately that initial density has a dramatic effect on work required to compress snow. Density-ratio rate is also significant but certainly much less so than initial density.

II.D. DEVELOPMENT OF CONSTITUTIVE LAW FOR NECK GROWTH MODEL

The deformation of porous material such as snow involves several different mechanisms which act simultaneously to varying extents. Three such mechanisms are: (a) pore collapse, (b) intergranular glide, and (c) inelastic deformation of intergranular necks. Pore collapse and neck deformation both involve deformation of the matrix material, whereas intergranular glide is a function of bond strength and surface frictional properties. Pore collapse is a predominant mechanism at higher densities, and was shown to accurately define mechanical behavior in the previous section.

For low density snow, the volumetric deformation is determiend largely by the intergranular glide and inelastic deformation of the grains and necks. Under a state of hydrostatic pressure, one may expect effects due to intergranular glide to be reduced to a minimum relative to inelastic deformation. Due to the random nature of both grain geometry and grain-to-grain bonding, glide effects certainly cannot be eliminated, but it may be reasonable to ignore them in comparison to the volumetric strains due to plastic deformation and flow of the matrix material.

In this section, a constitutive law for volumetric deformation of low density snow is formulated by using a neck-growth model. In order to account for intergranular slip effects, an empirical adjustment of the equation is then made, and the results are then compared to existing experimental data.

From Figure 9(a), a good idea of the grain and neck geometry can be obtained. The grains are those structural elements which have free surfaces which are predominantly concave inward, toward the center of the grain, where this radius of curvature is denoted by R. Individual grains are connected by necked-down regions whose surface are concave outward toward the air phase in the section view shown in Figure 9(a).. This radius is denoted by R'. The bond is the plane containing the minimum cross sectional area of the neck. When two ice grains are brought into contact, the length L of the neck begins to increase from its initial value of zero, since sintering effects begin to produce the concave outward geometry of the neck. This is illustrated in Figure 9. In many cases the length of the neck can be quite large, particularly for low density snow in which some of the necks have developed from the fragile needle structure of fresh snow.

If one is considering fracture strength of snow, the bonds are of primary importance, since these are the regions of low cross sectional area in the material. However, characterization of the deformation properties of snow must consider the entire neck and the ice grains, since they contribute to the total deformation process.

In developing the constitutive relation, inertial effects are assumed to be negligible. The major portion of the deformation procss is assumed to take place in the necked regions of the granular structure. The grain bodies them selves eventually begin yielding as the pressure increases

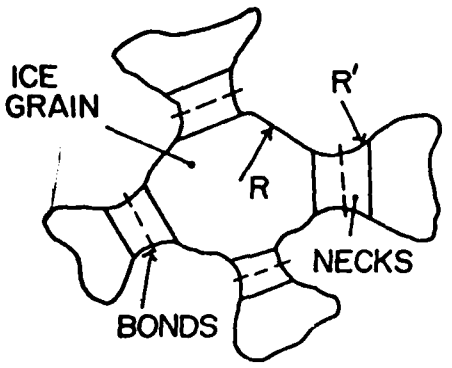

a. TYPICAL GRAIN and NECK GEOMETRY

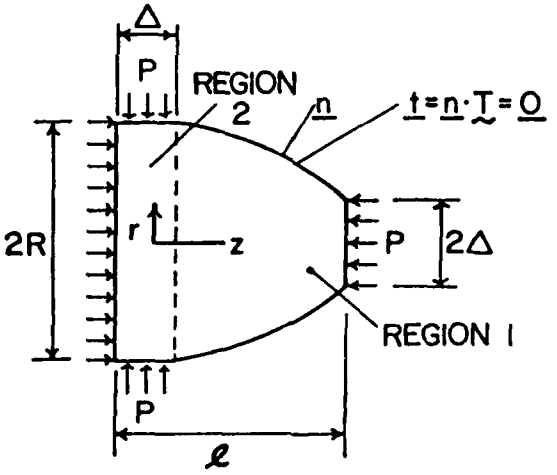

b. IDEALIZED GRAIN GEOMETRY

Figure 9. Representation of grain and bond geometry for neck-growth model of snow deformation.

during the deformation process. In undistrubed snow that has had several days to sinter at temperatures of about -5°C, the grain bonds will usually have cross sectional radii at least 25% as large as the grain bodies themselves. This rate of bonding depends to a large extent on the temperature and imposed pressure. At temperatures below - 30°C, snow sinters very slowly. In the absence of a temperature gradient, snow at -5°C can be fully bonded within one day with grain bond radii on the order of 10% of the grain body if moderate pressures are imposed on the material.

With reference to Fig. 9, the ice grain can be divided into two regions. Region 1 is that portion of the grain body upon which lateral surface loading is imposed, whereas Region 2 has a load-free lateral boundary. Region 1 does have some stress free surface since the grain bonds do not completely envelop the surface. The material is assumed to be completely yielded, since primary interest is in snow under large volumetric deformations.

The grain radius is R, and Δ is the neck radius. the bearing stress P (Fig. 9(b)) on the grain bond is assume to be related to the macroscopically measured pressure, p, by

$$P \sim p\alpha(R/\Delta)^2 \qquad \text{(II.D.1)}$$

Here α is taken to be the density ratio,

$$\alpha = \rho_m/\rho \qquad \text{(II.D.2)}$$

where ρ_m and ρ are, respectively, the densities of the matrix material (ice) and the porous material (snow).

Consider first Region 2 of the ice grain. Assuming surface tension effects are negligible, its lateral surface is completely stress free. The stress tensor, using a cylindrical coordinate system, has the nonzero stress components σ_{zz}, σ_{rr}, $\sigma_{\theta\theta}$, and σ_{zr}. The stress-free boundary condition on the lateral surface can be used to obtain:

$$\sigma_{rz} = \sigma_{zz}\, \partial R/\partial z \qquad \text{(II.D.3)}$$

The z and r components of the equation of equilibrium are

$$\partial\sigma_{zz}/\partial z + (1/r)\partial(r\,\sigma_{rz})/\partial r = 0 \qquad \text{(II.D.4)}$$

$$\partial\sigma_{rr}/\partial r + \partial\sigma_{rz}/\partial z + (\sigma_{rr} - \sigma_{\theta\theta})/r = 0 \qquad \text{(II.D.5)}$$

The condition of incompressibility requires that

$$\partial v_z/\partial z + (1/r)\partial(rv_r)/\partial r = 0 \qquad \text{II.D.6)}$$

where v_r, v_z and v_θ are the velocity components in the r, z and θ directions. Integration of eq 4 and use of Leibnitz's rule and the mean value theorem results in

$$\int_o^R 2\pi r(\partial\sigma_{zz}/\partial z)dr = A_z\partial\bar{\sigma}_{zz}/\partial z + (\bar{\sigma}_{zz}(z,t) - \sigma_{zz}(R,z,t))\, \partial A_z/\partial z \qquad \text{(II.D.7)}$$

where $\bar{\sigma}_{zz}$ is the average axial stress on the cross sectional area A_z at the location z in Region 2. The following relation,

$$\int_o^R 2\pi r(\partial\sigma_{zz}/\partial z)dr = A_z\partial\bar{\sigma}_{zz}/\partial z, \qquad \text{(II.D.8)}$$

is approximately correct if either $(\bar{\sigma}_{zz}(z,t) - \sigma_{zz}(R,z))$ or $\partial A_z/\partial z$ is sufficiently small to make their product small in comparison with the other terms in eq. 7. Assuming this approximation, the z-component of the equation of equilibrium becomes, after application of the boundary condition,

$$\partial\sigma_{zz}/\partial z + (2\sigma_{zz}/R)\, \partial R/\partial z = 0 \qquad \text{(II.D.9)}$$

Utilizing material incompressibility and the predominantly axial state of stress, the flow law given in eq. II.A.1 acquires, after some algebra, the form

$$\sigma_{zz} = 2S_o + 2C \ln((3A/4)\, \partial v_z/\partial z) \qquad \text{(II.D.10)}$$

Solving for $\partial v_z/\partial z$ gives

$$\partial v_z(z,t)/\partial z = (4/3A) \exp (\sigma_{zz}/2C - S_o/C) \qquad \text{(II.D.11)}$$

which can be shown to satisfy the equilibrium equation, eq. 9. The incompressibility condition can be used to show that the rate of change of the radial velocity v_r is

$$v_r = - (r/2) \partial v_z/\partial z \qquad \text{(II.D.12)}$$

Setting r and v_r equal, respectively, to Δ and $\dot{\Delta}$ in eq 12 and substituting into eq. 11 yield

$$\dot{\Delta} = -(2\Delta/3A) \exp (\sigma_{zz}/2C - S_o/C) \qquad \text{(II.D.13)}$$

Now consider the deformation in Region 1 of the ice grain. In this region, part of the lateral surface is constrained by the bearing pressure of adjacent grain bonds. In this case, at a neck

$$\sigma_{rr} = - p \alpha(R/\Delta)^2 \qquad \text{(II.D.14)}$$

whereas σ_{rr} is zero on other parts of the lateral surface not in direct contact with a neck. The average stress on the lateral surface must be reduced by a factor f, $0 \leq f \leq 1$, which gives the fraction of lateral surface in contact with a neck. Therefore the average value of σ_{rr} at r = R is

$$\sigma_{rr} = - f p \alpha (R/\Delta)^2 \qquad \text{(II.D.15)}$$

which gives the mean radial component of stress acting on the radial surface of the grain in Region 1. The radius R is relatively constant with respect to z in this region.

In what follows, the superscripts I and II are used to refer to regions 1 and 2, respectively. From eq. 1 the axial component of stress, σ_{zz}, in Region 1 is approximately

$$\sigma_{zz}{}^{I} = -p\alpha \qquad \text{(II.D.16)}$$

These last two equations define an average stress state in Region 1. The maximum difference value S in Region 1 is then

$$S = \sigma_{zz}{}^{I} \left[(R/\Delta)^2 f-1\right] \qquad \text{(II.D.17)}$$

$$= \sigma_{zz}{}^{II} \left[f - (\Delta/R)^2\right]$$

Making use of incompressibility, the maximum difference value for the rate of deformation tensor can be found to be

$$D = (1/r^2) \frac{\partial}{\partial r} (r^2 v_r) \qquad \text{(II.D.18)}$$

Returning to the constitutive law, and then integrating this after first substituting eqs 17,18 yield

$$\dot{R} = -\frac{R}{A} \exp \left\{\left[\left(\frac{R}{A}\right)^2 f-1\right] \frac{p\alpha}{C} - S_o/C\right\} \qquad \text{(II.D.19)}$$

Equations 13 and 19 define the rate of change of the neck radius and grain radius respectively. These must now be related to the rate of change of the density ratio. If V_m is the volume of the solid ice phase in a cubical region containing the grain of radius R and N necks of length L, one can show that V_m and the volume V of the cubical region are

$$V = (2\sqrt{R^2 - \Delta^2} + L)^3 \qquad \text{(II.D.20)}$$

$$V_m = (4-2N)\pi R^2/3 + N\pi\Delta^2 L/2$$

$$+ (N\pi/3)\ (2R^2 + \Delta^2)\ \sqrt{R^2-\Delta^2} \qquad \text{(II.D.21)}$$

V_m must be constant if the matrix material is incompressible. Utilizing this constraint gives the following approximate relationship for the rate of change of the bond length L,

$$\dot{L} = B_1\dot{\Delta} + B_2\dot{R} \qquad \text{(II.D.22)}$$

where

$$B_2 = -\frac{2}{N\Delta^2}\left\{\left(4 - \frac{2}{3}N\right)R^2 + N(2R^2 + \Delta^2)/3\right\} \qquad \text{(II.D.23)}$$

$$B_1 = -(2/N\Delta^2)\left\{N\Delta L + 2NR\Delta/3 - (2R^2 + \Delta^2)\Delta N/(3R)\right\} \qquad \text{(II.D.24)}$$

The average number of bonds N attached to a grain varies with density and snow type. In the absence of any substantial data on the variation of N with density, the following approximate relation is assumed.

$$N = 4\ (1 + (\rho - 0.30)/0.50) \qquad \text{(II.D.25)}$$

where ρ is given in Mg m^{-3}. Very little data are available to verify the accuracy of this equation. Kry and Gubler made studies of snow structure, but their results considered a relatively narrow density range. The density ratio can also be expressed as the ratio V/V_m. Then, the rate of change of α can be calculated with the use of eqs 13, 14, 20, 21, and 22. The result of this is

$$\dot{\alpha} = A_1 \exp(\beta_1 p) + A_2 \exp(\beta_2 p) \qquad \text{(II.D.26)}$$

where

$$\beta_1 = \frac{3\alpha}{2C}\ (R/\Delta)^2$$

$$\beta_2 = \frac{\alpha}{C}\left[(R/\Delta)^2 f - 1\right] \qquad \text{(II.D.27)}$$

$$A_1 = (2K\Delta/3A)\ (-2\Delta/\sqrt{R^2 - \Delta^2} + B_1)\ \exp(-S_o/C)$$

$$A_2 = (KR/3A)\ (2R/\sqrt{R^2 - \Delta^2} + B_2)\ \exp(-S_o/C)$$

$$K = 3(2\sqrt{R^2 - \Delta^2} + L)^2/V_m$$

Eq 26 describes a volumetric behavior for snow which functionally has the correct form. However, acceptable accuracy cannot be expected since factors such as work hardening of the matrix material, effects of random grain and neck geometry, and intergranular glide have not been accounted for. In order to adjust this equation to better fit experimental data, the following emperical

term is used

$$F = C_1 \rho_o \, (\alpha/\alpha_o)^{C_2 + C_3 \rho_o} \qquad \text{(II.D.28)}$$

to divide the pressure p in eq 26.

The constitutive equation then becomes

$$\dot{\alpha} = A_1 \exp(\beta_1 p/F) + A_2 \exp(\beta_2 p/F) \qquad \text{(II.D.29)}$$

with A_1, A_2, β_1 and β_2 remaining unchanged from the values given in eqs. 23, 24 and 27. In these results, all coefficients are determined by the properties of ice and the structure of snow, except for the three constants C_1, C_2 and C_3 contained in eq. 28.

II. E COMPARISON WITH EXPERIMENTAL DATA FOR NECK GROWTH MODEL

Abele and Gow (1975,1976) have reported results of their studies on the high rate volumetric properties of snow. Their 1976 study involved the deformation of sifted and compacted snow, a process which resulted in initial densities higher than 0.30 Mg m^{-3}. Their 1975 work was concerned with natural undisturbed snow with densities ranging from 0.1 Mg m^{-3} to 0.30 Mg m^{-3} and a temperature range of $-30°C \leq \theta \leq -2°C$. Their experiments consisted of confined compression tests and have already been described in Section II.C. The reader is referred to that section in order to familiarize himself with the test procedures.

Several densities were considered here to demonstrate the effect of initial density on the stress response of the snow. Generally, the average crystal diameter was about 0.2 to 0.3 mm, although this was at best an estimate obtained from the thin sections illustrated in reports by Abele and Gow. This snow is similar to fine grained seasonal snow. The bond radius was taken to be 0.08 - 0.12 mm, based on thin sections illustrated in Abele's paper.

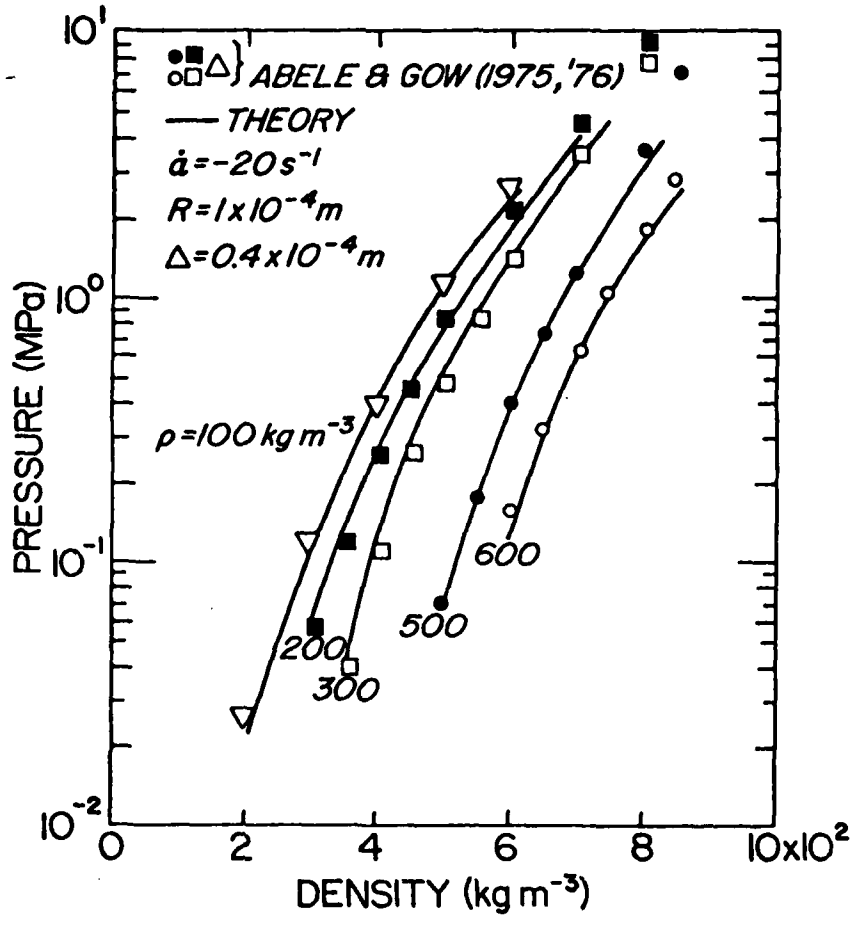

Figure 10. Comparison of neck-growth theory with experimental data.

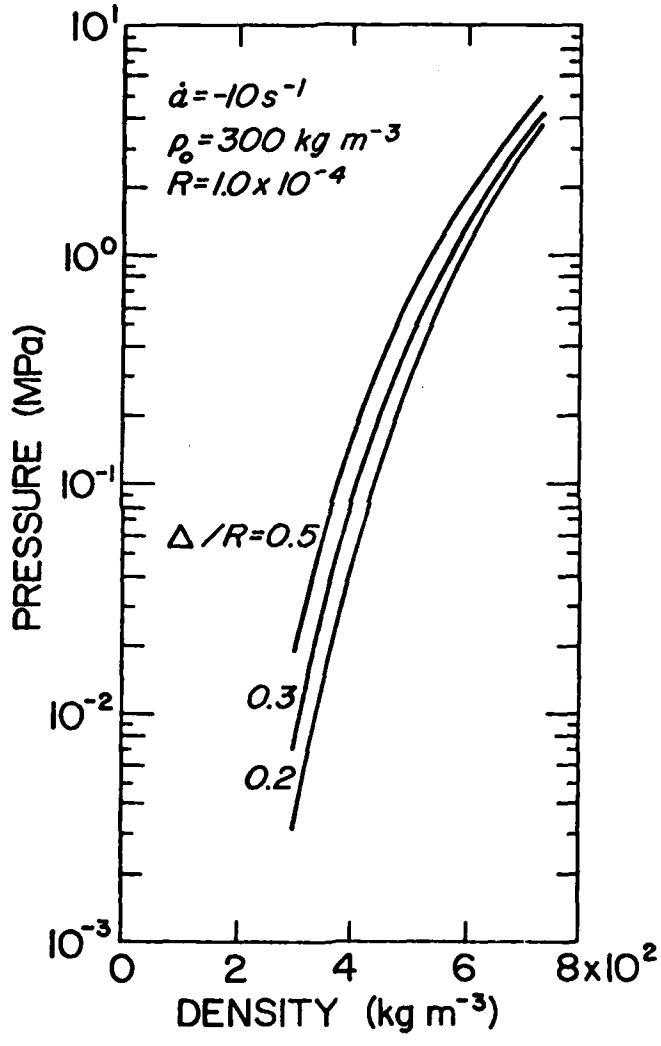

Figure 11. Effect of initial bond radius - grain radius ratio on material properties.

Figure 10 illustrates a comparison of theory with the experimental data. The term F in eqs 28 and 29 was evaluated by determining the coefficients to fit eq 29 to the experimental data for an initial density of 0.30 Mg m^{-3}. C_1, C_2 and C_3 were found to be 0.112, 1.67, and 6.40, respectively. As can be readily seen, for all densities from 0.10 Mg m^{-3} to 0.60 Mg m^{-3} the agreement between theory and experiment is excellent.

Figure 11 illustrates the effect of bond size on the volumetric properties of snow. In Figure 11, grain size is held constant while bond size is varied over a range characteristic of alpine snow. Figure 12 illustrates the effect of deformation rate on the response of snow. The importance of grain size on pressure response was checked. R was varied over an order of magnitude while the ratio Δ/R was kept constant, and the pressure response was found to vary by less than a percentage point, so that one may conclude that grain size is a second order effect.

II.F SIMPLIFIED EQUATION FOR NECK GROWTH MODEL

Equations 13 and 19 can be used to calculate $\dot{\Delta}$ and $\dot{R}$ during volumetric compaction. This was done for the range of initial densities and deformation rates illustrated in Figures 10, 11 and 12, and $\dot{R}$ was found to be at least two orders of magnitude less than $\dot{\Delta}$. This is due to the fact that the grains have a high degree of lateral constraint, whereas the grain bonds are essentially unrestrained. This result allows the constitutive equation to be simplified by neglecting the term $B_2 \exp(\beta_2 Fp)$. The resulting simplified constitutive law becomes

$$\dot{\alpha} = A_1 e^{\beta_1 p/F} \qquad \text{(II.F.1)}$$

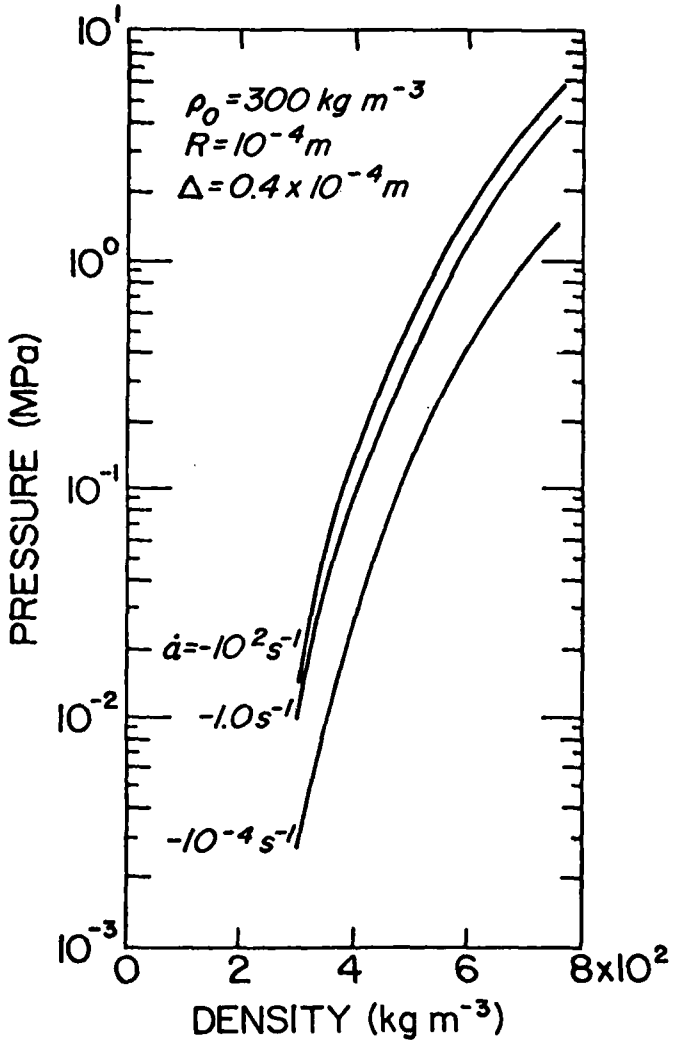

Figure 12. Effect of deformation rate on pressure as predicted by neck-growth model.

and this equation is more readily inverted to obtain p as a function of α and $\dot{\alpha}$. This equation gives results virtually identical to the results illustrated in Figures 10 - 12.

The above constitutive equation is considered to be valid for quazi-static rates of loading. When very large rates, such as those associated with stress waves are incurred, intergranular dynamical effects such as those derived in the pore collapse model should be included. This results with the following constitutive law.

$$p = \frac{F}{\beta_1} \ln (\dot{\alpha}/A_1) + \frac{\tau^2}{\alpha} \frac{dQ}{d\alpha} (\alpha,\dot{\alpha},\ddot{\alpha}) \qquad \text{(II.F.2)}$$

In summary, a rate sensitive volumetric constitutive law based on grain and grain bond deformation has been developed and compared with experimental data. As can be seen in the above, the developed law does accurately describe the behavior of snow for a given deformation rate and for a range of initial densities. Aside from the rheological properties of the matrix material, one of the most important parameters is the ratio Δ/R of the bond and grain radii in the undeformed snow. However, the importance of this parameter becomes less significant as volumetric strains become large. This can be better understood by first considering Figure 13, which shows the variation of the neck radius as a function of density for two different intial neck radii. It can be seen that the relative differences in bond radii decrease during the compaction process. The smaller bonds experience a larger stress and hence flow more readily than the large bonds, thereby growing at a faster rate.

The constitutive law was found to lose accuracy at the higher pressures where the theoretical curves are terminated in Figure 10. For all four cases shown in Figure 10, this occurred when the bond radius was about three fourths the value of the grain radius. At this point, the adjacent bonds

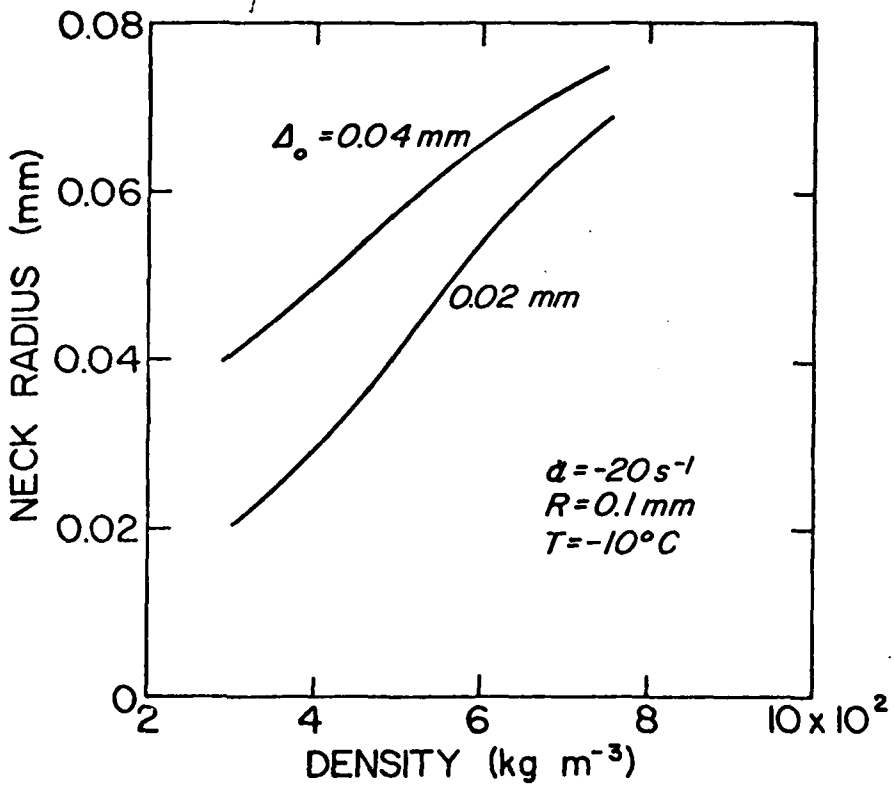

Figure 13. Variation of neck radius with density during high rate compaction of snow.

on an ice grain begin to interact in a significant degree as they grow into each other. The kinematic equations, eq 22 - 27, do not account for this, and this may be part of the reason for the loss of accuracy at the higher densities.

The neck growth model used in this study could be applied to other materials such as porous metals, although the constitutive law for the matrix material would be different than the one used here. However, the kinematical description used here should be readily adaptable to other porous materials.

III APPLICATION TO THE PROBLEM OF VEHICLE MOBILITY

III.A INTRODUCTORY REMARKS

The problem of oversnow mobility can generally be divided into two different but related topics: (1) power requirements for motion in snow and (2) traction requirements. The latter problem has probably received more attention, since sufficient traction and drawbar pull capability must be developed before any forward motion is possible. In addition the problem of traction capability is somewhat simpler to define mathematically, at least in the manner that this problem has been previously treated (Mellor 1963). This is not meant to imply that the problem of traction capability is a simple problem, since the stress state in the immediate vicinity of the track grousers is quite complex. Previous studies have avoided a detailed stress analysis by calculating averaged shear stress capability of the snow at the track-snow interface. A relation similar to the Coulomb-Mohr criterion is used to find the shear stress in terms of the track pressure, and by application of equilibrium, the tractive capability of the vehicle can be found. This approach has met with some success as indicated by Mellor (1963). In addition, Harrison (1956, 1975) has utilized a method used for soils to predict drawbar pull capability, but he has pointed out some shortcomings of this method.

The problem of calculation of vehicle power requirements has however not been studied as extensively as the second problem. A very relevant reason for this is that there has not existed a theory for accurately defining the volumetric properties of snow under finite, high rate compaction processes. This difficulty has in part been relieved by the development of volumetric constitutive laws such as presented in Section II, where it was shown to accurately predict the response of medium-to-high density snow

to large amplitude high rate volumetric deformations.

In the case of a shallow snowpack, the pressure bulb, which is the region of compacted snow directly beneath the vehicle track, extends to the ground. This enables the relatively rigid ground to lend a significant amount of support to the vehicle. If the snowpack is quite shallow, the effects of the shear stress on the sides of the pressure bulb may be neglected. The pressure inside the bulb does not consequently vary signficantly in the vertical direction, thereby allowing the rather easy calculation of power requirements for tracked vehicles in snow.

In the case of deep snowpack, the pressure bulb receives no support from the ground, and the bulb must be supported primarily by the shear stresses existing on the bulb wall. As a consequence the pressure bulb can extend a significant distance into the snowpack before an equilibrated state is reached. Due to the effects of the shear on the bulb walls, the pressure and the density distribution in the wall is no longer uniform.

The constitutive law in eq II.B.47 is used to estimate energy and power requirements for over-snow tracked vehicles. Since high rates and large amounts of compaction are involved, constitutive equations developed by other researchers are generally not valid for this case. Mellor (1974, 1977) gives a thorough review of previous constitutive formulations for snow, and one can readily see that most previous work is valid for either small strains or rates well below those that can be generated by tracked vehicles in motion. The following analysis, therefore, represents one of the first attempts to analytically calcualte power requirements for tracked vehicles which generate large amounts of compaction of snow. The comparatively simple problem of shallow snowpack is first studied, and then deep snowpack mobility is considered in the following section.

III.B TRACKED VEHICLE MOBILITY IN SHALLOW SNOWPACK OF MEDIUM DENSITY

Harrison* (private communication) has indicated that the cross section of the failure zone below a vehicle track takes on a somewhat rectangular shape. Figure 14 gives a schematic of the failure region, often referred to as the pressure bulb. It is assumed that shear failure occurs along the sides of the failure region, and that the material directly below the vehicle track undergoes unidirectional compaction. Outside the pressure bulb, the snow undergoes very little compaction so that the energy dissipated would be negligible when compared to the dissipation occurring within the pressure bulb. The depth of the failure region depends on the shear strength of the snow, and some of the energy dissipation is invariably due to deviatoric deformations. However, when one considers the massive amount of compaction occurring within the pressure bulb, neglecting deviatoric energy dissipation becomes a valid simplifying approximation. There are conditions under which such an assumption may not be reasonable. This would include situations of slippage or vehicle turning. But if a vehicle is moving along a straight path and is not experiencing much slipping, the above approximation should be valid. At any rate, the results should give a reasonable lower bound on vehicle power requirements and allow for a good parametric study of the problem. The following analysis would be particularly valid in the case of shallow snow in which the pressure bulb extends to the ground.

The constitutive equation as given by eq II.B.47 can be used to calculate directly the energy a vehicle expends in compacting snow during its passage. Stress power is given by

$$\dot{W} = \frac{1}{\rho} \operatorname{tr}(\underset{\sim}{T} \cdot \underset{\sim}{D}) \qquad \text{(III.B.1)}$$

*Research Engineer, U.S. Army Cold Regions Research and Engineering Laboratory, Hanover, New Hampshire 03755.

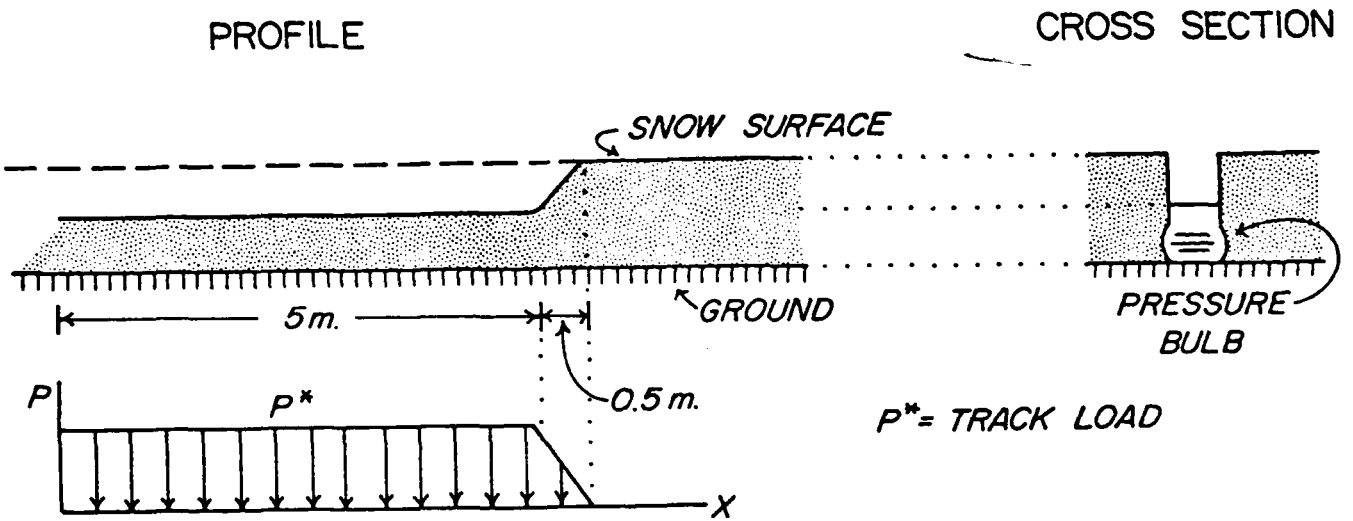

Figure 14. Representation of track loading and pressure bulb geometry for shallow snowpack.

where $\underset{\sim}{T}$ and $\underset{\sim}{D}$ are, respectively, the Cauchy stress tensor and the rate of deformation tensor. tr(·) is the trace of the tensor quantity inside the parenthesis. The stress power, $\dot{W}$, is simply the rate, per unit mass, at which work is being done internally by the stresses. $\hat{W}$ is a central part of the first and second laws of thermodynamics. For a purely viscous material under isothermal conditions, $\dot{W}$ would reduce to the rate of energy disspiation. For a viscoelastic material, the stress power would contribute to both the rate of change of strain energy and to the rate of energy dissipation.

In case of a undirectional deformation, the stress power associated with compaction is:

$$\hat{W} = -\frac{p}{\rho}\frac{\partial v}{\partial x} \qquad \text{(III.B.2)}$$

where p is the hydrostatic pressure, v is vertical particle velocity, and x is the vertical coordinate position of the particle during deformation. The continuity equation for unidirectional motion is

$$\frac{d\rho}{dt} + \rho\frac{\partial v}{\partial x} = 0 \qquad \text{(III.B.3)}$$

Eqs. II.B.47, 2 and 3 can then be used to obtain

$$\hat{W} = -\frac{1}{\rho_m} p\,\dot{\alpha} \qquad \text{(III.B.4)}$$

Integration of eq 4 results with

$$W = -\int_{t_o}^{t} \frac{p}{\rho_m}\dot{\alpha}\,dt \qquad \text{(III.B.5)}$$

In the above the pressure p is a function of time. Eq II.B.47 may be inverted to yield

$$\dot{\alpha} = -e^{Q(t,\alpha)} \qquad \text{(III.B.6)}$$

where

$$Q(t,\alpha) = \frac{1}{2}\,[F(t,\alpha) + \ln[\alpha(\alpha-1)]] - \ln A \qquad \text{(III.B.7)}$$

$$F(t,\alpha) = \frac{1}{C}\,[3\alpha p(t) e^{(\phi\alpha/\alpha_o)}/(J\ln(\frac{\alpha}{\alpha-1})) - 2(S_0-C)] \qquad \text{(III.B.8)}$$

The pressure loading in the material below the track is assumed to have the form

$$p(t) = p^* \frac{t}{t_o}\,[1 - H(t-t_o)] + P^*H(t-t_o) \qquad \text{(III.B.9)}$$

where H(t) is the Heavyside step function. Figure 14 shows the nature of the pressure distribution under the track. The total work done by the track to a unit mass of snow is then

$$W = \int_o^{t^*} \frac{1}{\rho_m}\, p(t)\; e^{Q(t,\alpha)}\, dt \qquad \text{(III.B.10)}$$

where t* is the duration of time that the snow is under the track. Eqs. 7 to 10 can then be used to study the energetics of oversnow vehicle travel.

The above results have been used to make such a study. By substituting the assumed pressure function given by eq 9 into eq 10 and integrating eq 10 over the time t* corresponding to the interval that an element of snow is under the vehicle track, the actual work in compressing a unit volume of undeformed snow is found. This gives a direct measure of track efficiency for a given set of parameters such as vehicle speed, track pressure, track geometry, and snow properties.

Eq 2 gives the instantaneous power/unit mass of snow while the material is under the track, and this expression can vary considerably during the interval, t*, of track loading. For the purpose of this study, the average power is more meaningful, and this is calculated by simply dividing the total work per unit mass, W, by the time period, t*, required to produce this work.

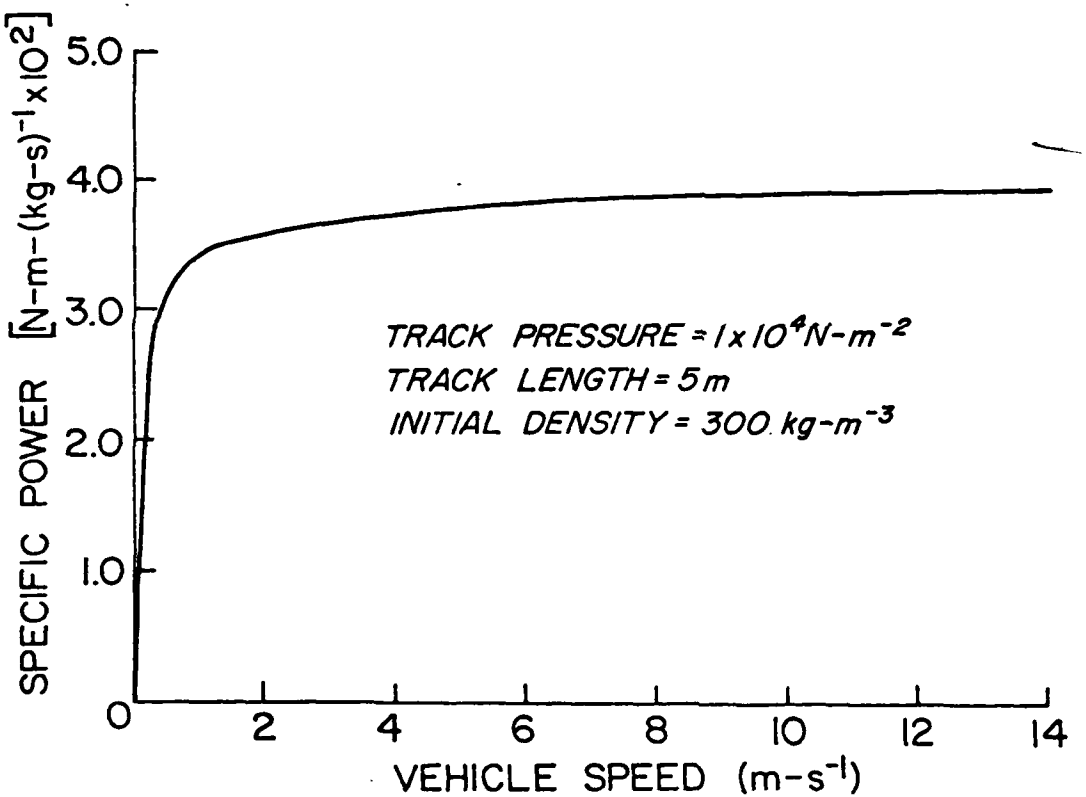

Figure 15. Variation of power consumption with vehicle speed.

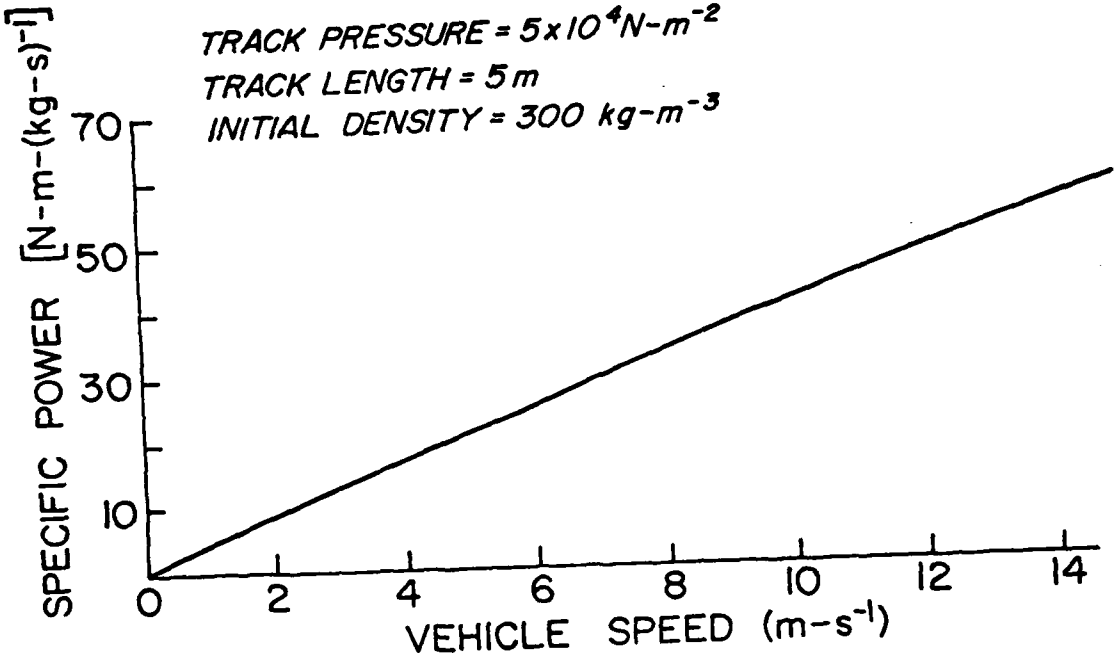

Figure 16. Variation of power consumption in shallow snowpack with vehicle speed.

Therefore,

$$P = \frac{1}{t^*}\int_0^{t^*} p(t)\ \frac{e^{\phi(t,\alpha)}}{\alpha}\ dt \qquad \text{(III.B.11)}$$

gives the power per unit mass is subsequently refrred to as "specific power". The specific power, P, would have to be augmented by a factor equal to the total mass of snow under the tracks, if one wanted to find the total power requirements.

- Nominally, a track length of 5 meters was chosen. Track pressure was limited to $5x10^4 N\text{-}m^{-2}$, which admittedly is uncharacteristically low when considering military vehicles. However, such pressures are more realistic for vehicles such as snowmobiles. Initial snow densities studied range from 300 $Kg\text{-}m^{-3}$ to 700 $Kg\text{-}m^{-3}$, and vehicle speeds are restricted to about 15 $m\text{-}sec^{-1}$.

Figures 15 and 16 compare specific power requirements for two track loadings, and a significant difference is generated when one increases the track loading from $1x10^4$ $N\text{-}m^{-2}$ to $5x10^4$ $N\text{-}m^{-2}$. In particular, the efficiency of the lower track pressure becomes increasingly apparent at higher vehicle speeds. This is due to decreasing amount of snow compaction that occurs while the snow is under the track as the speed increases. At the lower track loading there appears to exist a critical speed above which little increase in efficiency is achieved with higher speeds. For the higher pressure, significant amounts of compaction continue to occur at the higher vehicle speeds. These high pressures, even at high speeds, forces the vehicle a significant distance down into the snowpack, thereby expending much energy in snow compaction. At lower track pressures, the compaction becomes much less significant, and the vehicle tends to "ride-up" on the which is a much more efficient configuration. The relationship between the pressure and deformation is a highly nonlinear one, as evidenced by eq.

II.B.47. As a consequence, one can expect a nonlinear relationship between specific power and vehicle speed.

Notice the tremendous increase in power when the track pressure is increased from $1x10^4$ N-m^{-2} to $5x10^4$ N-m^{-2}. Again, this can be attributed to the highly nonlinear relationship between p, α, and $\dot{\alpha}$ in the constitutive equation.

Figures 17 and 18 illustrate the variation of vehicle power with initial snow density. In these figures the relationship between specific power and density is illustrated for three different vehicle velocities. As can readily be seen, for snow with initial densities above 300 Kg-m^{-3}, a track loading of 10^4 N-m^{-3} operates fairly efficiently. However, the same cannot be said for a track loading of $5x10^4$ N-m^{-2}, where good efficiencies are not achieved until an initial snow density of about 500 Kg-m^{-3} is reached.

The foregoing calculations indicate that much can be done in an analytical manner to make parametric studies of over-snow mobility. The study given here considered only volumetric effects, and as such would represent a lower bound on total energy levels absorbed by the snow when compressed by vehicle tracks. However, this estimation should be good if slipping is not significant. Central to such an analytical study is the availability of a constitutive equation which can accurately represent the material response to large compactions at high rates.

The results of the computations illustrated in the figures show an intricate relationship between the rate at which energy is absorbed by the snow and such parameters as track pressure, vehicle speed, and initial snow density. Decreasing the track pressure substantially reduces the snow density required to allow the vehicle to move efficiently through snow.

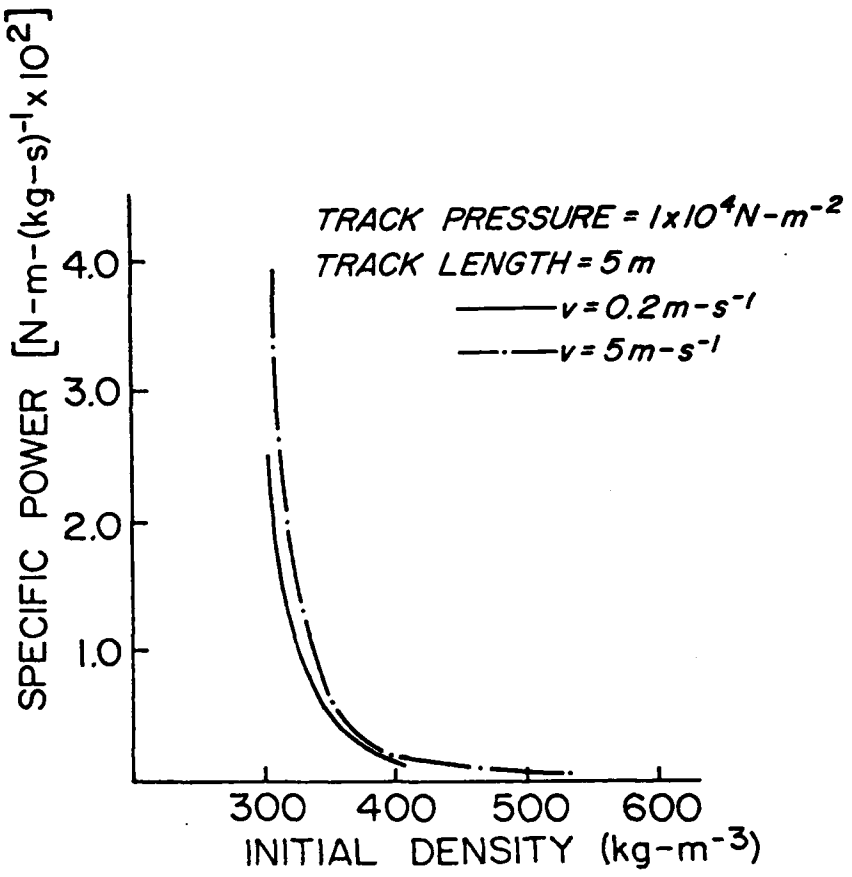

Figure 17. Effect of initial snow density on power consumption.

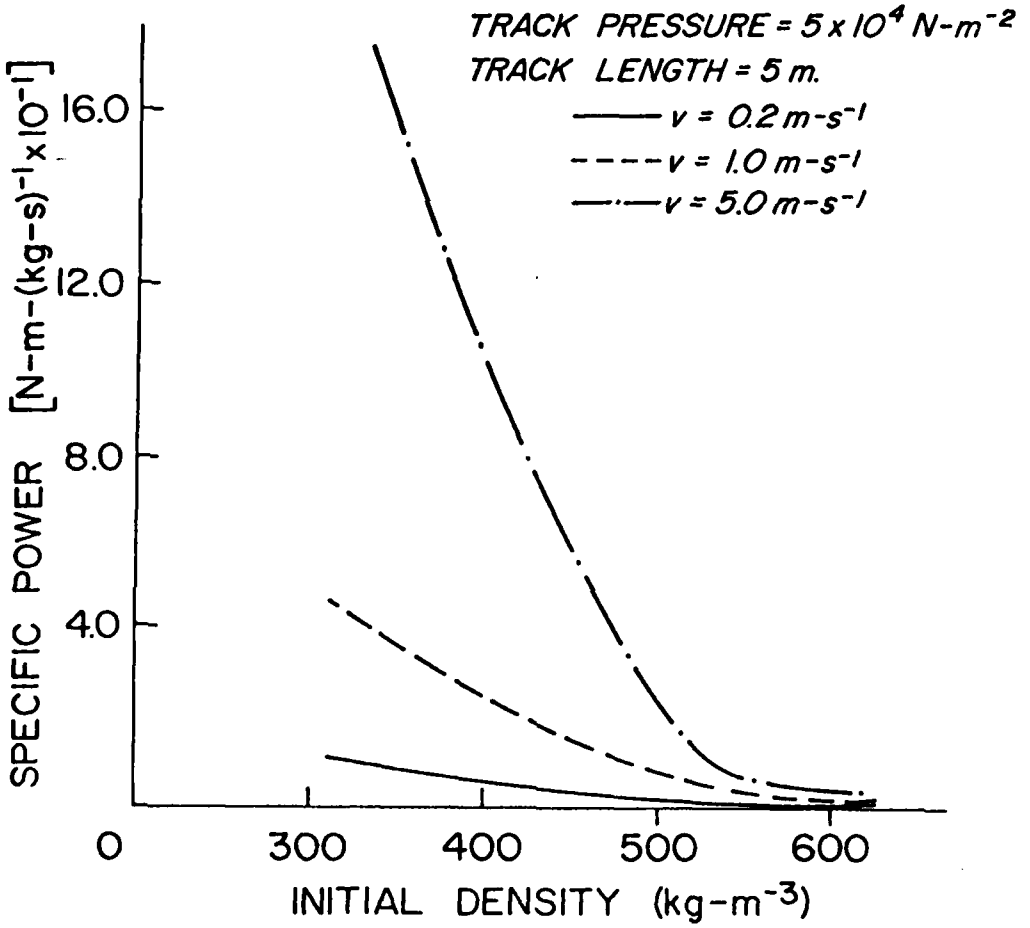

Figure 18. Effect of density on power consumption.

The same results are implied for the speed required to allow the vehicle to begin to plane out onto the surface, thereby resulting with less compaction of snow. The figures show a highly nonlinear relationship between these parameters and the power dissipation. These figures also indicate there exists critical combinations of snow density, track loading, and vehicle speed which allow efficient travel over snow.

The calculations were made by assuming a uniform compaction of the snow directly below the vehicle track, and as a consequence these calculations would be particularly accurate for shallow snowpack, in which pressure bulb reaches the ground. For deep snowpack, compaction within the pressure bulb would not be as uniform, and the results would have to be interpreted in terms of the averaged pressure within the pressure bulb. However, without knowing the shear strength of the snow along the sides of the pressure bulb, these calculations would be difficult to arrive at.

Presently, the author is working on a more comprehensive constitutive law for snow, which, when completed, should provide a more complete description of the high strain rate properties of snow. In addition to the formulation of a more comprehensive constitutive law, much more experimental data is needed so that the variation of snow properties with snow type can be determined. Density alone is not a sufficient parameter for doing this, and in-depth studies are needed to determine those structural parameters of snow which, in conjunction with density, can be used to accurately evaluate the material coefficients to make calculations such as done here more accurate. When a set of constitutive equations, such as the one presented here, are available for a wide range of snow densities and snow-types detailed studies can then be made on vehicle performance in snow for a wide range of conditions. Such studies can form guidelines for track design.

III.C TRACKED-VEHICLE MOBILITY IN DEEP SNOWPACK OF MEDIUM DENSITY

In this section, we assume the snowpack is so deep that the pressure bulb does not extend to the ground. In this case, the pressure bulb must be supported by the surrounding snowpack. This is done by means of shear stresses along the bulb walls and a normal stress along the bottom of the bulb.

Studies by Harrison (1975) have indicated that in deep snowpack the pressure bulb is usually very close to a rectangular shape. There is some spreading of the bulb below the track, but this is usually not very significant. Figure 19 shows schematically a typical shape. Often local inhomogeneous conditions or vehicle turning can cause the vehicle to significantly alter the bulb shape. However, if the vehicle is moving in a straight line, the bulb geometry depicted in Figure 19a is realistic.

Now idealize the bulb as shown in Figure 19b. The hydrostatic pressure, p in the bulb is assumed to be a function of Y and t, where Y is the vertical Lagrangian coordinate of a particle which eventually is contained in the pressure bulb at deformed position y and time t. The shear stresses along the wall and in the pressure bulb is simply the critical pressure p_c required to initiate inelastic compaction of the snow. Not shown at the lower surface is a shear stress component, which must be zero at the center of the bottom surface and which grows as the two lower corners are approached. This shear stress is felt to partly restrain the pressure bulb from spreading, since it must act inward toward the centerline of the bulb.

We consider now the Lagrangrian forms of the equilibrium equation and the continuity equation. The equilibrium equation and continuity equations are respectively

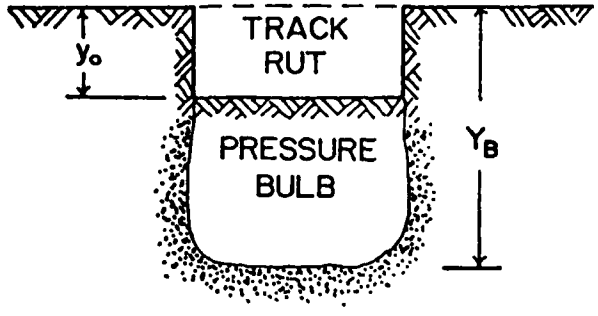

a. ACTUAL PRESSURE BULB GEOMETRY

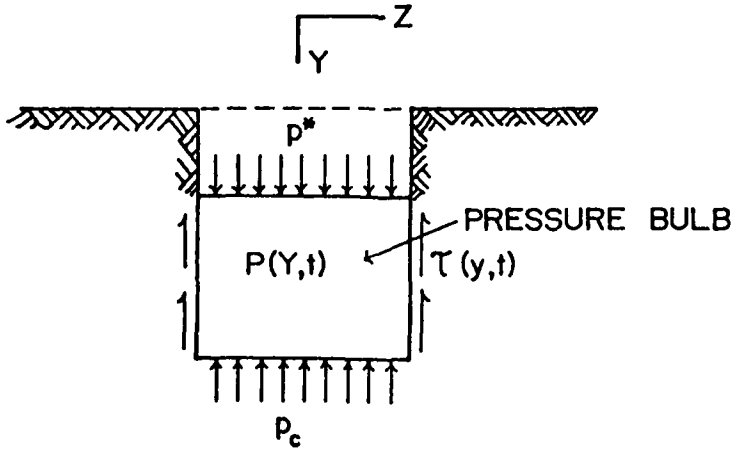

b. IDEALIZED PRESSURE BULB GEOMETRY

Figure 19. Actual and idealized pressure bulbs below vehicle track.

$$\frac{\partial T_{yy}^{\circ}}{\partial Y} + \frac{\partial T_{zy}^{\circ}}{\partial Z} = 0 \qquad \text{(III.C.1)}$$

$$\frac{d\rho}{dt} + \rho\frac{\partial v}{\partial y} = 0 \qquad \text{(III.C.2)}$$

T_{yy}° and T_{zy}° are respectively the normal and shear components of the Piola stress tensor $\underset{\sim}{T}^{\circ}$. The Piola stress tensor is related to the more familiar Cauchy stress tensor, $\underset{\sim}{T}$, by the equation

$$\underset{\sim}{T}^{\circ} = \frac{\rho_o}{\rho} F^{-1} \cdot \underset{\sim}{T} \qquad \text{(III.C.3)}$$

ρ_o is the initial density of snow, and $\underset{\sim}{F}^{-1}$ is the inverse of the deformation gradient tensor. Utilizing eqs 3 and 1 and taking advantage of the uniformity of the deformation in the Z-direction results with the following reduced form of the equilibrium equation:

$$\frac{\partial p}{\partial Y} = -\frac{2\rho_o}{\rho_m w}\alpha\tau \qquad \text{(III.C.4)}$$

where w is the width of the track, and τ is shear stress on the bulb wall. Integration of the above gives

$$p(Y,t) = -\frac{2\rho_o}{\rho_m w}\int_o^Y \alpha\,\tau dY' + p(0,t) \qquad \text{(III.C.5)}$$

where p(0,t) is the pressure produced by the surface loading.

Eq II.B.47 can be inverted to give

$$\alpha = -\int_o^t e^{Q(t',\,p,\,\alpha)}\,dt' + \alpha_o \qquad \text{(III.C.6)}$$

where

$$Q = \frac{1}{2}\left[F(t,\alpha) + \ln(\alpha(\alpha-1))\right] - \ln A \qquad \text{(III.C.7)}$$

$$F(t,\alpha) = \frac{1}{C}\left[3\alpha e^{\phi\alpha/\alpha_o}p(y,t)/\left(J\ln\left(\frac{\alpha}{\alpha-1}\right)\right) - 2\,(S_o - C)\right] \qquad \text{(III.C.8)}$$

Equations 5 and 6 can be solved simultaneously to yield the variation of α under the track. In order to solve these equations the shear stress τ must be found. In his earlier study, Mellor (1963) has studied the shear strength of snow and have shown that under sufficiently high rates, the shear stress of snow is weakly rate dependent but depends strongly on the hydrostatic pressure. In view of these results, the following form is adopted for τ.

$$\tau = \tau_o + K\, p \qquad \text{(III.C.9)}$$

Under relatively high pressures, the portion K p can be significantly larger than τ_o, so that τ_o can be neglected. The pressure variation then becomes

$$p(Y, t) = + \frac{2\,\rho_o\, K}{\rho_m\, w} \int_o^Y \int_o^t e^{Q(\alpha,\, t')}\, dt'\; p(Y', t)\, dY' + p(0,t) \qquad \text{(III.C.10)}$$

K is actually a function of the velocity of the particles on the bulb wall, but here it will be assumed constant, since the rate dependence of K is not well defined.

The continuity equation can be put in the form

$$\frac{\alpha}{\alpha_o} = \det \left|\underset{\sim}{F}\right| = \det \begin{vmatrix} 1 & 0 & 0 \\ 0 & \frac{\partial y}{\partial Y} & 0 \\ 0 & 0 & 1 \end{vmatrix} \qquad \text{(III.C.11)}$$

Integration of this results with

$$y - y_o = \int_o^Y \left(1 - \frac{\alpha}{\alpha_o}\right) dY \qquad \text{(III.C.12)}$$

y_o is simply the depth of the rut formed by the tracks, since this is the deformed position of the top surface Y = 0. At the bottom of the pressure bulb, y = Y, since there is no significant displacement at that point. Therefore, if we denote Y_B as the position of the bottom of the pressure bulb,

eq 12 gives

$$y_o = \int_o^{Y_B} \left(1 - \frac{\alpha}{\alpha_o}\right) dY \qquad \text{(III.C.13)}$$

For a given problem, eqs 6 - 13 can be solved numerically when appropriate boundary and initial conditions are specified. Assuming p (0,t) is known, eq II.B.48 is first evaluated at t=0 to find p_c, the critical yield pressure. Eq 10 then is integrated to determine the value of Y = Y_B at which p = p_c. Eq. II.B.47 is then used to find $\dot{\alpha}$ for $0 \leq Y \leq Y_B$. Then the problem is step forward integrated in time by some small time increment Δt, and the procedure is repeated. Doing this for the complete time period of track loading gives a numerical solution defining sinkage, energy consumed, α, and stress distribution and bulb depth.

The work done to the snow can easily be found by calculating the work expended by the surface pressure in compacting the snow. At the upper surface, the work is given by the expression

$$dW = p(0,t)dy(0,t) \qquad \text{(III.C.14)}$$

The work rate is then

$$\frac{dW}{dt} = p(0,t)\ \frac{dy}{dt}\ (0,t) \qquad \text{(III.C.15)}$$

This is the work rate/unit time per unit track area. Consequently the total vehicle power expended in compacting the snow is

$$P_w = \frac{A_T}{t^*} \int_o^{t^*} p(0,t)\ \frac{dy}{dt}\ (0,t)\ dt \qquad \text{(III.C.16)}$$

where A_T is the area of the vehicle track and t* is the time that the snow is under the vehicle track. This power term includes the work dissipated due to shear losses along the bulb wall as well as the energy dissipated by compaction of the snow in the bulb. Not reflected would be energy expended due to track slippage and the dissipation of energy associated with the

large deviatoric deformations in the immediate vicinity of the track grousers.

Idealize now the track pressure by the distribution shown in Figure 20b. The pressure is assumed to build up linearly to a constant peak pressure p*. This variation is given by the equation

$$p(0,t) = 0 \qquad t \leq t^*$$

$$p(0,t) = p^* \frac{t}{t_o}\,[1 - H(tt_o)] + P^*H(tt_o),\ 0 \leq t \leq t^* \qquad \text{(III.C.17)}$$

H(t) is the Heavyside step function, and t_o is the entry time, i.e. the time increment that the surface snow is in contact with the front part of the track. t_o is determined by the vehicle sinkage and speed. Figure 20b illustrates the temporal variation of p(0,t). Generally the track pressure has a periodic variation determined by the spacing and size of the track wheels. For wheels with a moderate or small spacing, this periodic fluctuation may be neglected.

The track grousers also generate stress concentrations within the snowpack in a localized region near the surface. This region will have a very complicated stress state which involves both large normal stresses and large deviatoric stresses. In this zone, a significant amount of energy is dissipated by both shearing and compaction, and the exact nature of the deformation within this area would be determined by grouser size, geometry and spacing as well as the amount of slippage and nominal track pressure.

The analysis made in this section does not have the capability of calculating the energy absorbed in this zone within the localized effect of the track grousers. Here we find the energy absorbed through compaction of the snow in the pressure bulb and the shearing deformation within the pressure bulb and along the bulb walls. As a consequence these calculations provide a lower bound on the total energy absorbed by the snow. In the absence of vehicle slipping, the shear zone in the grouser region may be neglected in comparison to the much larger pressure bulb.

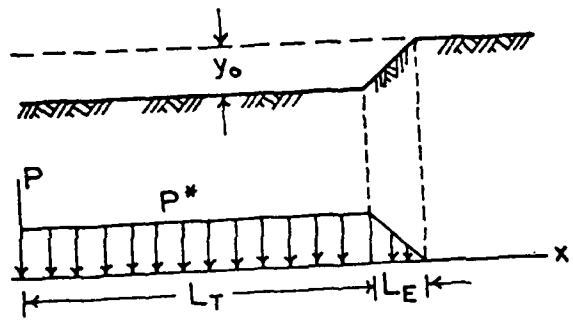

a. RUT PROFILE and PRESSURE PROFILE

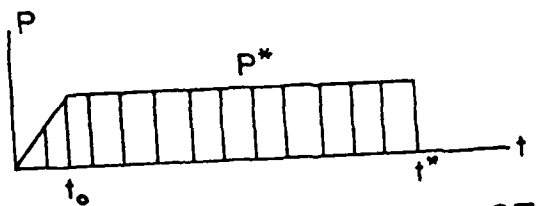

b. TEMPORAL VARIATION OF TRACK PRESSURE

Figure 20. Rut profile and pressure loading in deep snowpack.

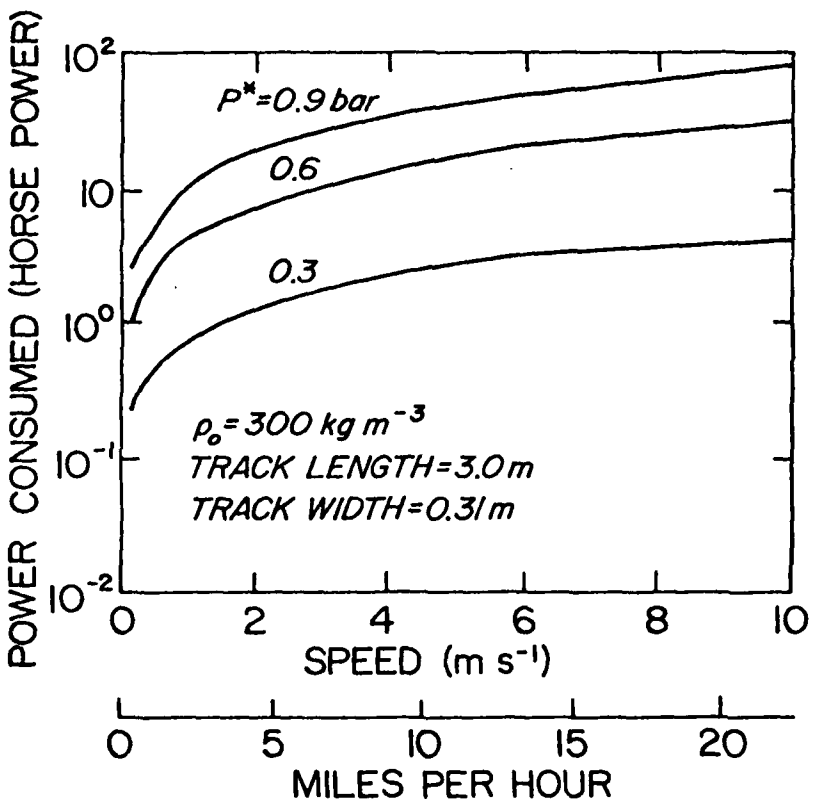

Figure 21. Effect of vehicle speed and track pressure on power consumption.

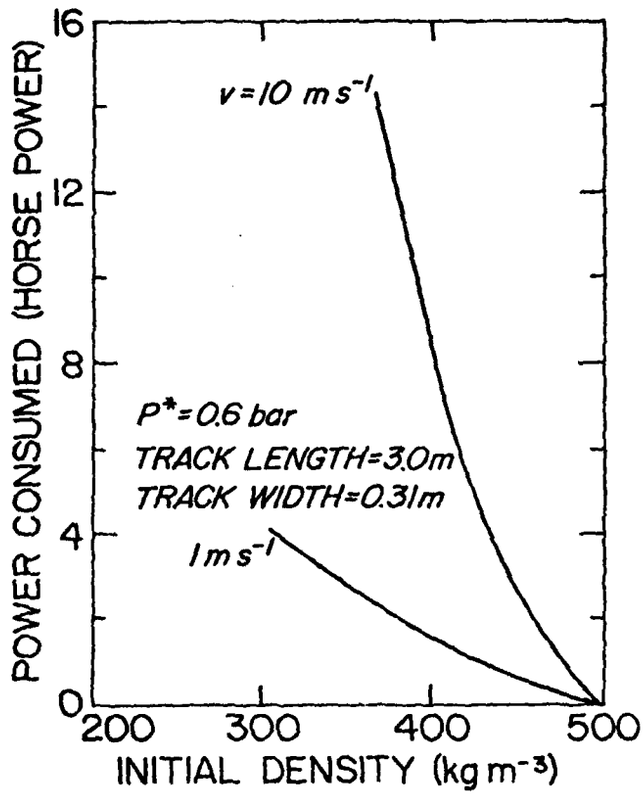

Figure 22. Effect of initial snow density on power consumption.

Vehicle performance can be determined parametrically in terms of a number of parameters, including track geometry, track pressure, vehicle speed, and snow density. By track geometry, we mean track width, length, entry length and angle of attack.

In addition to calculating vehicle power requirements, such information as sinkage, bulb depth, and density and pressure profile within the bulb can be found. Not all of this will be done here, since this would require too much space, and the main interest is the evaluation of power requirements.

The basic track geometry and vehicle weight chosen for the calculations are those of the Ordinance M5A4 high-speed tractor. This vehicle was originally designed for transporting personnel and light cargo over soft terrain. The M5A4 has a 235 horsepower gasoline engine, weighs about twelve tons, and has a track length of about 3.0 meters and a track width of 0.31 meters. The nominal track pressure varies from 0.43 bar upward, depending on the load. Consequently the M5A4 does not have good capability for operating in deep seasonal snowpack but does have a reasonable mobility in perennial snowpack such as on the Greenland icecap or on medium density seasonal snow. Generally these densities are in excess of 300 $Kg\text{-}m^{-3}$.

Figures 21-27 summarize the results of this study. The results are shown in terms of horsepower, since this is the most recognizable unit of power. The track pressures considered were for the most part larger than 0.2 bars, since for medium-to-high density snow, track pressures below 0.2 bars result with insignificant energy levels consumed in the pressure bulb.

Figures 21 and 22 illustrate the very strong dependence of energy consumption on initial density and nominal track pressure. For instance by merely increasing the pressure from 0.3 bars to 0.9 bars, an increase of an order of magnitude in energy consumptin results for snow with a density of

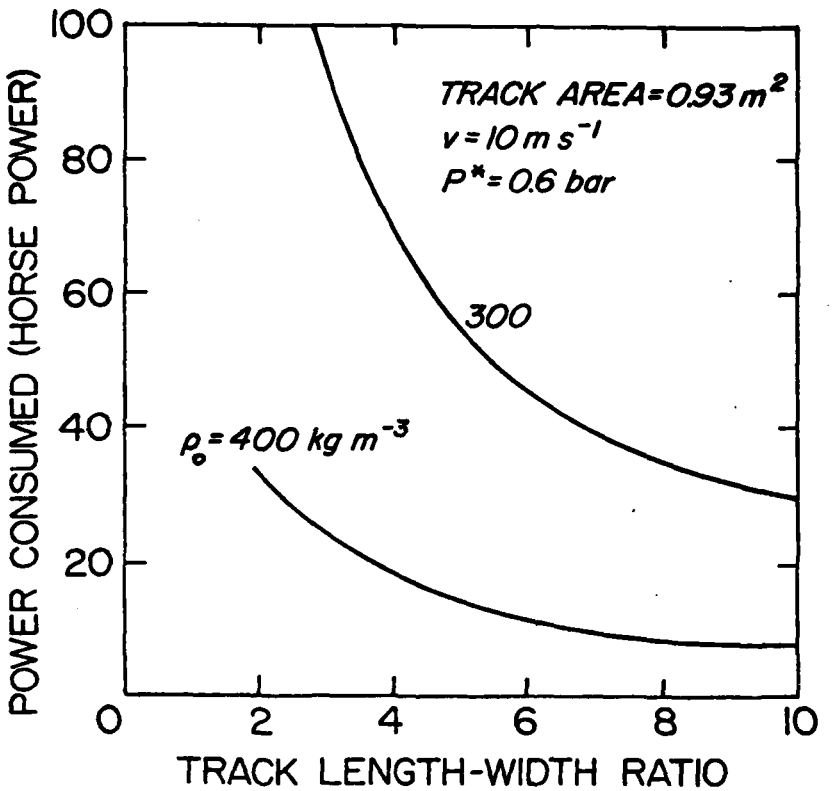

Figure 23. Variation of power consumption with track geometry.

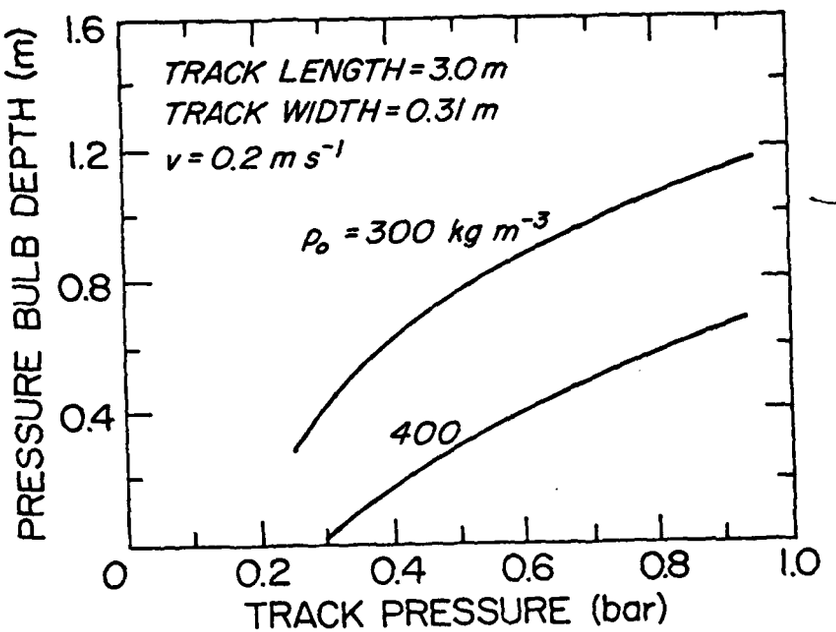

Figure 24. Effect of track pressure and initial snowpack density on pressure bulb depth.

300 Kg-m^{-3}. Conversely snow with an initial density of 500 Kg-m^{-3} consumes only about 10% as much energy as snow with an initial density of 300 Kg-m^{-3}, as shown in Figure 5. As indicated by Brown (1978b) and evidenced in Figure 22, for a given pressure P*, there exists a critical density above which very little compaction and energy consumption takes place. Figure 22 shows that for a density above 450 Kg-m^{-3} a track pressure of 0.6 bar produces very little compaction.

Figure 23 demonstrates the effect of track geometry on track efficiency. The M5A4 has a length-width ratio of about 10, but Figure 23 shows how energy consumption would vary for a L/w variation from 2 up to 10. This figure shows the obvious advantage of a long narrow track. The reason for this dependence lies in part with the role that the shear stress plays in supporting the pressure bulb. One can readily see by Figure 19 that for a wide track, the pressure bulb would have to be deeper in order for the wall shear stresses to support the bulb. This can also be seen by noting eq 4 in which the track width w inversely affects the pressure gradient in the bulb. An increased w decreases $\partial p/\partial y$, thereby increasing the depth to which the bulb penetrates before the bulb pressure decreases to the critical yield pressure p_c.

Figure 24 shows the variation of bulb depth with track pressure for three initial snow densities. As should be expected, bulb depth decreases with decreasing pressure and increasing density. The variation of bulb depth with track length-width ratio is illustrated in Figure 25, and Figure 26 gives the vertical variation of bulb pressure for one particular case. As can be seen, the dpeth is critically dependent on the value of p_c, the yield pressure given by eq. II.B.48. Over the bottom 0.4 meters of the bulb, the pressure p goes through a relatively small variation, so changing

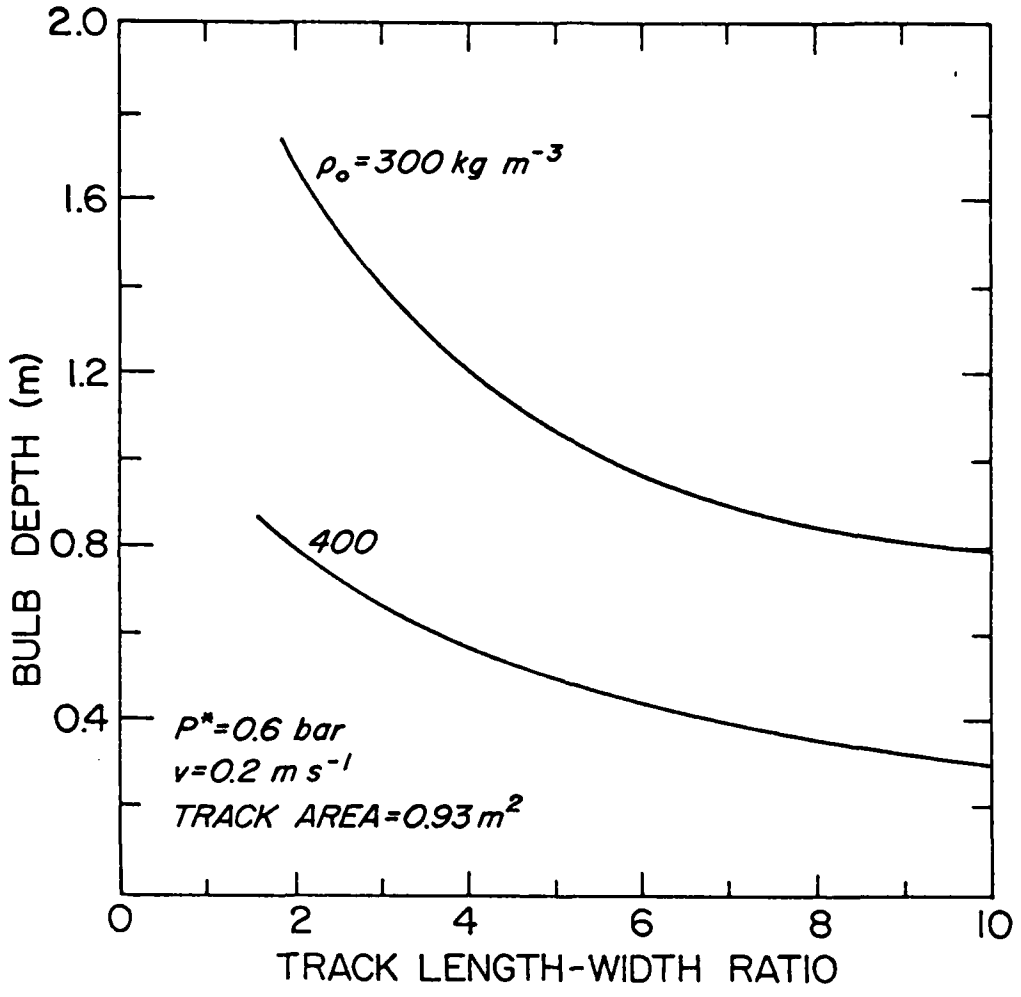

Figure 25. Effect of track geometry on bulb depth.

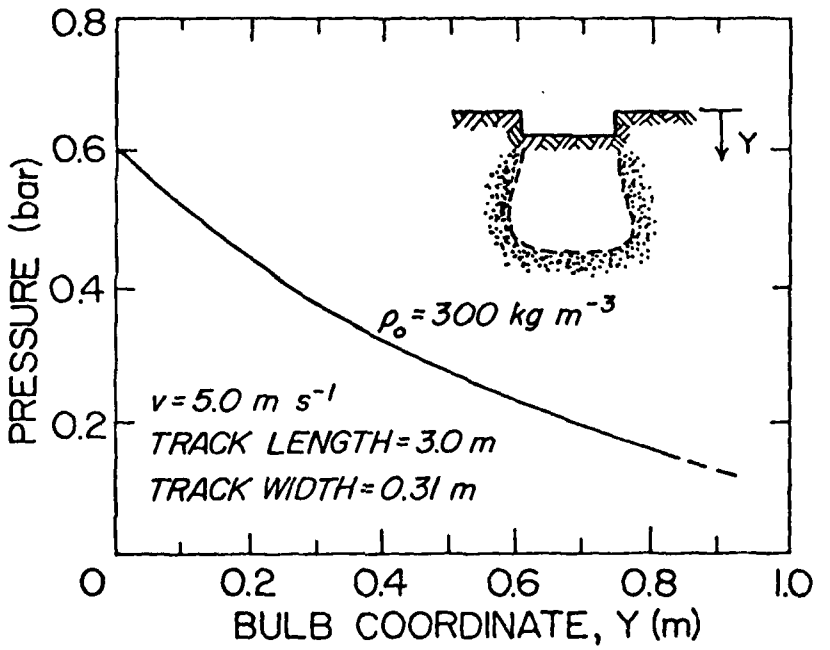

Figure 26. Typical pressure distribution in pressure bulb.

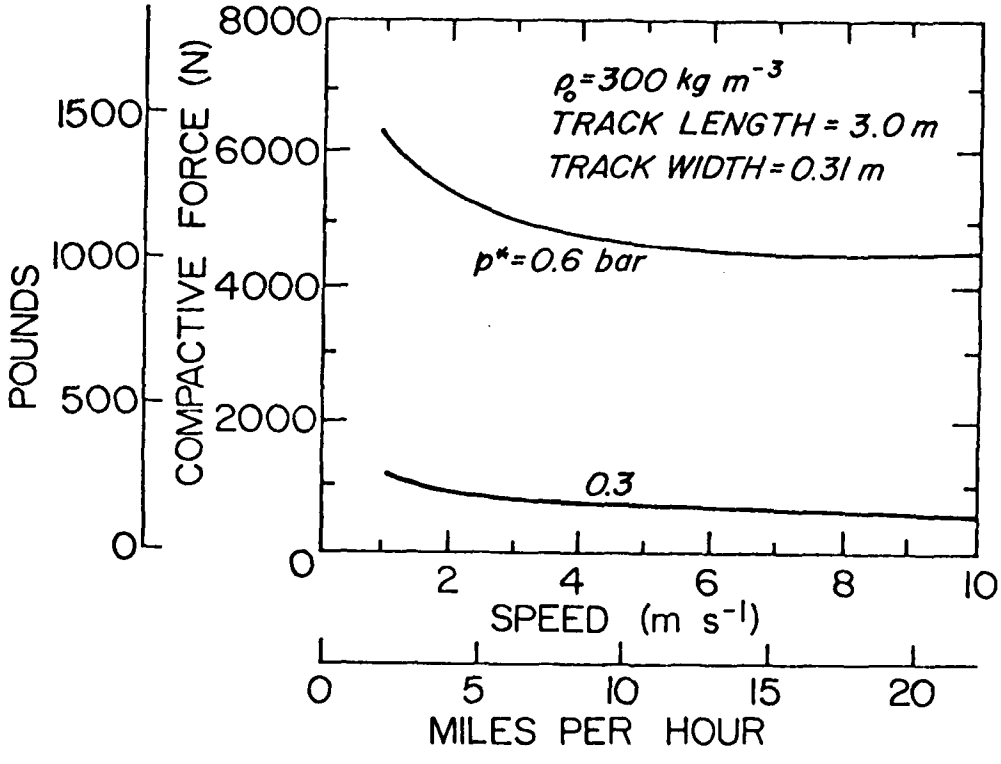

Figure 27. Variation of compactive force with vehicle speed.

p_c by 50 to 100% could case a significant change in the bulb depth. This, however would not affect power consumption much, since most of the energy is consumed in the upper portion of the bulb.

Finally, Figure 27 shows the compactive force generated by the motion of the vehicle in the snow. This was obtained by integrating the horizontal component of the track pressure over the track area. Note here the improvement of track efficiency with vehicle speed.

The results of this study show that the method described here has the potential of predicting power requirements of oversnow vehicles for a wide range of conditions. For example the formulation developed here enables one to make a parametric study of the effect of a large number of factors on energy consumption rate. This includes such factors as nominal track pressure, length-width ratio, snow properties, angle of attack, etc. Therefore this formulation could be of some use as an analysis and design tool.

The calculations used in the example were for snow with a uniform density and a track which develops a uniform track pressure. Such an assumption is not necessary, and a stratified snowpack and nonconstant track pressure could have been used. However, to demonstrate the formulation, the simpler problem was considered here.

Presently there is not much data available for comparison with the example given here. Harrison (1975) has detailed results for several vehicles in seasonal snowpack in which th snow density in the upper 50 cm were less than 300 Kg-m^{-3}, which makes direct comparison with the example given here difficult. The constitutive law given in eq II.B.47 is not considered to be accurate for densities less than 300 Kg-m^{-3}, so consequently an example for lower density snow was not possible.

The general behavior of the results demonstrated in Figures 21-27 agree with what has been observed in field studies reported by Harrison (1975). Whether or not there is a good quantitative agreement will be determined when either new field data is available or when the model developed here has been generalized to include conditions of lower density snow. What has been demonstrated, however, is the apparent usefulness of this model for design and analysis purposes.

III.D VEHICLE PERFORMANCE UNDER DIFFERENT SNOWPACK CONDITIONS.

In the previous two sections, vehicle performance was evaluated for dry snowpack with densities greater than 300 Kg m^{-3}. The pore collapse equation was used for these calculations, since it is valid for this type of snow and is relatively easy to use.

In this section the neck growth model is used. This allows an evaluation of vehicle performance in low density snow as well as higher density snow. In addition, since grain size and bond diameter can be varied, the effects of snow type can be studied.

Normally a vehicle will have to be operated under a variety of snowpack conditions. For instance during mid winter, operation on low density dry snowpack may be required, whereas during the spring, unsaturated wet snow will be incurred. It would be useful to be able to predict how much variations in snowpack conditions affect vehicle performance.

Recently Abele (1981) has investigated the volumetric properties of wet snow. Of particular interest is his work on unsaturated snow (free water content less than 8% by volume). A volumetric constitutive law for this snow (Brown, unpublished) has been developed and could be used in a number of problems of interest. This constitutive equation has a form similar to the pore collapse model developed earlier, i.e.

$$p = \frac{Je^{-\phi\alpha/\alpha o}}{3\alpha}\left[2(So - C) + C \ln\left(\frac{(\dot{\alpha}\, A)^2}{\alpha(\alpha-1)}\right)\right] \qquad \text{(III.D.1)}$$

which is essentially the same equation as was used to describe the behavior of high density snow (Brown, 1979). Abele (1980) indicates that wet snow is somewhat more rate dependent than dry snow, and that the material is somewhat softer than dry snow at the same density. Also the work hardening term ϕ was found to be dependent on the free water content. Utilizing Abele's experimental results, eq 11 was used to approximate the properties of wet snow with essentially no free water and wet snow with 7% free water by weight. It should be noted that to date, Abele's data is the only high rate test data for wet snow, so the constitutive equation given by eq 11 cannot be expected to be extremely accurate. There just is not yet enough data to thoroughly verify the accuracy of any equation. However, the results found here for wet snow should give a good qualitative evaluation of mobility in wet snow.

A procedure essentially the same as used in the earlier two sections can be used to analyze vehicle performance, so only the results are given here. The same track loading is assumed here as was assumed in Section III.C.

For dry snow, a range of densities from 200 Kg m^{-3} to 500 Kg m^{-3} were evaluated for speeds ranging from 1 ms^{-1} to 10 ms^{-1}. Also the effect of track pressure on vehicle power requirements was also investigated. These results are all illustrated in Figures 28-32. The unit of power used here is horsepower as it is more familiar to people. Figure 31 illustrates the effect of snow type on vehicle performance in snow. Plotted in that figure is the variation of vehicle horsepower with the ratio Δ/R. For well sintered mid-season snowpack, the mean radius, r, is on the order of 0.1 mm, whereas Δ may average as large as 0.04 mm. However, snow which has been under temperature gradient effects will metamorphose until the grain size R may be as large as 2 mm.

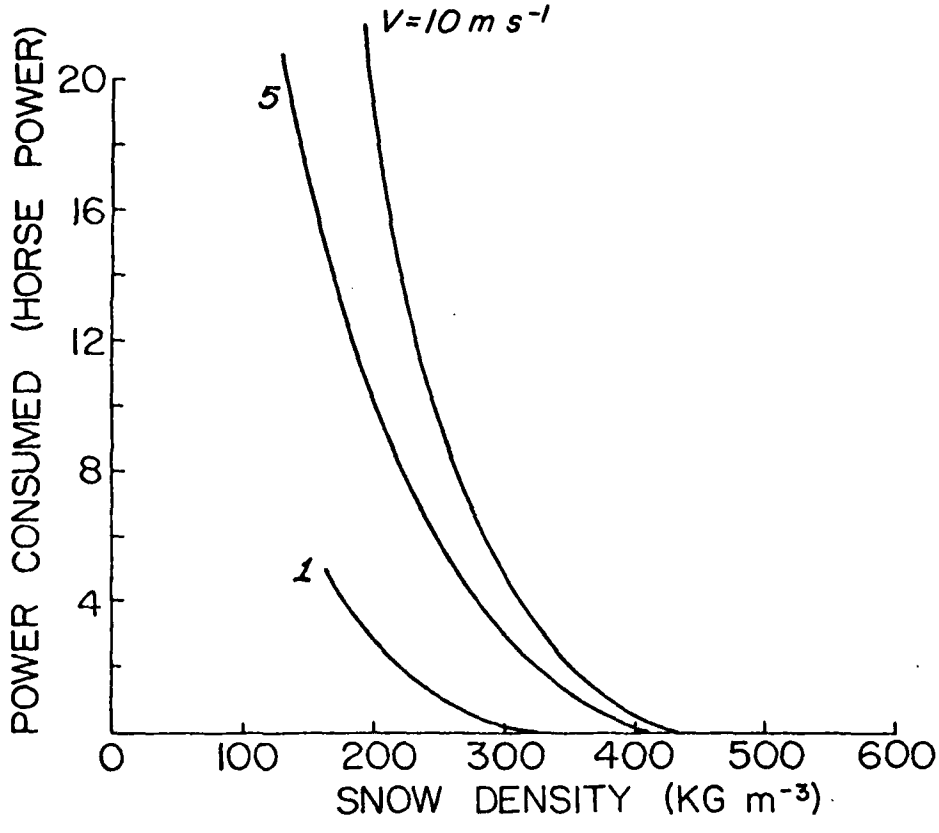

Figure 28. Dependence of power consumption on initial snow density for three vehicle speeds.

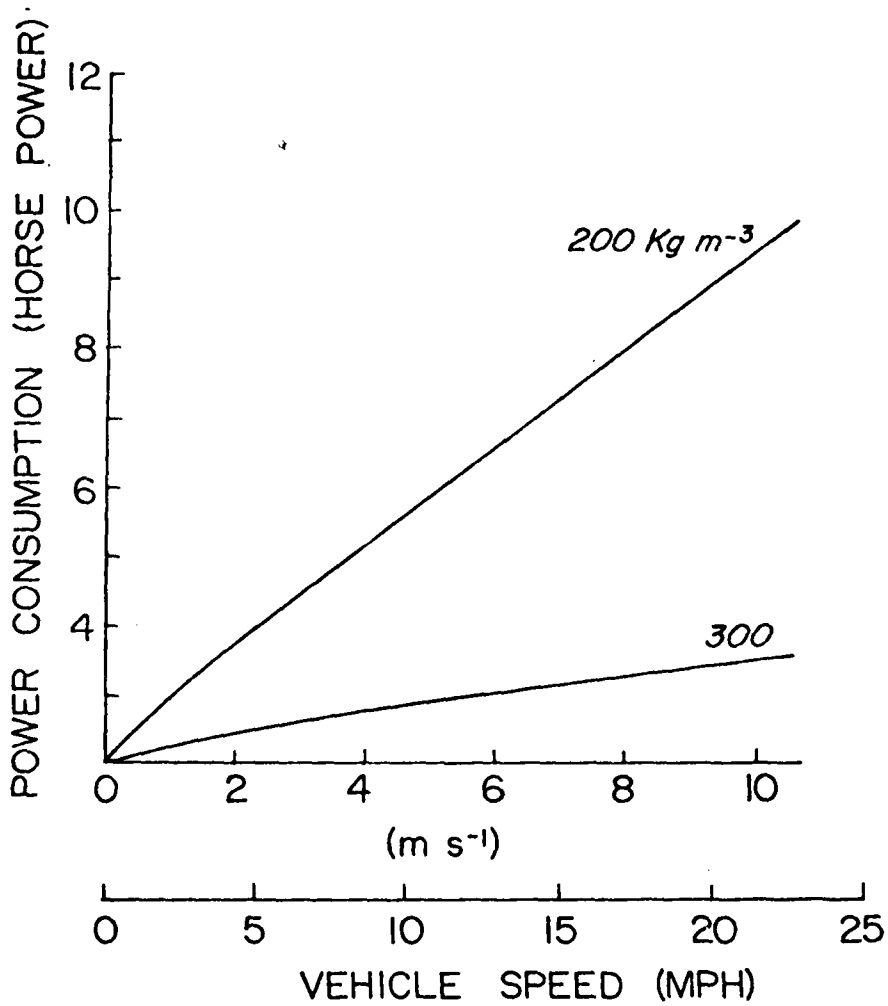

Figure 29. Effect of density and vehicle speed on power consumption on low density dry snowpack.

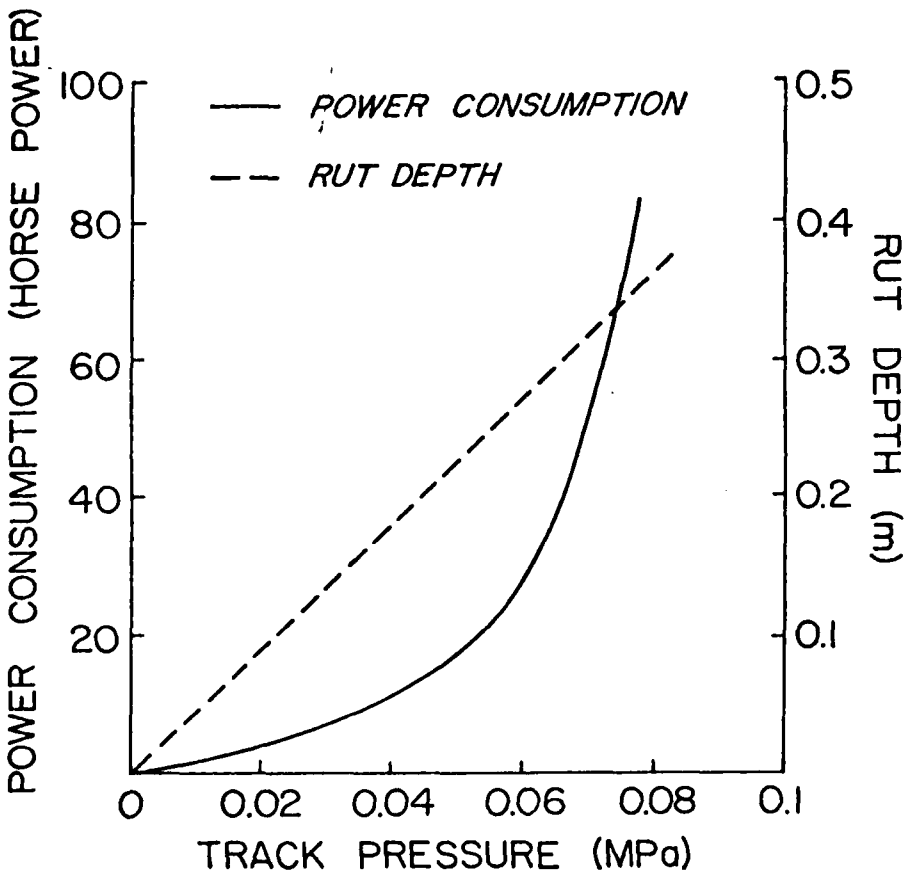

Figure 30. Power consumption and rut depth variation with track pressure.

A relative comparison of vehicle power requirements in wet snow and dry snow is illustrated in Figure 32 where results are shown for wet snow with 0% free water and 7% free water. A density of 400 Kg m^{-3} was chosen since late season wet snow usually has a density in excess of 400 Kg m^{-3}. For the wet snow, eq 1 was used in evaluating the vehicle performance.

Figure 28 shows the dramatic increase in energy requirements with decreasing snowpack density. The sinkage increases significantly, and this additional sinkage increases the thrust required to push the snow just ahead of the track downward and forward as the track passes over the snowpack. Comparisons in Figure 28 are for two vehicle speeds while such parameters as intergranular bonding were kept constant.

One additional point should be made here. As rut depth increases, the forward thrust applied by the tracks also must increase. This results with an increased shearing force applied to the snowpack in a direction parallel to the direction of vehicle travel. This increased shearing force results with additional horsepower consumption within the snowpack and would have to be added to the numbers arrived at here since shearing effects were not included in the analysis. Consequently, the solution found here should represent a lower bound on the actual energy consumed within the snowpack. Studies with W. Harrison of the U. S. Army Cold Regions Research and Engineering Laboratory show that shearing effects are not significant as long as the vehicle is not experiencing slippage.

Figures 29 and 30 show that power consumption increases rapidly with track pressure but that when a critical vehicle speed is reached, vehicle travel becomes relatively efficient. This critical speed depends on snowpack density, track pressure and intergranular bonding.

Finally the variation of vehicle power required for travel in temperature gradient snow increases dramatically as the temperature gradient effects become more significant. Mid season equi-temperature snow is the predominant snow type for normal snowpack. For instance in a two meter deep snowpack, a full .5 meters may consist of this snow type. Grain size is normally 0.1 - 0.3 mm in diameter, and intergranular bonding is well established, the ratio Δ/R often being on the order of 0.3 to 0.5. However, under the influence of a temperature gradient, grain size increases. This rate of increase depends on temperature, so that the metamorphism proceeds most quickly near the bottom of the snowpack where the temperatures are normally above -5°C. Quite often in a one meter early season snowpack which experiences a cold period, the entire snowpack can show these temperature gradient effects. It is certainly possible that the ratio Δ/R could decrease to values less than 0.1 to produce very weak, collapsing snowpack.

Future work needs to be directed at the more difficult problem of energy consumption when vehicle slippage occurs during travel. Current finite element and finite difference methods may be used to solve this problem if the relevant material properties of the snowpack are known. Unfortunately these material properties are still not available. Brown (1981) has used a nonlinear constitutive relation to model sinkage of building foundations into snow. This constitutive equation has the form

$$\underset{\sim}{\bar{T}} = 2\eta \quad \underset{\sim}{C}^{-1}\dot{\underset{\sim}{E}}(\underset{\sim}{C}^{-1})^{T} - \frac{2\eta}{3}\,\mathrm{tr}(\underset{\sim}{C}^{-1}\dot{\underset{\sim}{E}})\ \underset{\sim}{C}^{-1} \qquad \text{(III.D.2)}$$

$$- \frac{\rho_o}{\rho}\, p\ (\alpha,\dot{\alpha})\ \underset{\sim}{C}^{-1}$$

where $\underset{\sim}{C}^{-1}$ is the inverse if the deformation tensor, $\underset{\sim}{E}$ is the Lagrangian strain tensor, $\underset{\sim}{\bar{T}}$ is the second Piola stress tensor, and η is a viscosity coefficient

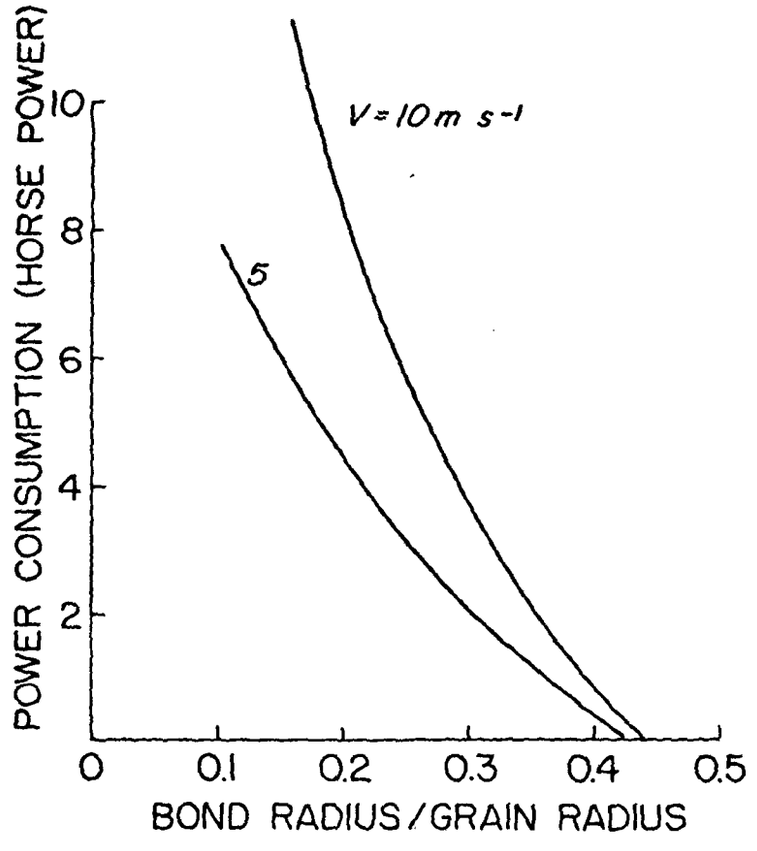

Figure 31. Effect of snowtype on power consumption in deep snowpack.

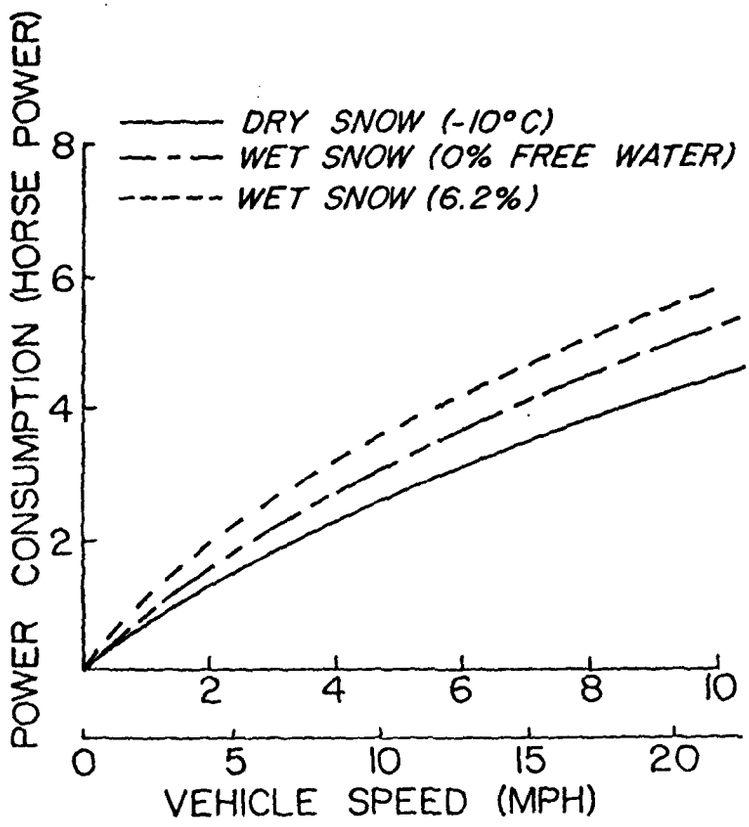

Figure 32. Comparison of power requirements for wet snow and dry snow.

which is density dependent. The pressure term is a function of α and $\dot{\alpha}$ and is given by eq II.B.47. For the settlement problem, this formulation was found to work well. Generally strain rates less than $10^{-4}s^{-1}$ were incurred in the problem. Whether or not it would work at all well for higher strain rates associated with vehicle mobility has not been determined. Also the constitutive equation is somewhat complicated, and it should be possible to formulate a simpler constitutive equation for the vehicle mobility problem. At any rate, if an accurate representation of the deformation in the bulb below the track is to be determined for conditions where vehicle slippage is occurring, a more general equation than used in this paper is needed. Assuming an acceptable constitutive relation for snow can be found, solution procedures similar to that of Yong et al (1978) can be performed. Yong's work to date represents the best numerical work on this type of problem. Their approach would have to be modified to account for large snowpack strains and somewhat more complicated material properties, but their finite element approach should give useable results.

IV APPLICATION TO SHOCKWAVE PROPAGATION

IV.A INTRODUCTORY REMARKS

Stress waves in snow are a problem that has not been studied as extensively as other subjects. Practically all of the previous work on the mechanical properties of snow has been restricted to quasi-static conditions in which inertial effects are negligible. Napadensky (1964) first investigated the dynamic properties of snow under the effects of shock waves. More recently, Johnson (1978) considered in detail the propagation of elastic sonic waves in snow. Wakahama and Sato (1977) Wisotski and Snyder (1964), and Gubler (1977) all conducted experimental investigations of stress waves in snow. Mellor (1977) reviewed previous work on shock waves in snow, as did Johnson (1978). But to date virtually no work performed has utilized a material constitutive equation to investigate the propagation of inelastic stress waves in snow. This is not surprising, since a valid constitutive law for snow has been lacking, and consequently previous studies have been restricted to the use of mass and momentum balance principles. However, once a constitutive law is found to accurately describe the behavior of snow under rates of loading characteristics of stress waves, a much more detailed analysis of stress waves can be made.

A number of problems require a detailed knowledge of the response of snow to shock waves. The relative effectiveness of in-snow and airborne explosives for initiating avalanches is one such example. To date the relative effectiveness of explosives detonated in the air, or in snowpack, or on the ground has not been determined. Avalanche experts still do not agree on optimum explosive speed or charge size. Another case in which stress waves are generated is projectile impact. A related problem is avalanche impact on structures. In all of these problems, solution of the

usual balance principles can yield some information; but without an appropriate constitutive law, such questions concerning stress wave attenuation or alteration of stress wave profile cannot be answered.

At this point some definitions are in order. An elastic wave is one in which no internal dissipation takes place. The material responds elastically to the stress wave, and no attenuation can be attributed to inelastic deformation of the material. A plastic wave is one in which material yielding and viscous flow occur. This is often referred to as a nonlinear wave. This is an inexact definition, however, since material nonlinearity can occur in the absence of material yielding and plastic flow. However, since at high deformation rates snow remains practically linear up to the point where yielding begins, any differentiation between plastic waves and nonlinear waves is meaningless.

In stress waves, the jump in a variable (such as strain, pressure, and energy) is defined as the difference between the values of the variable just in front of and behind the wave front. Much of the previous analytical work on stress waves has been restricted to the determination of these jumps. A shock wave is a wave in which the displacement of a particle is continuous across a wave front but in which the particle velocity experiences a jump. An acceleration wave is one in which the particle velocity and displacement are continuous across a wave front, but in which the acceleration has a jump across the wave. The surface representing a wave front is often referred to as a singular surface, since discontinuities in acceleration and/or velocity can occur at this surface.

A steady wave is defined here as one in which the wave speed propagates at a constant speed V. One can show that the wave amplitude remains constant for such a wave. Even in plastic waves such a condition can be established,

although generally this condition is short-lived. Steady waves have been studied extensively since they are mathematically easy to investigate. Nonsteady waves are simply those waves that lack the characteristics of steady waves; i.e., their amplitudes may either grow or attenuate.

IV.B GOVERNING EQUATIONS FOR PLANE SHOCKWAVES

In the following sections, differentiation of the constitutive law will be necessary. This can be done in terms of the moduli:

$$E_T = \frac{-\partial p}{\partial \alpha} \quad (\alpha, \dot{\alpha}, \ddot{\alpha}) \tag{IV.B.1}$$

$$E_1 = \frac{\partial p}{\partial \dot{\alpha}} \tag{IV.B.2}$$

$$E_2 = \frac{\partial p}{\partial \ddot{\alpha}} \tag{IV.B.3}$$

E_T, E_1, and E_2 are, respectively, the tangent, rate, and acceleration moduli. The derivatives $\partial p/\partial X$ and dp/dt then can be shown to have the forms:

$$\frac{\partial p}{\partial X} = -E_T \frac{\partial \alpha}{\partial X} + E_1 \frac{\partial \dot{\alpha}}{\partial X} + E_2 \frac{\partial \ddot{\alpha}}{\partial X} \tag{IV.B.4}$$

$$\frac{dp}{dt} = -E_T \dot{\alpha} + E_1 \ddot{\alpha} + \dot{E}_2 \ddot{\alpha} \tag{IV.B.5}$$

where X is a coordinate variable.

Consider now balance laws for stress waves. We use here strictly a mechanical theory and do not study restrictions invoked by the energy law or the second law of thermodynamics. The two laws we consider are those of mass balance and momentum balance.

The momentum balance for a plane wave propagating in the X direction requires

$$\frac{\partial \sigma_x}{\partial X} + \rho_0 b_0 = \rho_o \frac{\partial v}{\partial t} \qquad \text{(IV.B.6)}$$

where b_0 is the body force acting in the X direction and v is the particle velocity.

If the state of stress is dominated by the pressure p, and if body forces are negligible, eq 6 can be reduced to:

$$-\frac{\partial p}{\partial X} = \rho_0 \frac{\partial v}{\partial t} \qquad \text{(IV.B.7)}$$

The mass balance equation (or continuity equation) is

$$\frac{\rho_0}{\rho} \frac{\partial \rho}{\partial t} + \frac{\partial v}{\partial X} = 0 \qquad \text{(IV.B.8)}$$

Since $\alpha = \rho_m / \rho = \rho_0 \alpha_0 / \rho$, we can get

$$\frac{\partial v}{\partial X} = \frac{1}{\alpha_0} \frac{\partial \alpha}{\partial t} \qquad \text{(IV.B.9)}$$

as the form of the mass balance equation which is used later.

Consider a one-dimensional stress wave propagating through a medium such as snow. We define as a wave (or wave front) a smooth one-parameter family of points Y(t), $\infty, < t < \infty$, such that Y (t) gives the material point (or particle X) at which the wave is located at time t. X is the position of a particle in the reference configuration, which here will be the undeformed configuration. x = x(X,t) is the position of a particle X at time t and is therefore the deformed position. The intrinsic velocity of the wave is

$$V = \frac{d}{dt} Y(t) \qquad \text{(IV.B.10)}$$

which is the velocity of propagation relative to the undeformed position of the body.

Let f be any variable, say density or stress. Assume f(X,t) is a function of position X and time t and is of class C_2 in X and t except at X = Y, where f has a jump on discontinuity; i.e., the values of f just in front of and behind the wave front (X = Y) have different values. We denote this jump by the expression [f], or

$$[f] = f^- - f^+ \tag{IV.B.11}$$

where

$$f^- = \lim_{\substack{X \to Y \\ X < Y}} f(X,t) \tag{IV.B.12}$$

$$f^+ = \lim_{\substack{X \to Y \\ X > Y.}} f(X,t) \tag{IV.B.13}$$

f^+ and f^- represent, respectively, the values of f just in front of and just behind the wave front. For instance, in a shock wave we would have $[v] \neq 0$, $[\dot{v}] \neq 0$, and $[x] = 0$; i.e., the particle acceleration would undergo a jump across the shock wave, but particle position would not. The above equations were all defined with the assumption that V > 0, so that the wave is propagating in the positive coordinate direction.

Now, consider derivatives of [f], since these will be used later in the analysis of shock waves. Assume f(X,t) has a jump discontinuity at the wave front, X = Y(t), but otherwise is continuous and differentiable. Thus, clearly the jump [f] is a function of time only through the position X = Y(t). The derivative of [f] follows from the definition of the jump:

$$\frac{d}{dt}[f] = \frac{d}{dt}\Big(f(Y^-(t), t) - f(Y^+(t), t)\Big)$$

AD-A108 032 MONTANA STATE UNIV BOZEMAN DEPT OF CIVIL ENGINEERING--ETC F/G 8/12
AN INVESTIGATION OF THE HIGH RATE VOLUMETRIC PROPERTIES OF SNOW--ETC(U)
NOV 81 R L BROWN DAAG29-78-G-0089

UNCLASSIFIED ARO-15413.9-GS NL

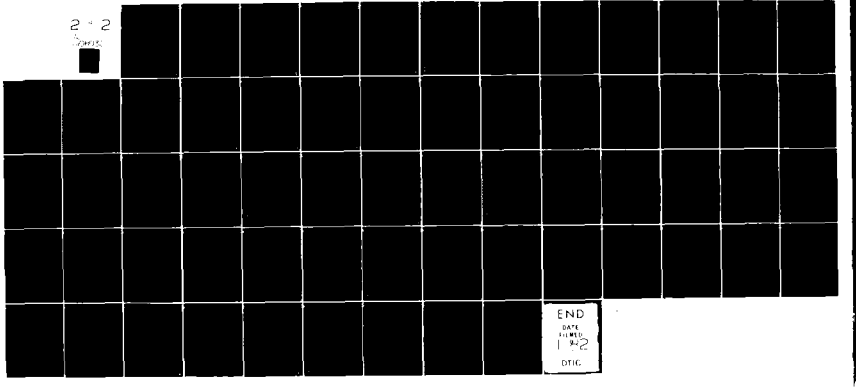

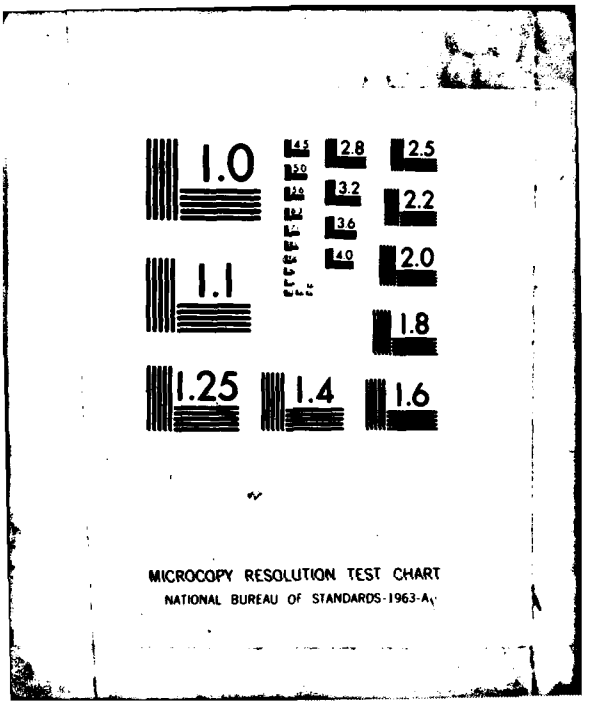
1.0
1.1
1.25
1.4
1.6
1.8
2.0
2.2
2.5
2.8
3.2
3.6
4.0
4.5
5.0
MICROCOPY RESOLUTION TEST CHART
NATIONAL BUREAU OF STANDARDS-1963-A

$$= \frac{\partial f(Y^-,t)}{\partial X}\frac{dY}{dt} + \frac{\partial f^-}{\partial t}$$

$$= \frac{\partial f(Y^+,t)}{\partial X}\frac{dY}{dt} - \frac{\partial f^+}{\partial t}$$

from which we get

$$\frac{d}{dt}[f] = V\left[\frac{\partial f}{\partial X}\right] + \left[\frac{\partial f}{\partial t}\right] \qquad \text{(IV.B.14)}$$

However, if we assume f is continuous across the wave front, then [f] = 0, and eq 14 gives

$$V\left[\frac{\partial f}{\partial X}\right] = -\left[\frac{\partial f}{\partial t}\right] \qquad \text{(IV.B.15)}$$

Equation 15 places restrictions on the jumps in the derivatives of f if f is continuous at Y. Equation 15 is called Maxwell's theorem, although both eq 14 and 15 are also often referred to collectively as the compatibility conditions for singular surfaces.

The compatibility equations can now be applied to the balance laws. Recalling that a shock wave generates jump discontinuities in $v, \dot{v}$, and $\partial v/\partial X$, whereas x is continuous across the wave, Maxwell's theorem gives

$$[v] = -V\left[\frac{\partial x}{\partial X}\right] \qquad \text{(IV.B.16)}$$

To calculate the pressure jump across a pressure wave, integrate eq 7 from X_α to X_β, where $X_\alpha < Y(t) < X_\beta$, to obtain

$$-p(X_\beta,t) + p(X_\alpha,t) = \frac{d}{dt}\int_{X_\alpha}^{X_\beta} \rho_0 \dot{x}\, dX$$

Or, by breaking the integral on the right-hand side into two parts, we get

$p(X_\alpha, t) =$

$$-p(X_\beta,t) + p(X_\alpha, t) =$$

$$\frac{d}{dt}\left(\int_{X_\alpha}^{y(t)} \rho_0 \dot{x}\, dX + \int_{y(t)}^{x_\beta} \rho_0 \dot{x}\, dX\right) \qquad \text{(IV.B.17)}$$

Now, taking the limits of $X_\alpha \to Y^-(t)$, $X_\beta \to Y^+(t)$, and using eq 16 and Leibnitz's rule to differentiate the integral on the right-hand side, we obtain

$$[p] = \rho_0 V [\dot{x}] = p_0 V [v] \qquad \text{(IV.B.18)}$$

This equation is a familiar jump equation that relates the pressure jump across the wave to the jump in the particle velocity and wave speed. A similar procedure applied to eq 9 results in

$$[v] = \frac{-V}{\alpha_0} [\alpha] \qquad \text{(IV.B.19)}$$

Therefore, we see that the material has a jump in α if the wave is a shock wave, since [v] is nonzero. Combining eq 18 and 19 gives

$$[p] = -\frac{p_0 V^2}{\alpha_0}[\alpha] \qquad \text{(IV.B.20)}$$

which is a well known relationship for shock waves relating pressure jump across a wave to the jump in density ratio.

Evaluating eq 7 both ahead of and behind the wave front, then letting X approach Y(t) and subtracting these two forms of eq 7 lead to:

$$\left[\frac{\partial p}{\partial x}\right] = -\rho_0 [\dot{v}] \qquad \text{(IV.B.21)}$$

Equations 18-21 are all widely recognized jump equations for stress waves and are applicable to both steady and nonsteady waves.

We now analyze in detail the propagation of steady waves before considering the details of nonsteady stress waves.

IV.C. STEADY SHOCK WAVES IN SNOW

To investigate further the properties of steady waves we now return to the jump equations, eq IV.B.18-21. If the material is at rest just prior to the stress wave arrival, the jumps [p] and [v] equal the values of p and v as the wave passes. Denoting the steady values of α and p behind the wave by the asterisk, *, eq IV.B.18. IV.B.21 can be put in the following respective forms:

$$\alpha^* = \alpha_0 - \frac{\alpha_0}{\rho_0 v^2} p^* \qquad \text{(IV.C.1)}$$

$$v^* = \frac{1}{\rho_0 v} p^* \qquad \text{(IV.C.2)}$$

From here on an asterisk will denote the value of a variable behind the wave, i.e., in the steady condition after the wave has passed. The terms v, α, and p refer to the values of the respective variables at any point in the wave. As indicated earlier, eq 1 and 2 result strictly from consideration of the balance principles and do not involve the material properties in any way. We now investigate the effect of material properties on the momentum balance equation.

Case 1: Steady waves in medium density snow.

In the following the constitutive equation based on the pore collapse (eq II.B.47) is used. Later steady waves in low density snow is considered. First, however, Eq II.B.47 has to be modified to include the intergranular inertial term as defined by eq. II.B.44. Eq II.B.47 is valid for quazi-static deformations in which inertial effects are negligible.

The complete constitutive law is

$$p = \frac{1}{3\alpha} \ln\left(\frac{\alpha}{\alpha-1}\right) \left(2(S_0 - C) + c \ln \left(\frac{-\dot{\alpha} A)^2}{\alpha(\alpha-1)}\right)\right) Je^{(-\phi\alpha/\alpha_0}$$

$$+ \frac{\tau^2}{\alpha} \frac{dQ}{d\alpha} (\alpha, \dot{\alpha}, \ddot{\alpha}) \qquad \text{(IV.C.3)}$$

where

$$Q = -\frac{3}{2} \ddot{\alpha} \left((\alpha-1)^{2/3} - \alpha^{-2/3}\right) \qquad \text{(IV.C.4)}$$

$$- \frac{1}{2} \dot{\alpha}^2 \left((\alpha-1)^{-1/3} - \alpha^{-1/3}\right)$$

$$\tau^2 = \rho_m a^2 / 3(\alpha_0 - 1)^{2/3} \qquad \text{(IV.C.5)}$$

The inertial term given in eq 3 is essentially the acceleration potential term $\rho_m (\psi_b - \psi_a)$ defined in eq II.B.44, except that a and b have been eliminated and the equation has been algebraicly reorganized. Some simplification of the acceleration term can be made. Except under extremely severe shocks, the term containing $\ddot{\alpha}$ can be neglected. Later in the paper this will be done.

In a steady wave, the solution to the balance equations may be expressed in terms of the single variable

$$\eta = X - Vt. \tag{IV.C.6}$$

Substituting the constitutive law into eq IV.B.20 and changing variables from X and t to η by use of eq 6 we find after some algebra

$$-\frac{\beta_0 V^2}{\alpha_0}(\alpha-\alpha_0) = \frac{J}{3\alpha}^{-\phi\alpha/\alpha_0} \ln\left(\frac{\alpha}{\alpha-1}\right) \left(2(S_0-C)+C \ln\left(\frac{(V\alpha')^2}{\alpha(\alpha-1)}\right)\right) - \frac{V^2\tau^2}{2\alpha}\frac{d}{d\alpha}(Q(\ddot{\alpha},\dot{\alpha},\alpha)) \tag{IV.C.7}$$

The prime denotes differentiation with respect to the variable η. After integrating the above, we get

$$-\frac{\rho_0 V^2}{3\alpha_0}(\alpha-\alpha_0)\left(\alpha^2 - \frac{\alpha_0}{2}(\alpha+\alpha_0)\right) = -\frac{V^2\tau^2}{2}\left(Q(\ddot{\alpha},\dot{\alpha},\alpha)\right) + \int_{\alpha_0}^{\alpha} \frac{J}{3} \ln\left(\frac{\alpha}{\alpha-1}\right) \left(2(S_0-C)+C \ln\frac{(A\dot{\alpha})^2}{\alpha(\alpha-1)}\right) e^{-\phi\alpha/\alpha_0} d\alpha \tag{IV.C.8}$$

The above equation describes the density ratio jump across the wave, once the wave speed is known. However, this is an integro-differential equation and would have to be solved by a numerical method or some other approximate method.

In cases where strain rates are not extremely large, eq 8 would have to be used, since it makes use of the more complete constitutive equation,

eq 3. Such would be the case for low-frequency, large-amplitude waves.

However, if one is considering shockwaves, the strain rates become very large, say on the order of 10^4 -$10^6 s^{-1}$. Under these extremely high rates, the constitutive equation can be simplified somewhat, since the yield stress of ice becomes only weakly rate dependent. This can be seen in eq. II.A.3 where at large values of D, Y changes only slightly with significant changes in D. Consequently, if Y is replaced by a constant value Y_o = 300 bar, the constitutive equation developed in section II.A can be reduced to the following form

$$p = \frac{2Y_0 J}{3\alpha} \ln\left(\frac{\alpha}{\alpha-1}\right) e^{-\phi\alpha/\alpha} - \frac{\tau^2}{2} \frac{d}{d\alpha} Q(\alpha,\dot{\alpha},\ddot{\alpha}) \qquad \text{(IV.C.9)}$$

This equation is obviously more tractable than the earlier equation. The value of Y_o = 300 bar was chosen since this yield stress is consistent with strains actually generated in many shockwaves ($D \tilde{\sim} 2x10^5 s^{-1}$), and a range of D between $10^4 s^{-1}$ and $10^6 s^{-1}$ places the actual yield stress Y within ten percent of the value of Y_o = 300 bar.

Substituting eq. 9 into eq IV.B.20, we obtain

$$-\frac{\rho_0 V^2(\alpha-\alpha_0)}{\alpha_0} = \frac{2Y_o}{3\alpha} J \ln\left(\frac{\alpha}{\alpha-1}\right) e^{-\phi\alpha/\alpha_0}$$

$$-\frac{V^2\tau^2}{2\alpha} \frac{d}{d\alpha}\left(Q(\ddot{\alpha},\dot{\alpha},\alpha)\right) \qquad \text{(IV.C.10)}$$

or, upon integrating,

$$-\frac{\rho_0 V^2(\alpha-\alpha_0)}{3\alpha_0}\left(\alpha^2 - \frac{\alpha_0}{2}(\alpha+\alpha_0)\right)$$

$$= -\frac{V^2\tau^2}{2}\left[Q(\ddot{\alpha},\dot{\alpha},\alpha)\right]$$

$$+\int_{\alpha_o}^{\alpha} \frac{2}{3}\frac{JY_o}{} \ln\left(\frac{\alpha}{\alpha-1}\right) e^{-\phi\alpha/\alpha_0}\, d\alpha \qquad \text{(IV.C.11)}$$

In steady waves, $\dot{\alpha} = 0$, and $\ddot{\alpha} = 0$ both ahead of and behind the wave; therefore $[Q(\ddot{\alpha},\dot{\alpha},\alpha)]$ vanishes. Substituting eq. IV.B.18 into eq. 11 for steady waves then gives

$$p^* = \left(2\gamma Y_0 \int_{\alpha_o}^{\alpha} \ln\left(\frac{\alpha}{\alpha-1}\right) e^{-\phi\,\alpha/\alpha_0}\, d\alpha\right)$$

$$\left(\alpha^{*2} - \frac{\alpha}{2}(\alpha^*+\alpha_0)\right)^{-1} \qquad \text{(IV.C.12)}$$

Carrying out the indicated integration results in

$$p^* = \left(\alpha^{*2} - \frac{\alpha_0}{2}(\alpha^*+\alpha_0)\right)^{-1}$$

$$\left(g_1(\alpha^*) - e^{-\phi\,\alpha^*/\alpha_0}\, g_1(\alpha^*-1)\right) \qquad \text{(IV.C.13)}$$

where

$$g_1(\alpha^*) = -\frac{\alpha_0}{\phi}\left(\ln(\alpha^*)e^{-\phi\alpha^*/\alpha_0} - \ln(\alpha_0)e^{-\phi}\right) + \frac{\alpha_0}{\phi}$$

$$\left(\ln\frac{\alpha}{\alpha_0} + \sum_{i=i}^{\infty} \frac{(-\phi)^n}{n\cdot n!}\left(\frac{\alpha^*}{\alpha_0}\right)^n - 1\right) \qquad \text{(IV.C.14)}$$

Equations 13 and 14 give the pressure jump across the wave. Equation 10 can then be used to calculate the wave profile, i.e., the variation of the density ratio α inside the stress wave. This can be accomplished by inverting eq. 10 to obtain

$$\eta = \int_{\alpha_o}^{\alpha} \frac{d\beta}{F(\beta,\ \alpha_0,\ V)} \qquad \text{(IV.C.15)}$$

where η is the variable defined in eq 6, and

$$F(\beta,\alpha_0,\ V) = \frac{1}{\tau V}\left(\frac{4\ Y_0}{3f(\beta)} \int_0^{\beta'} \ln\left(\frac{\beta'}{\beta-1}\right) e^{-\phi\beta'/\alpha_0}\, d\beta'\right.$$

$$+ \frac{2\rho_0 v^2}{3\ {}_0f(\beta)}(\beta-\alpha_0)\left(\beta^2 - \frac{\alpha_0}{2}(\beta+\alpha_0)\right)\Bigg)^{1/2} \qquad \text{(IV.C.16)}$$

Setting $\alpha = \alpha^*$ in eq 15 then gives η_1, the length of the wave, but this equation can also be used to calculate the α-η profile during the passing of the wave.

Napadensky (1964) conducted an extensive testing program on shock waves in snow at Camp Century. These experiments involved snow with densities generally higher than 400 kg m^{-3}. The stress waves were generated by using a low-density explosive to drive a metal plate into solid cylindrical specimens. By varying the amount of explosive and the mass of the driver plate, a wide range of load conditions was achieved. The explosive technique, however, usually has a considerable amount of experimental scatter.

A streak camera was used to record the motion of etch marks on the snow specimen and the driver plate. In this way, both particle velocity v and wave velocity V were recorded photographically. Since the speed of the camera was such that the exposure time was only about 5 μs, fairly good time resolution was achieved. However, as indicated by Mellor (1977), large errors were incurred in the experimental program. There was a very poor resolution at the lower pressure levels, and it is questionable whether or not Napadensky's reduced data accurately reflected the actual stress wave parameters. However, for the intermediate range of stress wave pressures, the data appeared reasonable, since the streak film recordings appeared to have both good time resolution and ability to record particle displacement.

Figures 33 and 34 give a direct comparison of the theory and Napadensky's experimental results, and as can be seen the two compare fairly well.

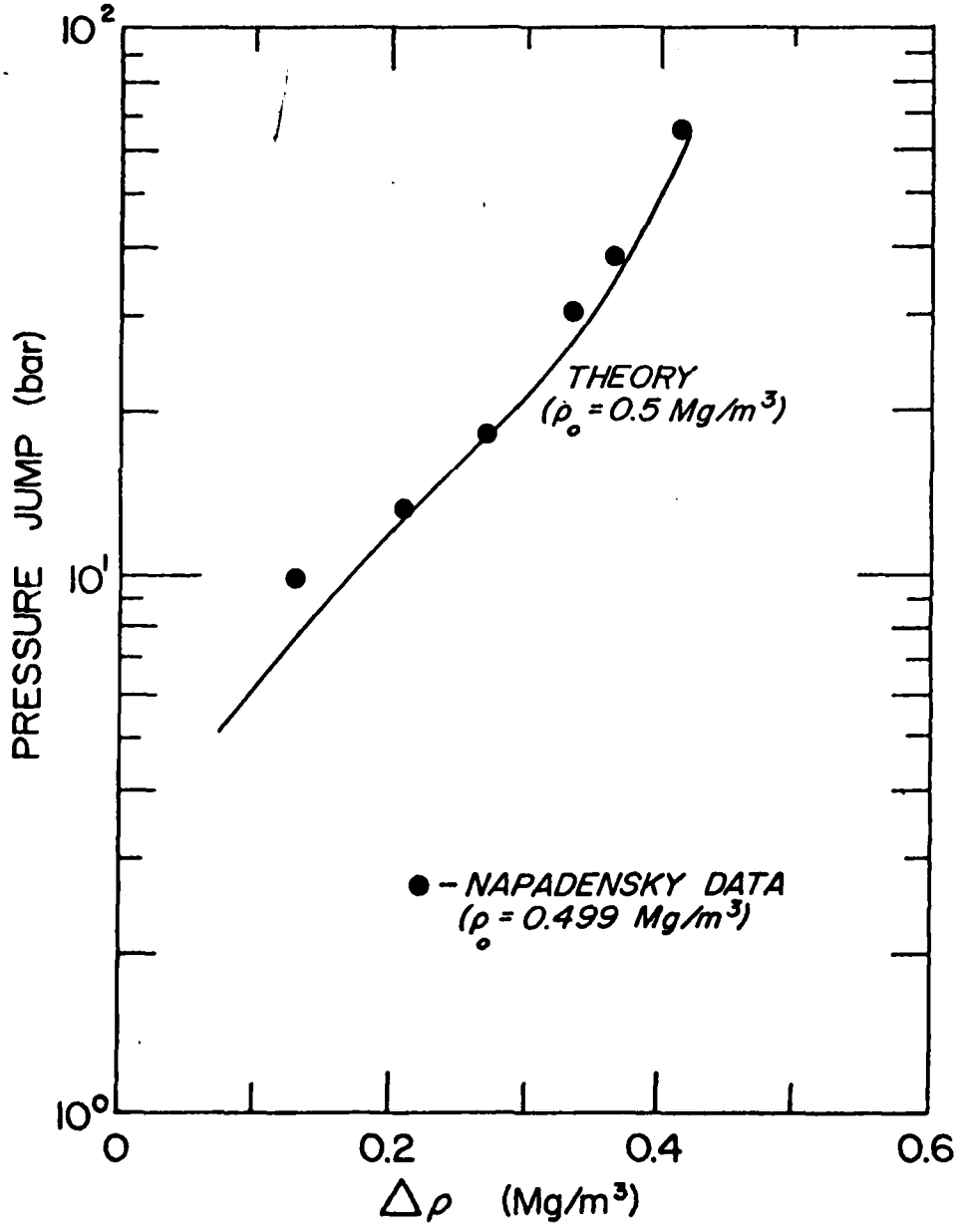

Figure 33. Comparison of theory with stress wave data.

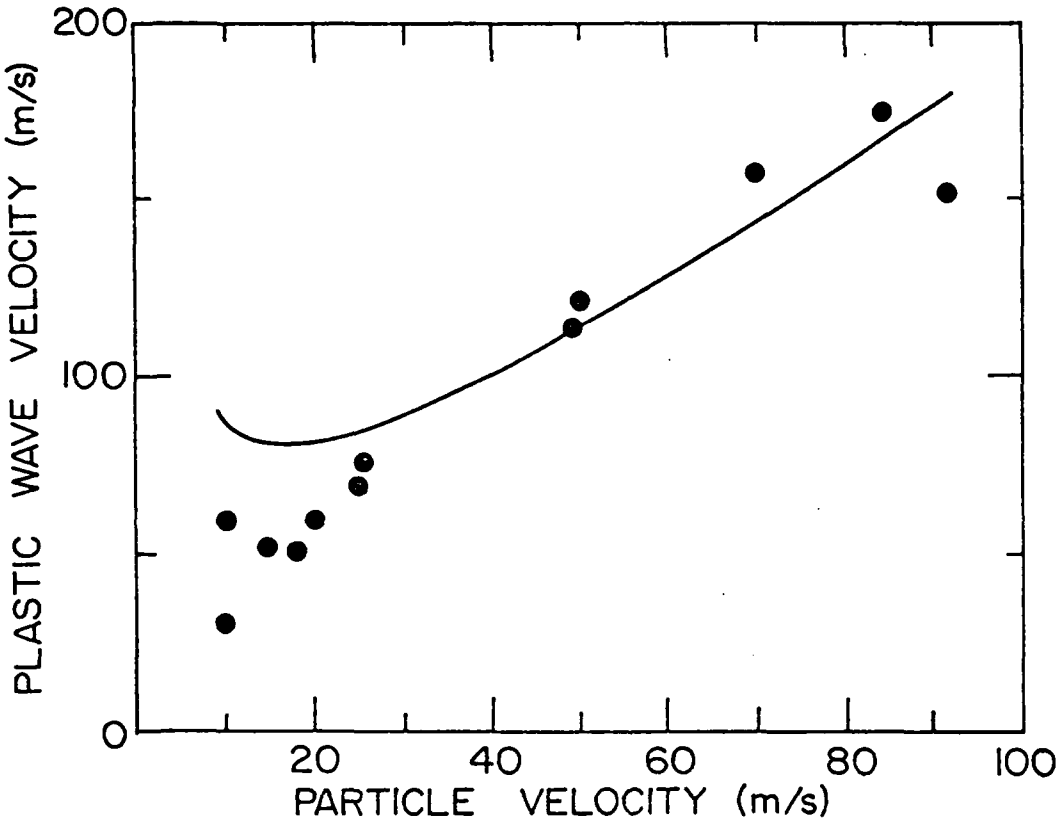

Figure 34. Theoretical and experimentally measured values of stress wave velocity.

Figure 33 shows the pressure jump across the wave as a function of the density jump $\Delta\rho$ caused by the wave. Figure 34 shows the variation of plastic wave velocity V with particle velocity v^*. For particle velocities above 20 m s^{-1}, the data and theory compare nicely, but below that, they deviate significantly. The theoretical curve terminates at the point where the wave ceases to be fully plastic.

The data in figure 34 at the lower particle velocities are questionable. Napadensky shows the plastic wave velocity decreasing to zero as the wave intensity (as indicated by v^*) the particle velocity decreases and this result defies physical reasoning. For instance, as the intensity of a shock wave decreases, the severity of the plastic deformation should also decrease. As the amount of the plastic deformation becomes less significant, the pressure wave should then begin to acquire characteristics of an elastic wave. Equation IV.B.20 can be used to find the wave speed:

$$V^2 = \frac{\alpha_o}{\rho_o} \frac{\Delta p^*}{\Delta \alpha^*} \qquad \text{(IV.C.17)}$$

If $\Delta p^*/\Delta\alpha^*$ does not approach zero as the stress wave intensity decreases, V^2 must remain finite at low plastic strains. One would expect $\Delta p^*/\Delta\alpha^*$ to acquire a value close to the elastic modulus. This argument is also supported by other analytical work, such as that of Coleman et al. (1964), on the theory of wave propagation in nonlinear materials. In particular, we note the familiar equation

$$V^2 = E_p/\rho_0 \qquad \text{(IV.C.18)}$$

where for shock waves E_p is the instantaneous secant modulus, and for acceleration waves E_p is the instantaneous tangent modulus. In either

stress wave, E_p increases as the degree of plastic deformation decreases, i.e., as a smaller percentage of the material is deformed plastically. As a result, E_p appraoches E, Young's modulus of the material, and V thereby increases to a value close to the elastic wave speed for weak plastic waves.

In the case of strong stress waves that produce complete plastic deformation of the matrix material and large jumps in density, the work-hardening characteristics of the material become important in determining the resulting wave speed. In particular, E_p increases as a result of densification and work-hardening effects, thereby resulting in larger balues of V as indicated by eq 18. Consequently, a very strong plastic wave has a large wave speed. The above reasoning justifies the minimum calculated value of V shown by the curve in Figure 34. This minimum is located near the transition zone between partially plastic and fully plastic waves.

Figure 35 - 37 present results of parametric studies of stress waves in snow. Figure 35 shows how the density ratio varies through the front of the stress wave. For the less intensive wave, a shorter wavelength is required to generate the acceleration forces necessary to produce the compaction to decrease α from 3.0 to 2.0.

Figure 36 illustrates the variation of pressure jump [p] with density jump for a range of initial densities. Note that as the initial density is increased, the curves are translated upward. Figure 37 also gives a very dramatic demonstration of the effects of work-hardening characteristics of snow. At low pressures, the plastic wave speeds are as expected; i.e., wave speed increases with density. But at higher pressures, this relationship is inverted, since large changes in α must accompany the large pressure

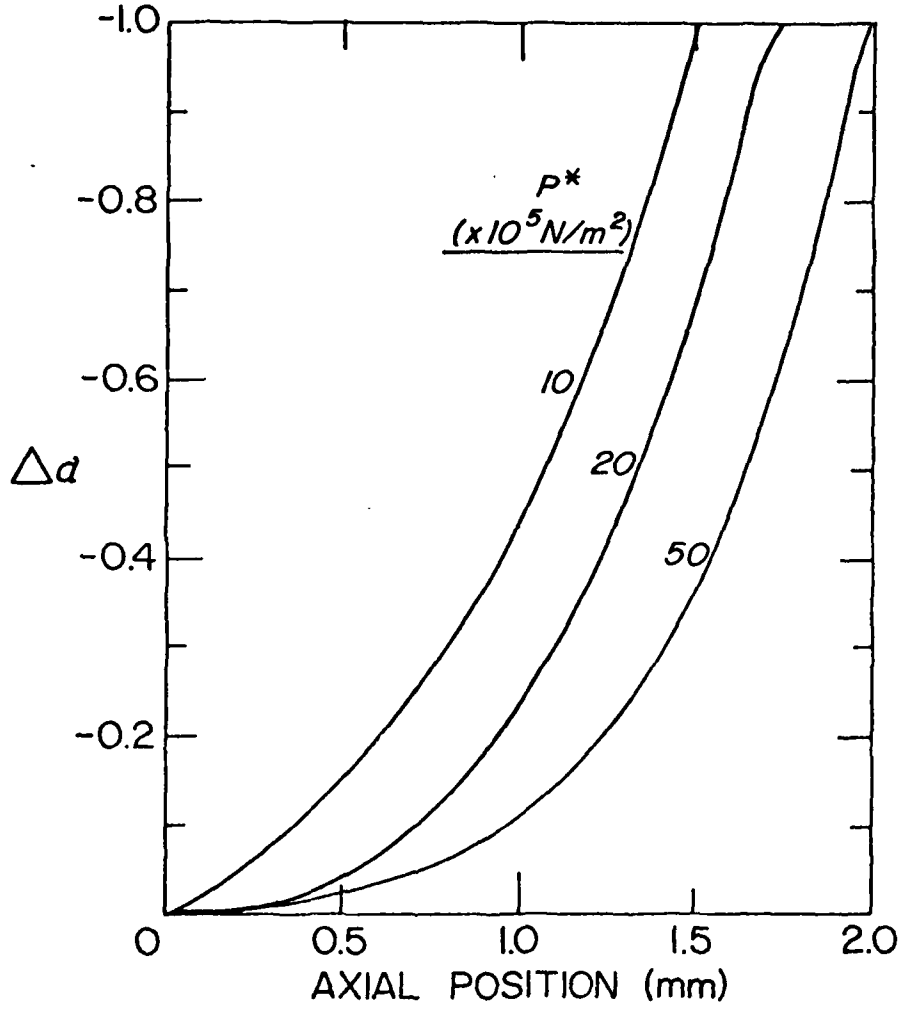

Figure 35. Wave profiles.

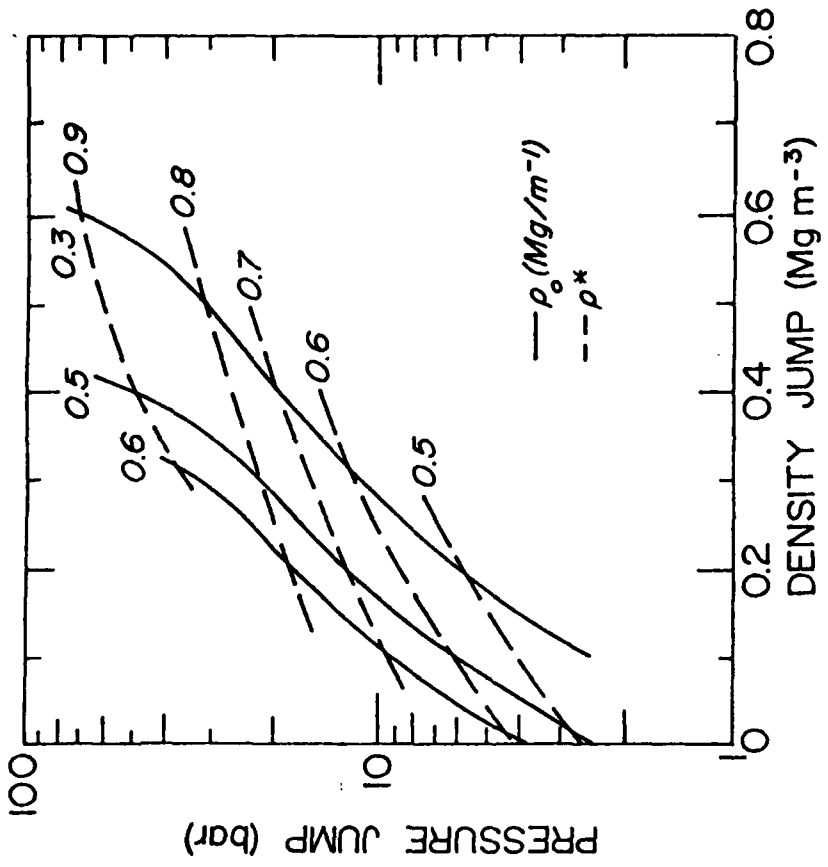

Figure 36. Variation of pressure jump with density jump and initial density.

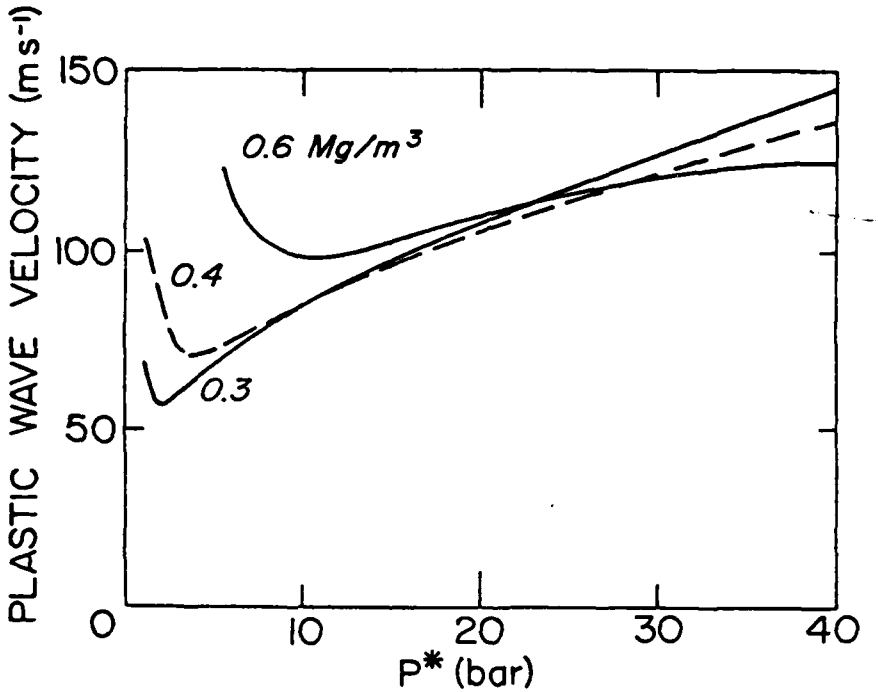

Figure 37. Variation of plastic wave velocity with pressure jump for steady waves.

jumps for snow with initial low densities. Consequently, there is considerable work-hardening, which has a stiffening effect, and this results in increased wave speeds. Snow with high initial densities would not undergo as much work-hardening.

Case 2: Steady waves in low density snow.

For this case, the neck growth model constitutive equation is used, since densities as low as 100 Kg m^{-3} may be studied. Other than the constitutive law, the analysis is identical to that presented in Case 1. Consequently only the results and discussion is presented here. The final expression for the pressure jump is

$$p^* = 3\left(\alpha^{*2} - \frac{\alpha_0}{2}(\alpha^* - \alpha_0)\right)^{-1} \int_{\alpha_o}^{\alpha^*} \frac{\ln(\dot{\alpha}/A_1)}{\beta_1 F}\, d\alpha \qquad \text{(IV.C.19)}$$

Figures 38-40 illustrate the results of this study. Unfortunately only a small amount of experimental data is available for a comparison with these results. To date the most comprehensive experimental study is that of Napadensky (1964). However, Napadensky's experiments were conducted with snow with desnities of 0.5 Mg m^{-3} or higher, so a direct comparison with the calculated results here is not possible for low-density snow.

Figure 38 illustrates the variation of pressure jump with density for several different initial densities, including 0.5 Mg m^{-3}, which is compared with Napadensky's data. As can be seen, the results agree with the data for that initial density. In Figures 38 and 39, the dominant frequency of the wave was 200 kHz. This frequency would correspond to what is produced by high-speed explosives.

Figure 39 shows the manner in which the wave speed varies with the wave intensity as determined by the pressure jump. In particular, for each initial density the wave speed has a local minimum at low values of

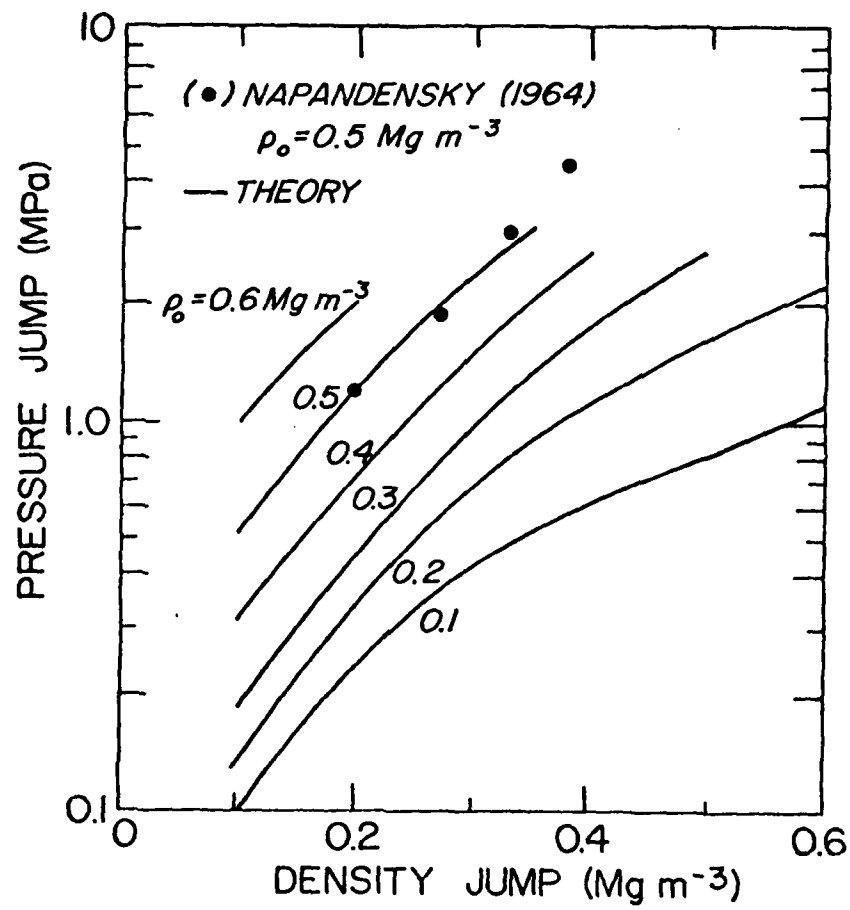

Figure 38. Dependence of pressure jump on density jump for stress waves in snow represented by neck growth model.

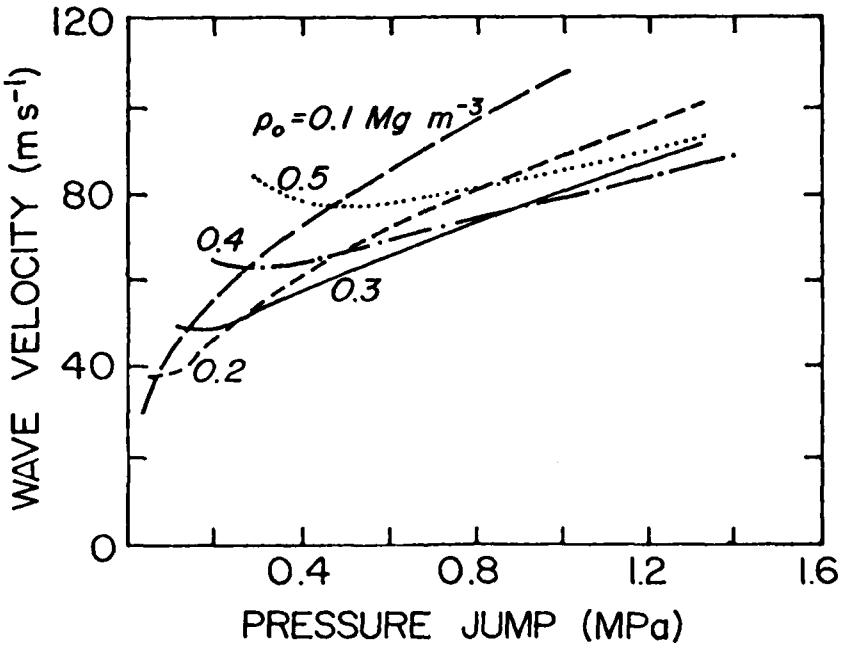

Figure 39. Variation of stress wave velocity with pressure jump.

wave pressure. This is attributable to the work-hardening properties of snow under volumetric deformations. As the snow is compacted, the necks rapidly thicken, which in part enhances the material strength. In addition, the large deformations which occurs in these necks also work-harden the neck material, thereby further increasing the snow strength. This resulting increase in material strength results in an increased wave speed since the wave speed is determined by the ratio of $p^*/(\alpha^* - \alpha_0)$.

Figure 40 illustrates the effect of wave frequency on the pressure jump for pressure waves which produce a density jump of 0.2 Mg m^{-3}. Curves are presented for initial densities of 0.1, 0.2, and 0.3 Mg m^{-3}. As can be seen, the pressure jump increases with wave frequency, although the dependence of pressure jump on frequency is not as significant as the dependence on density.

The stress-wave analysis reported here has been shown to agree well with the only experimental data the author is aware of. Unfortunately the data are available only for snow with an initial density of about 0.5 Mg m^{-3}. Consequently, no definite conclusions can be made about the validity of the theoretical results for snow with initial densities below 0.5 Mg m^{-3}. However, the volumetric equation upon which this study is based has been shown to represent accurately the response of snow under quasi-static load conditions for densities as low as 0.1 Mg m^{-3}. Consequently, the low-density stress-wave results shown here should at least be qualitatively correct.

The wave speed was found to be strongly dependent on initial density and the pressure jump across th wave front. Since the pressure is only moderately affected by frequency, the wave speed is also only moderately

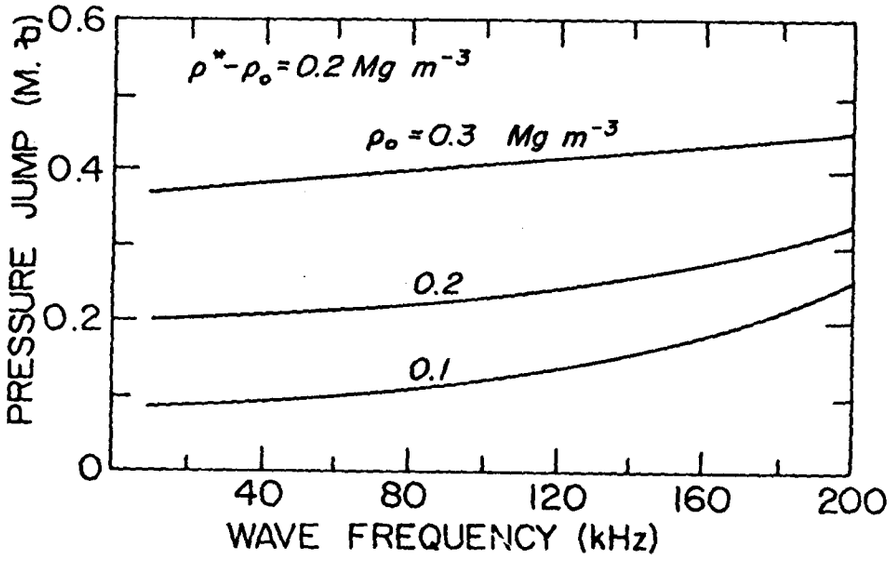

Figure 40. Effect of stress wave frequency on pressure jump for constant density jump.

frequency dependent.

The dependence of wave speed and pressure jump on density is not as straight-forward as it is for pressure waves which produce infinitesimal strains. In the case of pressure waves that produce large density changes, pressure jump and wave speed depend on both the initial density ρ_o and the final density ρ^*. The complicatated relationship can readily be observed in Figure 39.

The type of pressure wave described in this case is not commonly found in nature. However, it does play a central role in determining the effectiveness of explosives in initiating avalanches, since a good portion of the explosive energy that is transmitted to the snowpack is absorbed in the crater zone through inelastic compaction of the snow. This type of deformation also is largely responsible for the attenuation of the pressure wave as it propagates away from the crater formed by the explosive. All of this decreases the energy that is delivered to the snowpack for the purpose of starting avalanches.

The result that the wave pressure-jump increases with wave frequency would imply that the energy absorbed irreversibly by the snow also increases with frequency assuming that ρ_o and ρ^* are held constant. This in turn would imply that the attenuation rate would increase with frequency, since larger amounts of energy are dissipated in the snow as frequency increases. However, since this is weakly frequency dependent, the effect of frequency on attenuation rate is probably not as important as ρ^* and ρ_o for plastic waves.

IV.D NONSTEADY SHOCKWAVES

If the wave is nonsteady, the wave front profile, amplitude and wave speed may all change with time. Material nonlinearity and internal dissipation mechanisms are accountable for this. In some cases, the wave amplitude may actually grow, although such a situation is generally short-lived. Coleman et al. (1964) have studied the properties of nonlinear waves in some detail. Since that time considerable effort has been devoted to the study of stress waves in nonlinear or inelastic materials. More recently, Nunziato and Walsh (1978) have investigated the propagation of waves in uniformly distributed granular materials. In their paper they indicated that, in a granular material, the only density change induced by a shock wave must come from compaction of the matrix material and not from reduction of void volume. This result contradicts the results of this study (IV.B.19) and the experimental results of Napadensky (1964).

We have developed now the wave equation for a material with a volumetric constitutive equation of the form given by eq IV.C.3.

Differentiating eq IV.B.9 with respect to time, and then substituting the equation of motion eq IV.B.7, yield

$$\frac{1}{\rho_0} \frac{\partial}{\partial X}\left(\frac{-\partial p}{\partial X}\right) = \frac{1}{\alpha_0} \alpha_0 \frac{\partial^2 \alpha}{\partial t^2} \qquad \text{(IV.D.1)}$$

Then, substituting eq IV.C.3 directly in the above equation, we get, after some rearranging,

$$E_T \frac{\partial^2 \alpha}{\partial X^2} + \frac{\partial E_T}{\partial X} \frac{\partial \alpha}{\partial X} = \frac{\rho_0}{\alpha_0} \frac{\partial^2 \alpha}{\partial t^2}$$

$$+ \frac{\partial}{\partial X}\left(E_1 \frac{\partial \dot{\alpha}}{\partial X} + E_2 \frac{\partial \ddot{\alpha}}{\partial X}\right) \qquad \text{(IV.D.2)}$$

In order to solve this equation, a finite difference solution can be used. This equation is extremely nonlinear, since E_T, E_1, and E_2 are all functions of α, $\dot{\alpha}$, and $\ddot{\alpha}$. Therefore, convergence and stability problems are difficult

to handle. A central differencing technique is used. At position X_i and time t_j let α have the value α_i^j. Then the difference forms of the time and spacial derivatives of α become

$$\dot{\alpha}_i^j = \frac{\alpha_i^{j+1} - \alpha_i^{j-1}}{2\Delta t} \qquad \text{(IV.D.3)}$$

$$\ddot{\alpha}_i^j = \frac{\alpha_i^{j+1} - 2\alpha_i^j + \alpha_i^{j-1}}{(\Delta t)^2} \qquad \text{(IV.D.4)}$$

$$\frac{\partial \alpha_i^j}{\partial X} = \frac{\alpha_{i+1}^j - \alpha_{i-1}^j}{2\Delta X} \qquad \text{(IV.D.5)}$$

$$\frac{\partial^2 \alpha_i^j}{\partial X^2} = \frac{\alpha_{i+1}^{j+1} + \alpha_{i+1}^{j-1} - 2\left(\alpha_i^{j-1} + \alpha_i^{j-1}\right) + \alpha_{i-1}^{j+1} + \alpha_{i-1}^{j-1}}{2(\Delta x)^2} \qquad \text{(IV.D.6)}$$

The form shown in eq 6 is used for the second order derivative, since this averaged derivative results in improved stability characteristics of the finite difference solution, as indicated by Ames (1965).

In solving the problem, a double modulus was employed. During pressure buildup, IV.B.1 gives the appropriate tangent modulus, which becomes

$$E_T = \frac{2Y_0 e^{-\phi\alpha/\alpha_0} f_1(\alpha)}{3\alpha^2} - \tau^2 Y_0 \left(-f_2(\alpha)\ddot{\alpha} - -f_3(\alpha)\dot{\alpha}^2\right) \qquad \text{(IV.D.7)}$$

where

$$f_1 = \frac{1}{(\alpha-1)} + \left(1+\phi\frac{\alpha}{\alpha_0}\right) \ln\left(\frac{\alpha}{\alpha-1}\right) \qquad \text{(IV.D.8)}$$

$$f_2 = \frac{g(\alpha)}{3\alpha} + \frac{f(\alpha)}{\alpha^2} \qquad \text{(IV.D.9)}$$

$$f_3 = \frac{2}{9\alpha} \frac{1}{(\alpha-1)^{7/3}} - \frac{1}{\alpha^{7/3}} + \frac{g(\alpha)}{6\alpha^2} \qquad \text{(IV.D.10)}$$

$$g = (\alpha-1)^{-4/3} - \alpha^{-4/3} \qquad \text{(IV.D.11)}$$

$$f = (\alpha-1)^{-1/3} - \alpha^{-1/3} \qquad \text{(IV.D.12)}$$

However, once a maximum pressure is reached, and unloading begins, the static part of E_T must decrease in order to avoid a large elastic rebound in the finite difference solution. This rebound produces an artificial oscillation in the solution and is a common problem with finite difference methods. Various methods have been used to reduce this form of instability. The easiest way to facilitate this is to decrease f_1 by a factor of 1/2 when $\dot{\alpha}$ becomes negative. A factor of 1/2 is somewhat arbitrary, but this value was found to be sufficient to avoid any significant volumetric rebound.

In order to demonstrate the solution, we consider the particular problem of an air blast directly over a snow covered ground surface. We assume the blast produces an overburden pressure of the form

$$p = \frac{1}{2} p^* \ (1-\cos Wt), \ 0 < Wt < 2\pi$$

$$p = 0 \quad Wt > 2\pi \qquad \text{(IV.D.13)}$$

and calculate the attenuation of the wave as it propagates into the snowpack. The frequency $\omega = W/2\pi$ is determined by the speed of the explosion, and the overburden pressure p^* is determined by explosive size and proximity to the snowpack surface. Of particular interest is the response of a snowpack to an overburden pressure of about 20 bar since this is what the SULFAE (surface-launched unit fuel air explosive) weapon system generates.

Figures 41-46 show results of the finite difference solution of the nonsteady wave problem just described. Figures 41 and 42 illustrate how

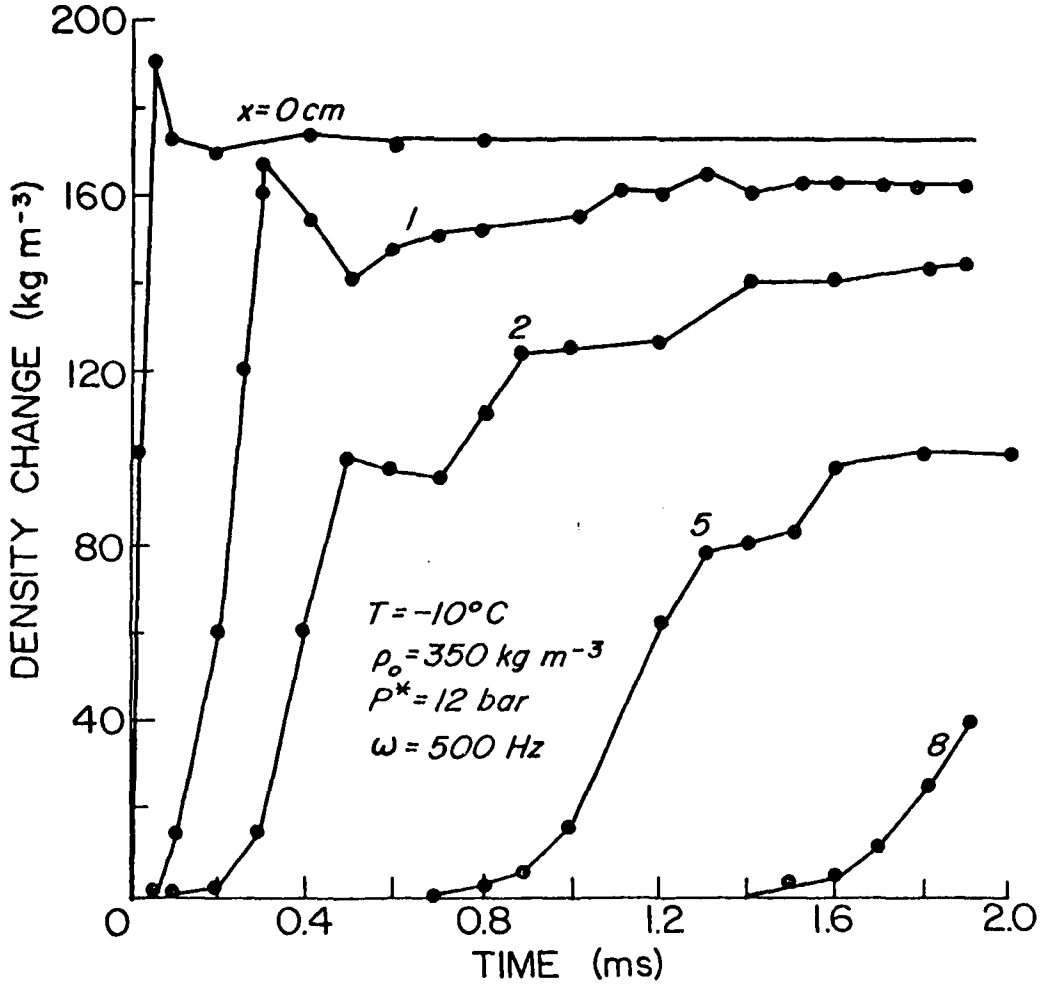

Figure 41. Temporal variation of snow density due to shockwave loading.

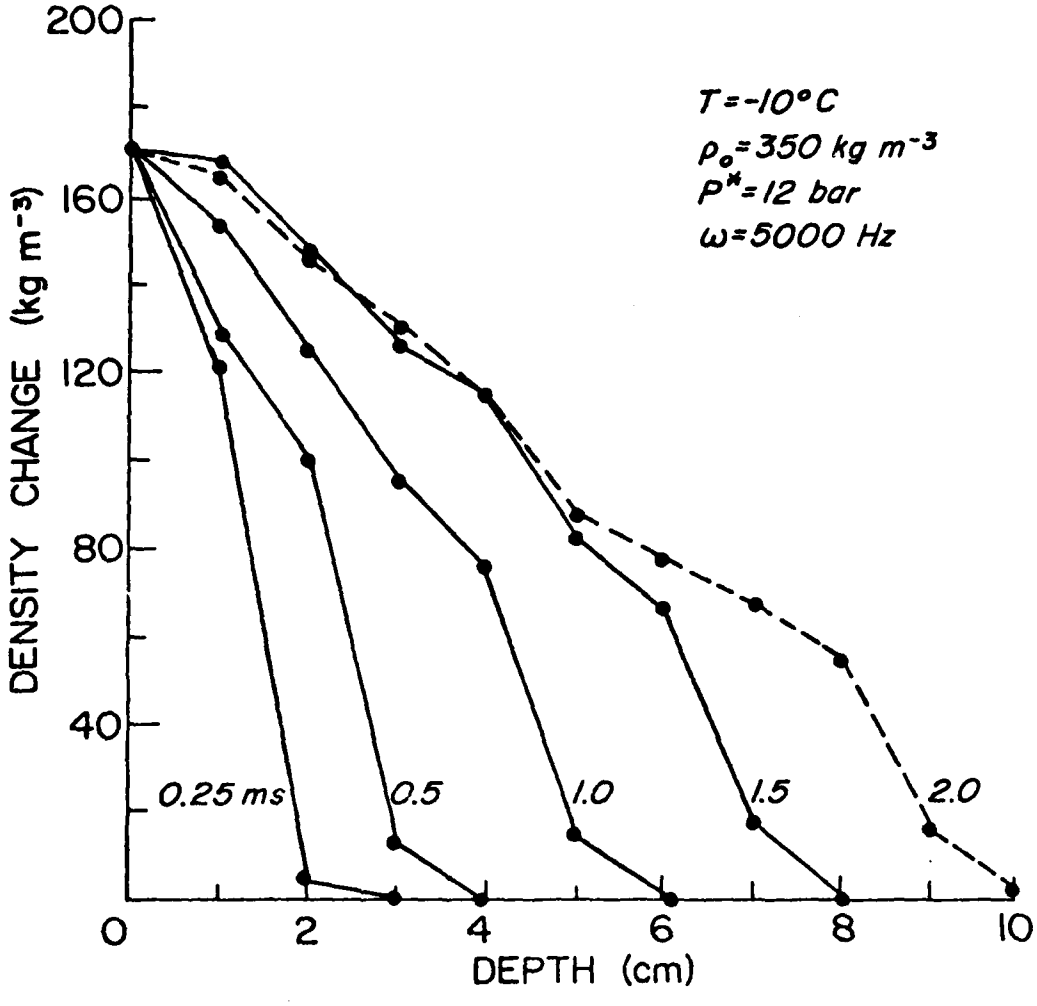

Figure 42. Spatial variation of density in sowpack at various times after initial loading.

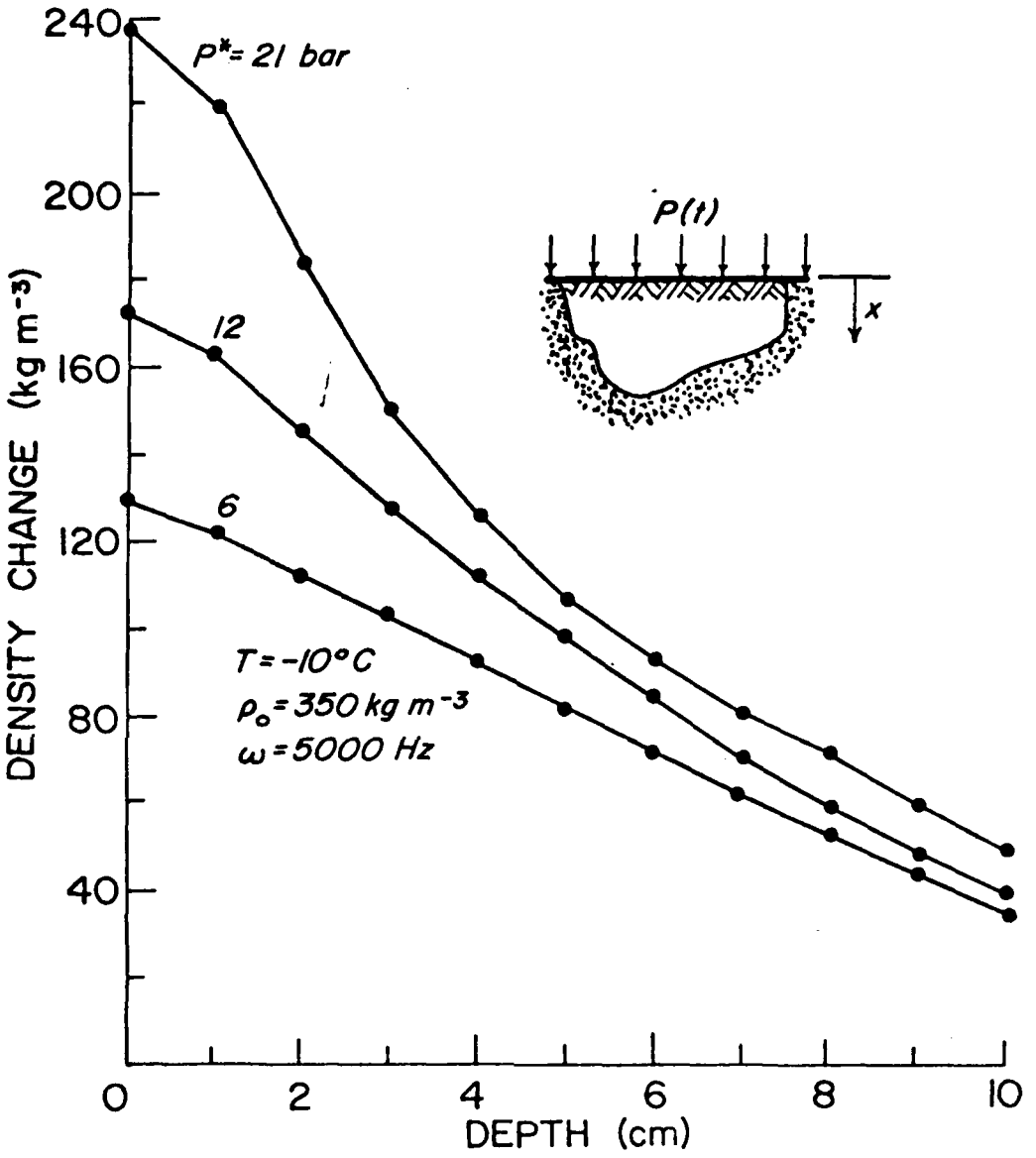

Figure 43. Attenuation of density jump caused by shockwave.

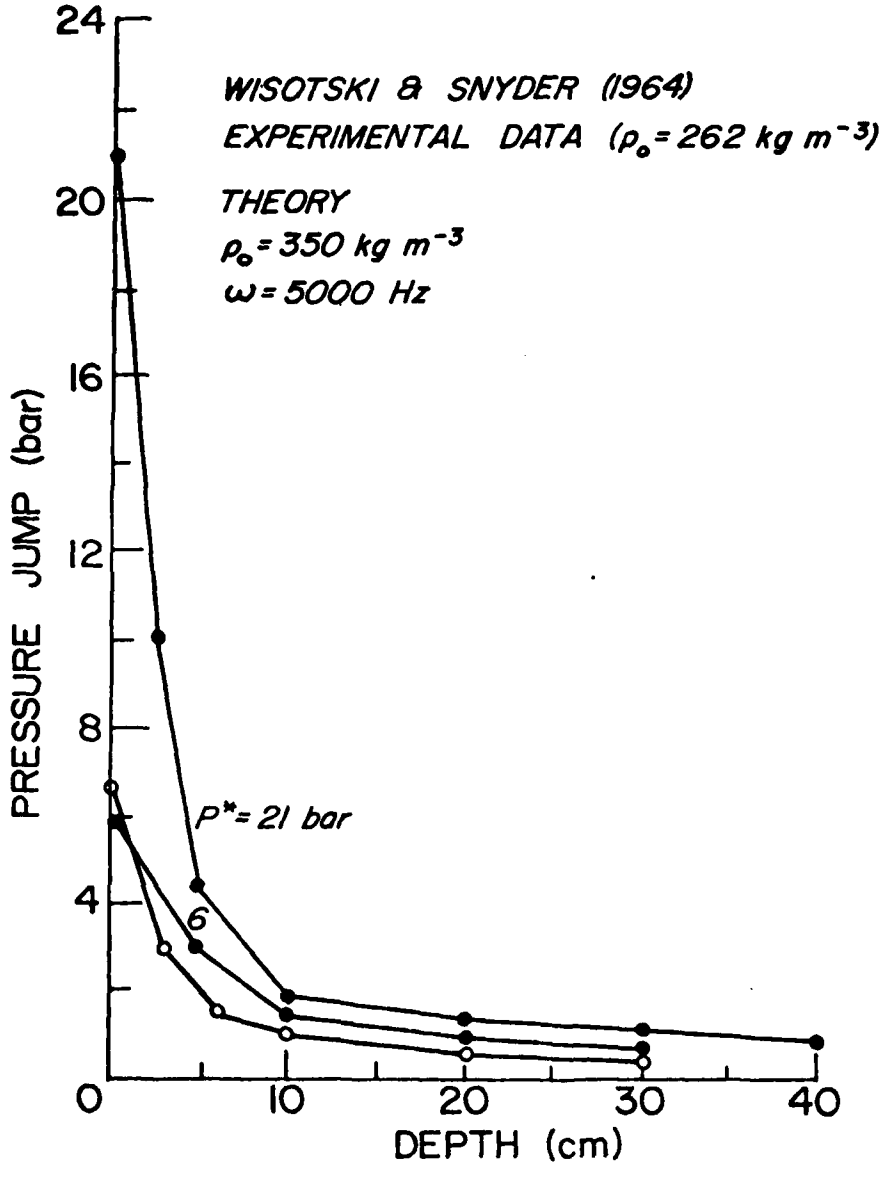

Figure 44. Attenuation of shockwaves in medium density snow.

the wave form is altered as it propagates into snow with an initial density of 350 kg m^{-3}. The surface loading has a frequency of ω = 5000 Hz and an amplitude of p^* = 12 bar. Figure 41 shows the temporal variation of the density change for points at 0, 1, 2, 5, and 8 cm into the snowpack. Figure 42 demonstrates the density profile for various times. Note how the wave spreads and the density rates $\dot{\rho}$ decreases as the wave propagates further into the snowpack.

Figures 43 and 44 make a direct comparison of three different pressures. Figure 43 compares wave attentuation in terms of density jump and Figure 44 shows the pressure attentuation. As can readily be seen, the advantage of the higher pressures is largely eliminated within the first 10 cm. This merely points out the substantial energy absorbing capability of snow.

As expected, the highly dissipative characteristics of snow rapidly change the stress wave as it propagates through snow. For pressure waves with a magnitude in excess of 5 bar, the pressure amplitude reduced to a small fraction within 10 cm. This result is to some extend verified by Wisotski and Snyder (1966). In the tests reported by Wisotski and Snyder, one-pound spherical Penolite charges were detonated in deep mid-season snowpack. Piezoelectric gages were used to record arrival times and pressures to within 0.15 m of the charge. These transducers apparently had a broad, flat frequency range, so that the recorded results should be meaningful. They also observed that the wave speed close to the charge was significantly slower than further from the charge. However, there was a great deal of scatter in measurement of arrival times, so no precise measurements were made. But the pressure readings for a 6-bar pressure wave showed good agreement with the results shown in Figure 44.

Figure 45 shows the variation of the stress wave speed as the wave propagates into the snow. Initially the 21-bar wave travels at a signi-

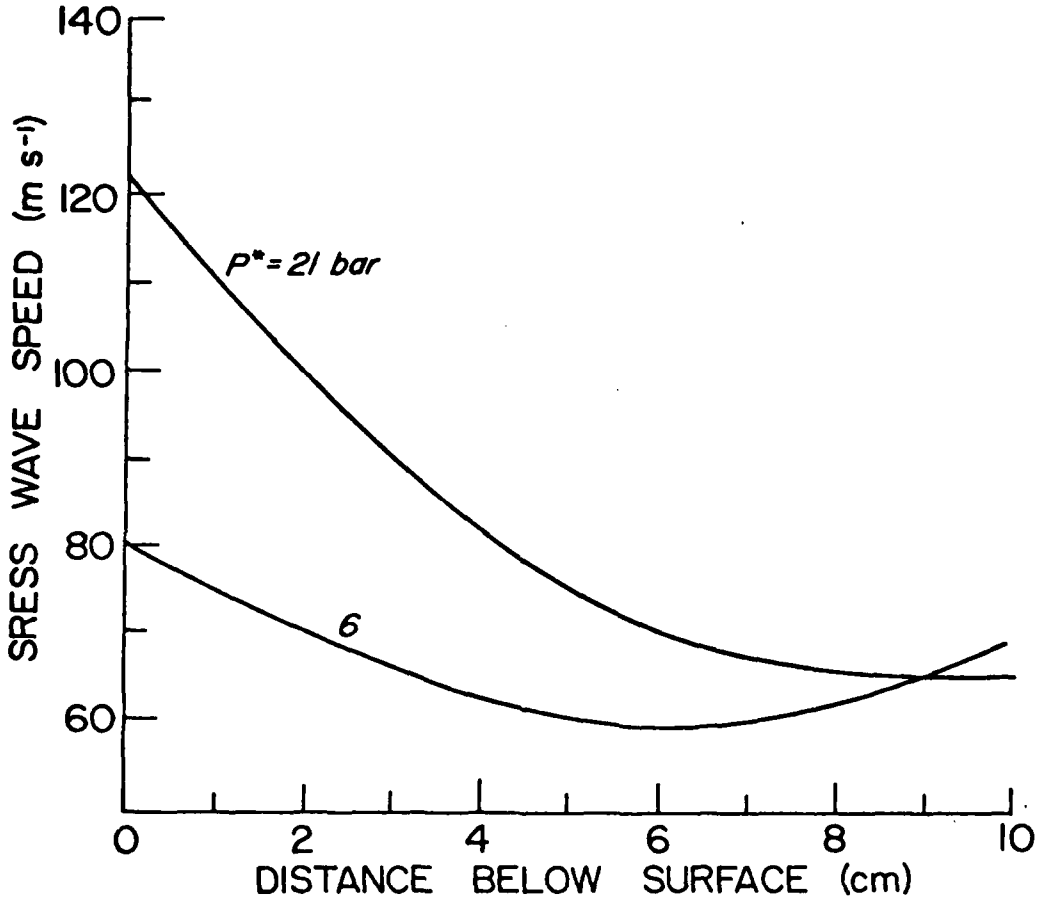

Figure 45. Variation of wave speed with density.

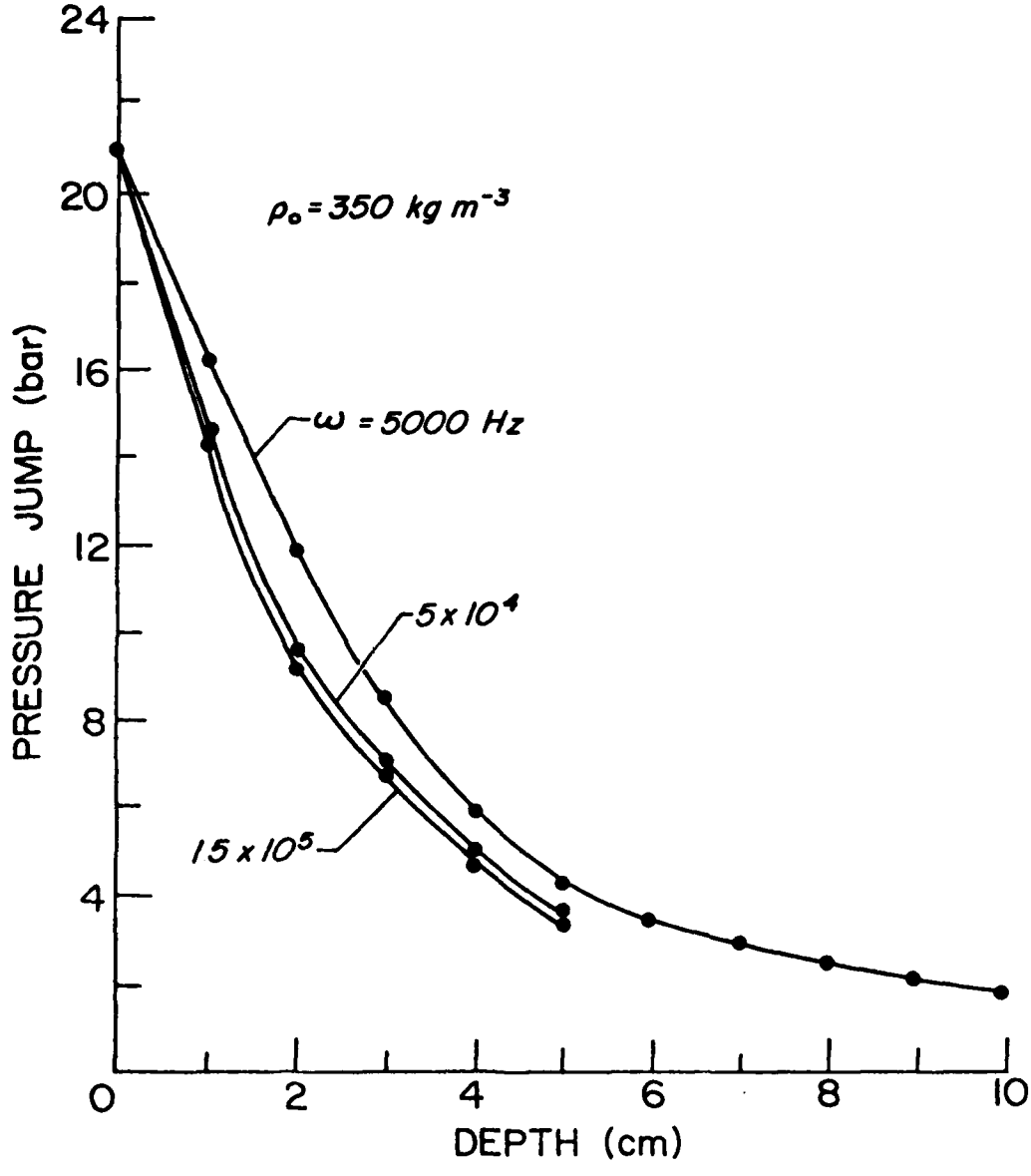

Figure 46. Effect of wave frequency on attenuation.

ficantly higher speed, but this situation quickly changes. The variation in stress wave speed is due to a combination of factors. The wave speed initially decrease as the waves attenuate and work-hardening effects become less significant. However, once the wave intensity is reduced to a critical value, dissipative effects likewise become less significant and the wave speed begins to increase. These results are in close agreement with those shown in Figure 37 for steady waves.

Figure 46 shows the effect of wave frequency on attenuation. One can readily see that higher frequency waves do attenuate more quickly, but this effect is not all that great. Of the three waves shown, the difference in pressure jump by the 5 cm position is only about 20%. The frequency difference is partly erased by wave spreading, and probably the higher frequency wave spread more quickly and therefore experience a quicker reduction in frequency content.

It is also possible to study the growth and decay of shock waves by considering the jump equations. These equations cannot give as much information as the direct approach just discussed, since stress wave profile and wave length cannot be calculated from the jump equations. However, the direct approach using the finite-difference technique is computationally a time-consuming and expensive means of solving the problem. If wave attenuation is sought, there should be more convenient means of doing this.

IV.E. THE USE OF JUMP EQUATIONS FOR ANALYZING NONSTEADY WAVE PROPAGATION.

A solution to the problem of shockwave propagation in a nonlinear dissipative material can be a complicated problem if one attempts to determine such wave properties as wavespeed, pressure profile, attenuation, and alteration of the wave as the wave propagates into a medium. Spence (1973) characterized wave propagation properties for viscoelastic materials.

Generally a detailed analysis requires solution of the momentum and mass balance equations. In particular, if one desires a quantitative evaluation, a numerical solution of these equations is usually required, but this can be an expensive and time consuming procedure, since the solution of the differential wave equation can involve a large number of simultaneous difference equations.

This can best be illustrated by considering the wave equation solved numerically in the preceding section:

$$E_T \frac{\partial^2 \alpha}{\partial x^2} + \frac{\partial E_T}{\partial X} \frac{\partial \alpha}{\partial X} = \frac{\rho}{\alpha_0} \frac{\partial^2 \alpha}{\partial t^2} + \frac{\partial}{\partial X} \left(E_1 \frac{\partial \dot{\alpha}}{\partial X} + E_2 \frac{\partial \ddot{\alpha}}{\partial X} \right) \quad \text{(IV.E.1)}$$

The constitutive law (for instance eq IV.C.3) can be conveniently written in the following form

$$p = Q_1(\alpha,\alpha_o) + Q_2(\alpha,\alpha_o)\dot{\alpha}^2 + Q_3(\alpha,\alpha_o)\ddot{\alpha} \quad \text{(IV.E.2)}$$

The functions Q_1, Q_2 and Q_3 can readily be determined from eq IV.C.3. For purposes of this discussion, it is convenient to use eq 2. E_T, E_1, and E_2 are functions of $\alpha,\dot{\alpha},\ddot{\alpha}$, so that the wave equation, which is basically the differential equations of motion, and continuity, is a nonlinear fourth order partial differential equation. Q_1, Q_2 and Q_3 are all continuous and differentiable functions of α and the initial ratio, α_o. The above equation was shown to accurately characterize the pressure response of snow to high rate compressive deformations.

In this section a solution to the stress wave problem is presented and compared to earlier results. The method used here entails the use of jump equations, often referred to as weak solutions. The shockwave is defined as a smooth one parameter family of points Y(t) such that Y(t) gives the material point at which the stress wave is located at time t. X is the position of the particle in the reference configuration, and x = x(X,t) is

the particle position for any time t. The intrinsic velocity of the wave is

$$V = \frac{d}{dt} Y(t) = \dot{Y} \qquad \text{(IV.E.3)}$$

If f (X,t) is any descriptive variable of the material, the jump in f, denoted as [f] is the difference in the values of f just behind and in front of the wave:

$$[f] = f^- - f^+ \qquad \text{(IV.E.4)}$$

where

$$f^- = \lim_{\delta \to 0} f(X-\delta, t)$$

$$f^+ = \lim_{\delta \to 0} f(X+\delta, t)$$

Here we assume the wave is propatating in the positive X direction. This characterization of a shockwave depicts the wave as a singular surface, i.e. the wave is assumed to have an insignificant wavelength, so that the only properties which can be garnered from this description are the jumps in variables across the wave. As a consequence, some information is lost, since the internal structure of the stress wave cannot be studied. However, the problem becomes mathematically much more manageable.

In the following the governing equations and widely recognized relations for stresswaves are again presented for more convenient reference. Then additional results are developed to make possible calculations of the growth and decay of stress waves by use of the jump equations. Finally, the current development is compared to earlier results.

In what follows, we assume the stress wave is propagating into an undisturbed medium. Thus $\alpha^+ = \alpha_o$, and the pressure p, particle velocity v, and density ratio rate $\dot{\alpha}$ ahead of the wave all vanish. Therefore,

$$[\alpha] = \alpha^- - \alpha_o \qquad \text{(IV.E.5)}$$

$$[p] = p^-$$

$$[v] = v^-$$

$$[\dot{\alpha}] = \dot{\alpha}^-$$

The derivative of the pressure p with respect to either time or position has the form

$$\dot{p} = -E_T\dot{\alpha} + E_1\ddot{\alpha} + E_2\dddot{\alpha} \qquad \text{(IV.E.6)}$$

$$p_x = -E_T\alpha_x + E_1\dot{\alpha}_x + E_2\ddot{\alpha}_x ,$$

where a subscripted x denotes differentiation with respect to X. Then the jumps in these variables may be shown to be

$$[\dot{p}] = -E_T^-[\dot{\alpha}] + E_1^-[\ddot{\alpha}] + E_2^-[\dddot{\alpha}] \qquad \text{(IV.E.7)}$$

$$[p_x] = -E_T^-[\alpha_x] + E_1^-[\dot{\alpha}_x] + E_2^-[\ddot{\alpha}_x]$$

E_T^-, E_1^-, and E_2^- are the values of E_T, E_1, and E_2 just behind the wave. The rate of change of [p] with respect to time may also be shown to be

$$[p]_t = -E_T^-[\alpha]_t + E_1^-[\dot{\alpha}]_t + E_2^-[\ddot{\alpha}]_t \qquad \text{(IV.E.8)}$$

The subscripted t implies differentiation with respect to time. In the above $[\dot{p}]$represents the change or jump in the value of the pressure derivative $\dot{p}$ across the wave, whereas $[p]_t$ gives the rate of change of the pressure jump [p] as the wave propagates through the medium.

For a plane wave propagating in the X direction, the two governing differential equations are the momentum and mass balance equations. These are;

$$\frac{\partial p}{\partial x} = -\rho_o\dot{v} \qquad \text{(IV.E.9)}$$

$$\frac{\partial v}{\partial X} = \dot{\alpha} / \alpha_o \qquad \text{(IV.E.10)}$$

These equations may be put in the form of jump equations in much the same manner as was done by Coleman (1964) and Chen and Gurtin (1971). The difference form for these equations are:

$$[\partial p/\partial X] = -\rho_o [\dot{v}] \qquad \text{(IV.E.11)}$$

$$[\partial v/\partial X] = [\dot{\alpha}/\alpha_o] \qquad \text{(IV.E.12)}$$

Alternate forms of these two equations are

$$[p] = \rho_0 V [v] \qquad \text{(IV.E.13)}$$

$$[v] = -V[\partial x/\partial X] = -V][F] \qquad \text{(IV.E.14)}$$

$$[v] = -\frac{V}{\alpha_o}[\alpha] \qquad \text{(IV.E.15)}$$

F is the deformation gradient, $\partial x/\partial X$.

Equations 13 and 15 may be used to arrive at

$$V^2 = -\frac{\alpha_o}{\rho_o}\frac{[p]}{[\alpha]} \qquad \text{(IV.E.16)}$$

The secant modulus for the material is defined as

$$\bar{E_s} = -\frac{[p]}{[\alpha]} \qquad \text{(IV.E.17)}$$

so that the wave speed V then has the form

$$V^2 = \alpha_o \bar{E_s}/\rho_o \qquad \text{(IV.E.18)}$$

In addition to the above, the familiar compatibility relation for shockwaves (Coleman et al 1964) is of considerable use in the study of shockwaves. If f(X,t) is any function of position and time, the compatability relation requires that

$$[f]_t = [\dot{f}] + V[f_x] \qquad \text{(IV.E.19)}$$

The above relations, eqs 11 - 19, are considered to be the standard jump equations for the propagation of shockwaves in materials. They have been used extensively in previous studies by Coleman et al (1964), Carrol et al (1973), Chen et al (1971), and others to characterize the manner in which shockwaves are propagated through materials, irrespective of the material properties.

We now use the foregoing relations to evaluate the growth and decay rates of shockwaves in snow. Differentiating eq 15 and using eq 19 with f = v results with

$$\dot{V}[\alpha] + V[\alpha]_t = -\alpha_o \, ([\dot{v}] + V[v_x]) \qquad \text{(IV.E.20)}$$

Then substituting eqs 11 and 12 gives

$$\dot{V}\,[\alpha] + V[\alpha]_t = \frac{\dot{\alpha}_o}{\rho_o}\,[p_x] - V[\dot{\alpha}] \qquad \text{(IV.E.21)}$$

This equation is then further modified by using eq 7, eq 9 with $f = \alpha$ and $f = \dot{\alpha}$, and eqs 13 and 15. After some algebra, we get

$$\frac{\rho_o V[\alpha]}{\alpha_o}\,\dot{V} = -(E_T^- + E_s^-)\,[\alpha]_t + (E_T^- - E_s^-)\,[\dot{\alpha}] \qquad \text{(IV.E.22)}$$

$$+ E_1^- ([\dot{\alpha}]_t - [\ddot{\alpha}]) + E_2^- ([\ddot{\alpha}]_t - [\dddot{\alpha}])$$

V may be eliminated by differentiating eq 15 and substituting into eq 22 for $\dot{V}$. The result is

$$\tfrac{1}{2}(3E_T^- + E_s^-)\,[\alpha]_t - \tfrac{3}{2}\,E_1[\dot{\alpha}]_t = (E_T^- - E_s^-)\,[\dot{\alpha}]$$

$$- E_1[\ddot{\alpha}] + E_2^-\,(\tfrac{3}{2}\,[\ddot{\alpha}]_t - [\dddot{\alpha}]) \qquad \text{(IV.E.23)}$$

As can be seen here, the full collection of moduli determine the rate of change of $[\alpha]$ for the above form of the wave equation.

Some additional criterion for determining what constitutes the wave amplitude is needed. For instance, one can require that the wave has passed a

point where the material is no longer being compressed, i.e. when $\dot{\alpha} = o$, which would be equivalent to requiring $[\dot{\alpha}] = o$. Rather than this, we impose the requirement that the wave has passed a point when the peak pressure has been reached. This is equivalent to the condition

$$[\dot{p}] = o \qquad \text{(IV.E.24)}$$

This then implies, with eq 7

$$-E_T^- [\dot{\alpha}] + E_1^- [\ddot{\alpha}] + E_2^- [\dddot{\alpha}] = o \qquad \text{(IV.E.25)}$$

With this, $[\ddot{\alpha}]$ can be eliminated from eq 23, and we get

$$\frac{1}{2}(3E_T^- + E_s^-)[\alpha]_t - \frac{3}{2} E_1^- [\dot{\alpha}]_t = -E_s^- [\dot{\alpha}] + \frac{3}{2} E_2^- [\ddot{\alpha}]_t \qquad \text{(IV.E.26)}$$

Eq 26, in conjunction with eqs 2, and 8 may be used to study the manner in which the stress wave propagates through snow. Given an initial set of conditions, say $[\alpha]$ and $[\dot{\alpha}]$, these equations may be solved to determine $[p]_t$, $[\alpha]_t$ and $[\dot{\alpha}]_t$ and by numerical integration, the temporal variation of $[p]$, $[\alpha]$, and $[\dot{\alpha}]$ can be evaluated.

Results in Section II indicate have the acceleration modulus is extremely small, and the terms $E_2^- [\ddot{\alpha}]_t$ in eqs 8 and 26 may be neglected. Therefore we will assume that effects associated with E_2^- can be neglected and drop this term from eq 26.

The formulation developed here may now be compared to results obtained in the earlier development where Eq 1 was integrated by a finite difference method. In that section, the material constitutive equation for volumetric deformation was given by eq 2 where Q_1, Q_2, and Q_3 are

$$Q_1 = \frac{2^{Y_o} J}{3\alpha} \exp(-\phi\alpha/\alpha_o) \ln(\alpha/(\alpha-1))$$

$$Q_2 = -\frac{\tau^2}{6\alpha} \left((\alpha-1)^{-4/3} - \alpha^{-4/3} \right) \qquad \text{(IV.E.27)}$$

$$Q_3 = -\frac{\tau^2}{\alpha}\left((\alpha-1)^{-1/3} - \alpha^{-1/3}\right)$$

In the earlier analysis, it was determined that a finite difference solution to the wave equation gave very reasonable results when compared to what experimental results are available. However, as is common in finite difference solutions of higher order differential equations, stability problems were incurred and had to be solved, and the required grid size resulted in long computation terms.

Eq 26, with the term with E_2^- eliminated, can readily be put in a difference from in order to obtain expressions for $[\alpha]_t$ and $[\dot{\alpha}]_t$ at any instant, t. This equation and the compatability equation eq 19 with f = α can then be used jointly to solve for $[\alpha]_t$ and $[\dot{\alpha}]_t$ The compatability condition is

$$[\alpha]_t = [\dot{\alpha}] + V\,[\alpha_x] \qquad \text{(IV.E.29)}$$

α_x can be evaluated by expanding α into a Taylor series about a point just behind the shockwave. To demonstrate this, consider Figure 47, which shows two α-profiles resulting from the shockwave. The solid line describes the wave profile at a time t^j, and the dashed line represents the wave profile at time $t^{j-1} = t^j - \Delta t$, where Δt is a small time increment. The wave has progressed a distance of $\Delta X = V\Delta t$ during this time from position X_{j-1} to X_j. α^j_{j-1} represents the density ratio at time t^j and position $X_{j-1} = X_j - V\Delta t$. A Taylor series expansion of α about point X_{j-1} is of the form

$$\alpha^j_{j-1} = \sum_{n=0}^{\infty} \frac{1}{n!} \frac{\partial^n}{\partial t^n} \alpha\,(t^{j-1}, X_{j-1})\,(\Delta t)^n$$

which may be truncated to

$$\alpha^j_{j-1} = \alpha^{j-1}_{j-1} + \dot{\alpha}^{\,j-1}_{j-1}\,\Delta t$$

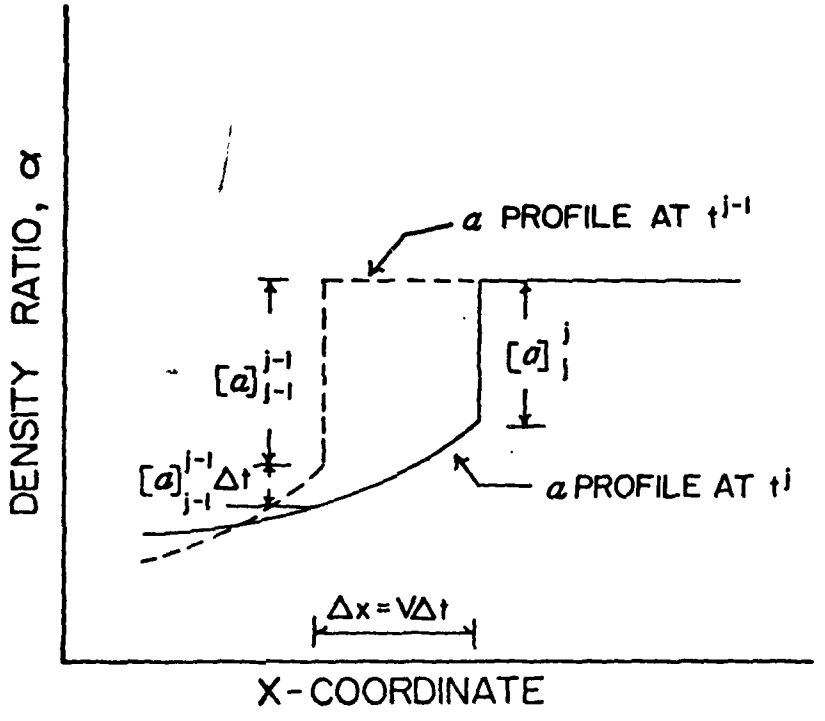

Figure 47. Idealized density profiles in a shockwave.

for small values of Δt. Then, $V[\alpha_x]$ can be shown to have the form

$$V[\alpha_x] = V \frac{(\alpha_j^j - \alpha_{j-1}^j)}{\Delta x}$$

$$= \frac{\alpha_j^j - \dot{\alpha}_{j-1}^{j-1} - \dot{\alpha}_{j-1}^{j-1} \Delta t}{\Delta t}$$

and eq 29 then has the difference form

$$[\alpha]_t^j = [\dot{\alpha}]_j^j + \frac{\alpha_j^j - \alpha_{j-1}^{j-1} - \dot{\alpha}_{j-1}^{j-1} \Delta t}{\Delta t} \qquad \text{(IV.E.30)}$$

and eq 26 in difference form becomes

$$\frac{1}{2}\left(3(E_T^-)_j^j + (E_s^-)_j^j\right)[\alpha]_{tj}^j - \frac{3}{2}(E_1^-)_j^j [\alpha]_{tj}^j = -(E_s^-)_j^j [\dot{\alpha}]_j^j \qquad \text{(IV.E.31)}$$

Upon using eqs 30 and 31 to evaluate $[\alpha]_t$ and $[\dot{\alpha}]_t$ at any instant t^j where the wave is located at position X_j, then $[\alpha]$ and $[\dot{\alpha}]$ can be calculated by direct step forward integration.

Figures 48 - 51 illustrates the results of the method described above. In figure 48, wave pressure attenuation in medium density snow is calculated and compared to experimental results of Wisotksi and Snyder (1964). As can be seen, agreement with the data is excellent, although one should notice that there is about a twenty five percent difference between the density used in the calculations and in snow studied by Wisotski and Snyder. It is anticipated that the attentuation in the lower density snow should be larger. Unfortunately there still is a shortage of good shockwave data for making a more rigorous evaluation of the theory.

Figure 49 illustrates the attenuation of the pressure jump due to the shockwave. Also included in the figures are results obtained by the full numerical solution of eq 1 in the preceding section and in the paper by Brown

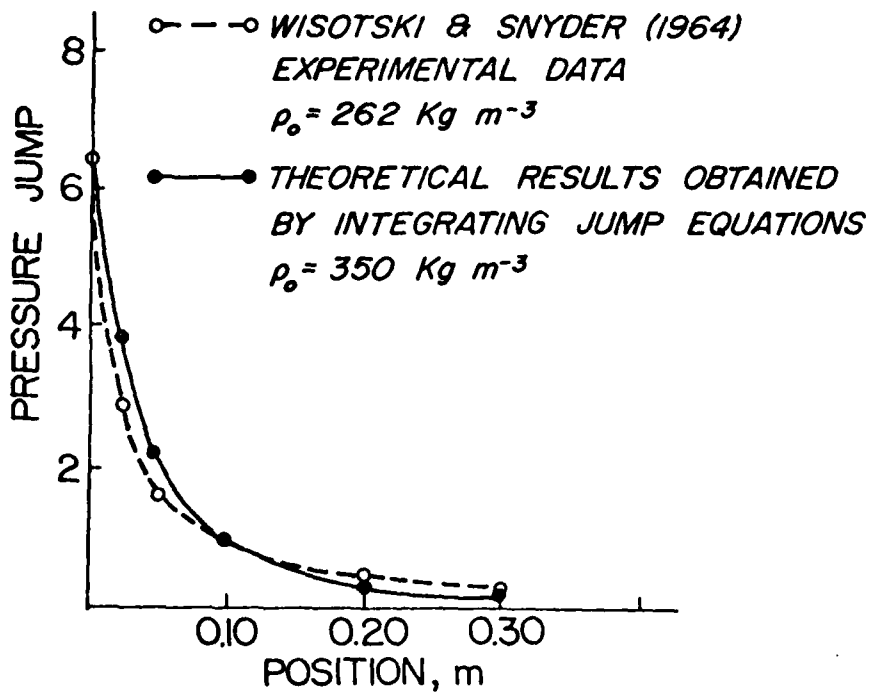

Figure 48. Comparison of theoretical solution to experimental data.

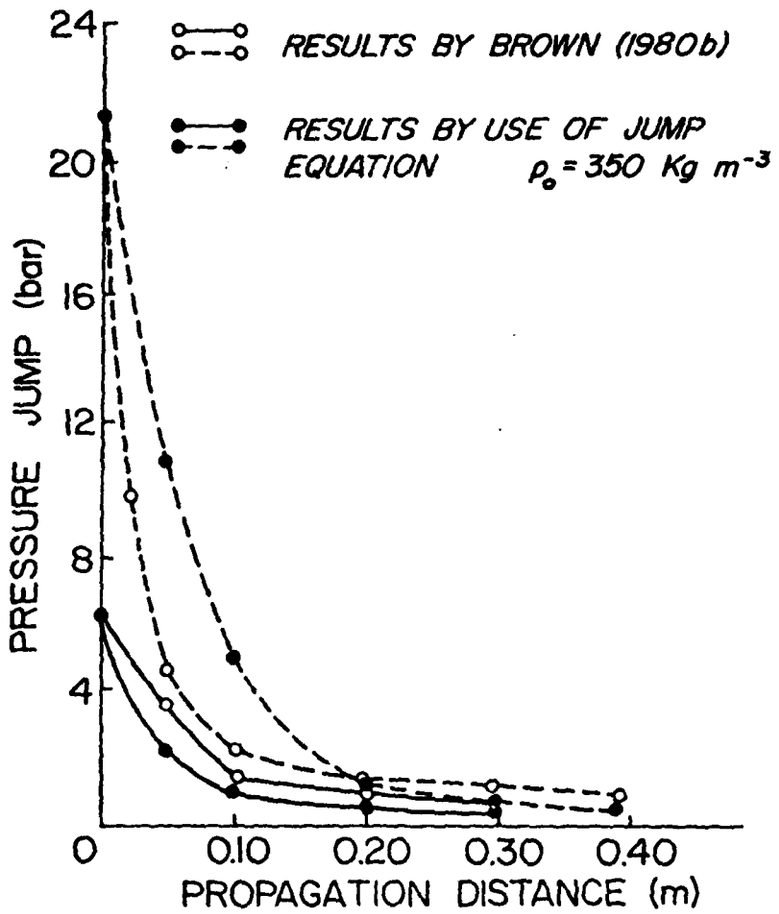

Figure 49. Comparison of two methods for calculating shockwave attenuation.

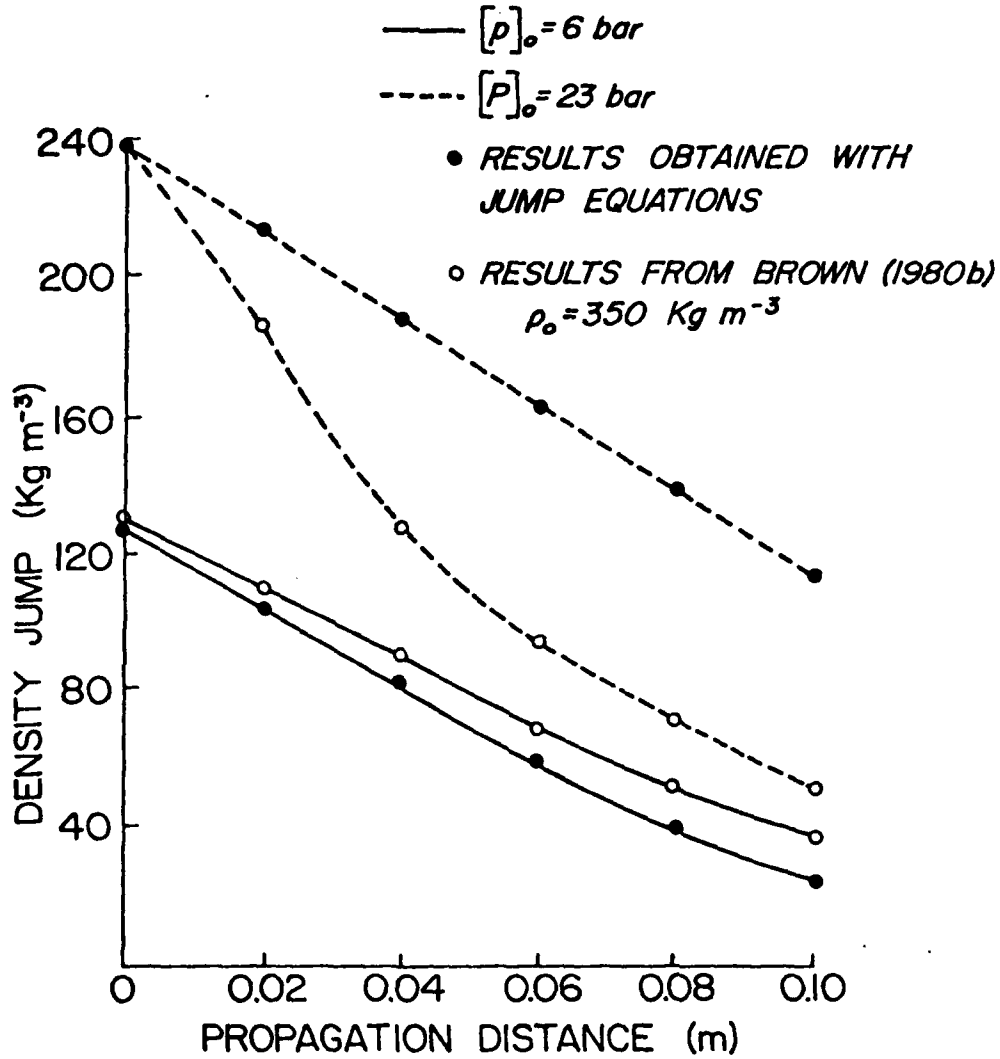

Figure 50. Comparison of two theoretical solution techniques (Sections IV C & D).

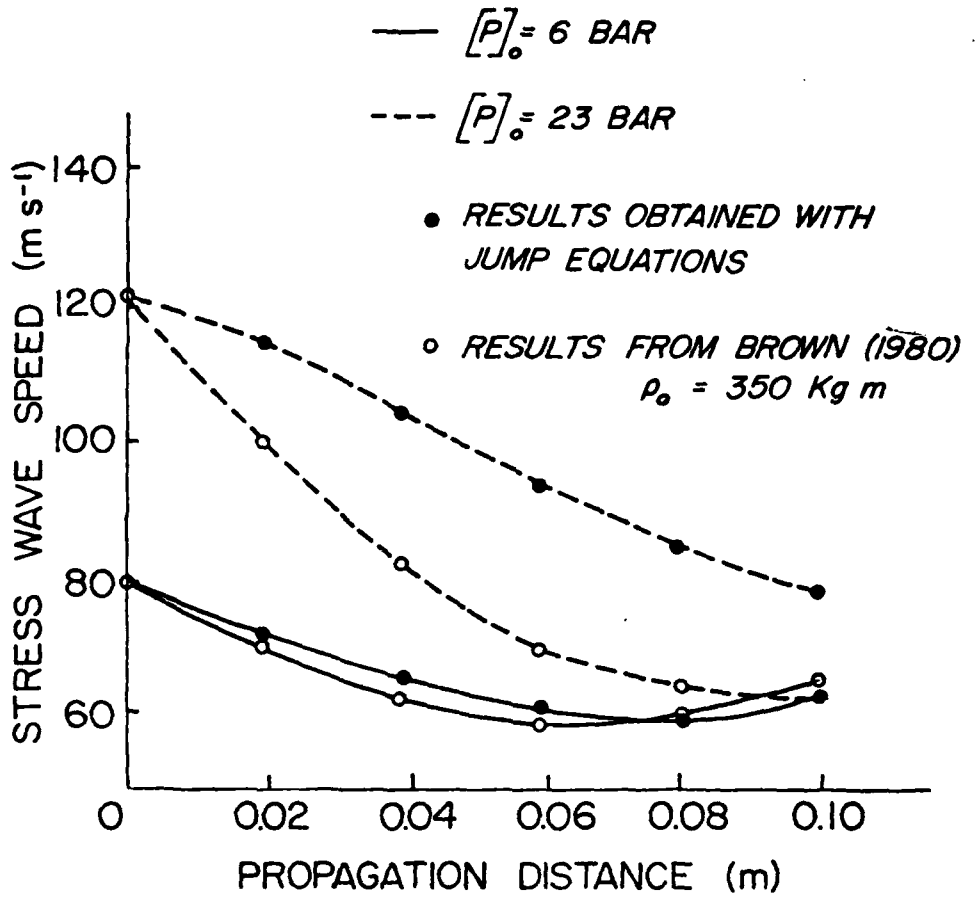

Figure 51. Variation of wave speed with propagation distance.

(1980b) and in Section IV.C. As can be seen, some discrepancies between the two theories emerge. There appears to be a fairly good correlation between the two theories for the lower pressure waves, but for a pressure wave with an initial amplitude of 21 bar, the two solutions diverge rather quickly. It is not yet determind which theory is more correct. While the direct finite difference solution of eq 1 would represent a more rigorous method than the method presented here, the stability problems associated with numerical solution of high order difference equations may introduce some numerical errors. Unfortunately there is no experimental data with which to compare these results.

Figure 50 compares the attenuation in the density jump, and Figure 51 illustrates how the wave speed changes as the wave propagates through a homogeneous snowpack. In both of these figures there do exist differences between the two formulations although the results do show very similar trends.

The method described here for characterizing shockwave propagation in materials such as snow has not been studied extensively in the past. When jump equations have been used, their use has been restricted almost entirely to calculations of density jump or wave speed. Very little effort has been made toward evaluating wave attentuation or growth.

As has been shown, the use of weak solutions do appear to be a viable means of investigating shockwaves without having to resort to complicated and expensive numerical solution of the wave equation. While a numerical solution was employed here, effort required to obtain a solution was but a small fraction of the effort required for the solution of eq 1 in the paper by Brown (1980b).

The numerical results here do imply that snow does strongly attenuate in plastic stress waves. As has been shown, the wave amplitude is reduced to about 10% of its original amplitude within 10 cm of propagation.

V. EXPERIMENTAL PROGRAM ON STRESS WAVES IN SNOW.

Other than the pioneering work by Napadensky (1964), there has been very little significant laboratory work on plastic shock waves in snow. Other work includes studies on shock waves in wet snow by Wakahama and Sato(1977). Brown (1979[a], [b], [c] has made theoretical studies of steady and non-steady waves in snow, and the results appear reasonable when compared to what little experimental evidence is available for stress waves.

In order to improve on the quantity and quality of shock-wave data, an electromagnetic stress-wave generator has been constructed, and this instrument is described in detail here. Other methods of generating shock waves could have been used. For instance, explosives can be used to produce a wide range of wave amplitudes, although wave frequency is not an easily controlled parameter, and explosives also usually have a great deal of experimental scatter. The electromagnetic generator was chosen, since it appeared to provide an optimum combination of pressure and frequency capability. In addition it has negligible experimental scatter and is easy to use. One drawback is the danger associated with high voltages, and such a system must have incorporated into it safety features to minimize this aspect of the system. However, the use of explosives also requires implementation of safety features.

Basically, the electromagnetic generator consists of a 20 kV capacitor with a capacitance of 30 μF, a triggering unit, a spark-gap trigger, and a system of conducting plates and load strips. The generator works on the principle that when two high-energy electric currents are conducted in opposite directions along adjacent parallel strips, a strong repulsive electromagnetic force is generated to force the two strips apart.

The capacitator and high-voltage side of the trigger are both completely submerged in a tank filled with transformer oil, thereby insulating components

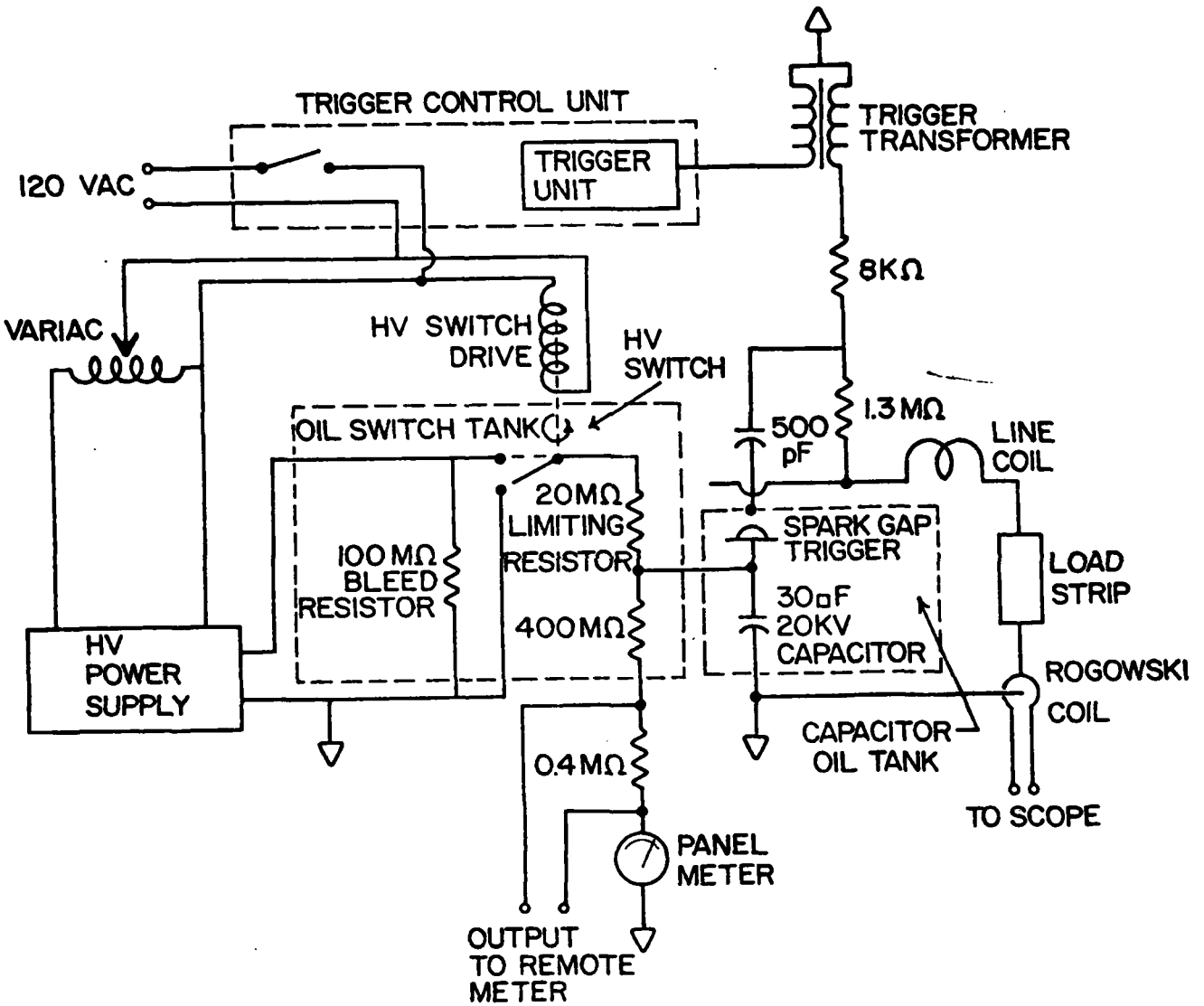

Figure 52. Schematic of stress wave generator.

and reducing any corona effects that might occur during charging of the capacitor. A 20 kV regulated power supply is used to charge the capacitor, and charging time generally is less than 5 min. The capacitor voltage can be read from either a gauge on the instrument panel or from a digital voltmeter if more accuracy is required. A 400 MΩ dropping resistor is used to drop the voltage to the gauge. The digital voltmeter is connected to opposite ends of a 0.4 MΩ resistor in series with the dropping resistor, so that a 1 V output on the digital meter corresponds to a 1 000 V charge in the capacitor. The digital voltmeter is connected remotely to the generator, so that charge voltage can be monitored from outside the cold room in which the testing is done.

As can be seen in figure 52, the electrical circuitry consists of three separate components: (1) the trigger control system; (2) the power supply, capacitor, and conducting elements; and (3) the monitoring instruments. While these three separate systems are interconnected, they serve different purposes.

The trigger control unit outlined in Figure 52 serves several purposes. First it controls power to the entire system. Second, when the power is switched on, an electromagnet activates a high-voltage switch to close the charging circuit to allow the capacitor to be charged. If the system is turned off or a power failure occurs, the switch automatically opens to allow a limiting resistor to discharge the capacitor. In addition, a 100 MΩ bleed resistor is also permanently installed in the circuit to bleed the capacitor down in case the H.V. switch for the other resistor should fail. The control unit also controls the power to the high-voltage power supply and contains the trigger module which, by means of a transformer, pulses the spark gap with a 25 kV pulse. This ionizes the gases in the trigger which closes the circuit and allows the current to be conducted across the spark gap, through a control coil to the load strip and to the ground side. The coil is used to make the inductance of the complete system large enough so that the current will not

exceed the maximum allowable current for the spark gap.

V.A ELECTROMAGNETIC THEORY

The generator is a LRC circuit, and the system performance is determined by the differential equation

$$\frac{d^2}{dt^2}(LQ) + R\frac{dQ}{dt} + \frac{Q}{C} = 0 \qquad \text{(V.A.1)}$$

where Q is the instantaneous capacitor charge, L is the circuit inductance, R is the total circuit resistance, and C is the capactitance. In the underdamped mode, the solution to eq 1 is

$$Q(t) = [Q_o \exp(-at)]\left(\frac{a}{\omega}\sin \omega t + \cos \omega t\right), \qquad \text{(V.A.2)}$$

$$a = R/2L, \qquad \text{(V.A.3)}$$

$$\omega = 1/LC - (R/2L)^2 \qquad \text{(V.A.4)}$$

The instantaneous current i(t) can be shown to be

$$i(t) = \frac{Q_o}{\omega LC}\exp(-at)\sin \omega t. \qquad \text{(V.A.5)}$$

The current is exponentially damped, and if T is the period of the oscillating current, the full-cycle peak-to-peak ratio of the current amplitude is

$$\frac{A_3}{A_1} = \exp(-aT), \qquad \text{(V.A.6)}$$

where A_1 and A_3 are the peak current values of two successive complete cycles. The values of L and C may then be solved for in terms of C, T, and A_3/A_1. This yields (Snell and others, 1973)

$$R = \frac{2T \ln (A_3/A_1)}{C[(2\pi)^2 + (\ln (A_3/A_1))^2]}, \qquad \text{(V.A.7)}$$

$$L = \frac{T^2}{C[(2\pi)^2 + (\ln (A_3/A_1))^2]}. \qquad \text{(V.A.8)}$$

The pressure p produced between the two conducting strips varies with the current as

$$p = \frac{\mu}{2}\left(\frac{i}{w}\right)^2 , \qquad \text{(V.A.9)}$$

where w is the strip width, and μ is the magnetic permeability of the material separating the strips, which, in this case is 0.254 mm thick Mylar. Equation 9 is valid so long as the strip width w is large compared to the separation of the conducting plates.

V.B ASSESSMENT OF GENERATOR PERFORMANCE

In its present form, the generator has about 6000 J of energy when charged to 20 kV. Maximum current with this configuration is about 160 kA. The spark gap, however, is designed for a maximum current of about 100 kA, so the maximum voltage used to date is about 15 kV. This level of current and voltage was however, found to be sufficient to produce high-pressure shock waves in snow.

When the system was originally completed and first tested, the resistance and inductance were found to be 3.75 mΩ and 85 nH, respectively, and a capacitor voltage of 15 kV resulted in currents of about 275 kA, which, after about 20 shots, destroyed the spark gap. After that, the control coil shown in figure 52 was placed in series between the capacitor and load strips to raise L and R to values of 650 nH and 19 mΩ, which keeps the maximum current below 100 kA when the capacitor voltage is less than 15 kV. This is significantly lower than the potential system output (450 kA at 20 kV) when the control coil is removed, but to date a spark gap to handle these current levels has not been constructed for the stress-wave generator.

The current in the circuit is monitored by a Rogowski coil that is encircled by the conducting strips near the end of the load strips. This coil is simply a length of insulated wire that is looped and twisted tightly into a shorter length. When this is placed adjacent to the conducting strip (in this case, at a point near the load strip), the electromagnetic field set up by the large current produces a voltage across the leads to the Rogowski coil. Actually it

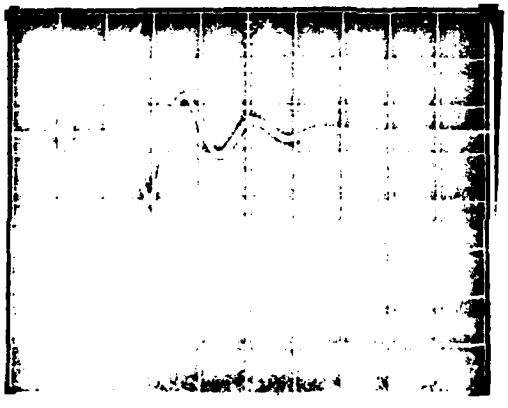

Figure 53. Typical Rogowski coil output.

makes little difference if the coil encircles the strip or is encircled by the strip itself, as was done in our case. The electromagnetic field produces a voltage across the coil leads in either case. The voltage across the leads from the Rogowski coil (Snell and others, 1973) is proportional to the instantaneous voltage in the capacitor. The output from a typical oscilloscope trace of the coil output is shown in figure 53. Snell and others (1973) have shown that the maximum current can be determined from the period T of the Rogowski output and the full-cycle peak-to-peak ratio A_3/A_1 of the voltage generated across the coil. This relation is

$$I_{max} = V_o C \frac{2\pi}{T} \left(\frac{A_3}{A_1}\right)^{1/4} \qquad \text{(V.B.1)}$$

From figure 53, $A_3/A_1 = 0.611$, T = 30 μs, so for a capacitance of 30 μF and a voltage of 15 kV, a maximum current of 84 kA is developed. Under these conditions, a pressure in excess of 5 000 kPa can be produced for a specimen with a 10 cm x 2.5 cm cross-section.

The test procedure is relatively simple. While the capacitor banks are uncharged, the specimen is cut and shaped and mounted on the load strips, and the pressure transducer is then positioned at the top end of the specimen. Then the capacitor bank is charged, which generally takes less than 5 min. When the desired voltage is reached, the spark gap is pulsed, thereby completing the test. The Rogowski coil and transducer output are recorded on trace oscilloscopes. Repeatability of the system is excellent, with generator output scatter being less than 5%.

V.C. TEST RESULTS WITH THE ELECTROMAGNETIC STRESS WAVE GENERATOR

A testing program was initiated during the research project funded by the Army Research Office. The purpose of the project was to evaluate the propagation of shockwaves in low density snow. In all, about 150 shockwave tests were run on

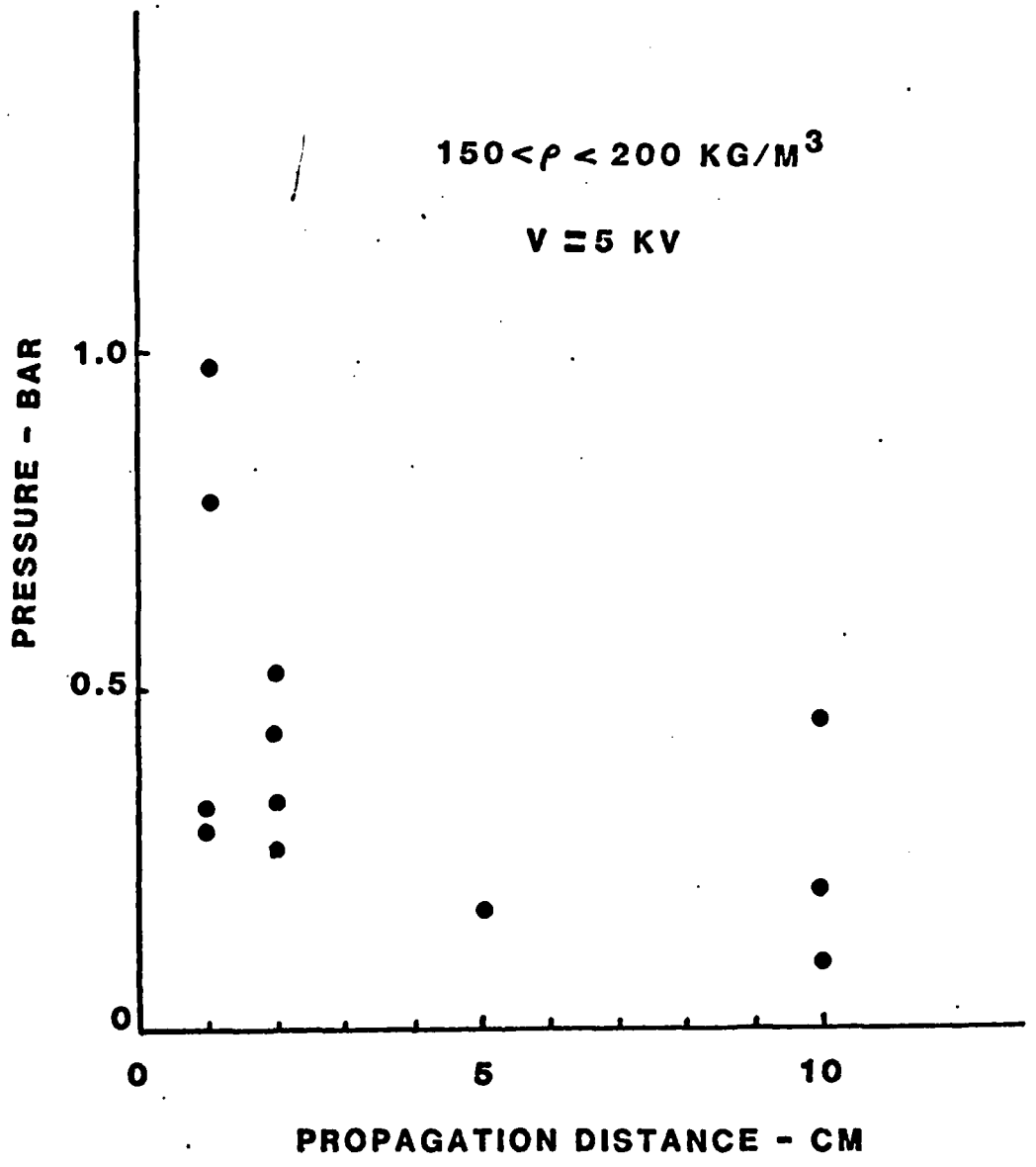
150<ρ<200 KG/M3
V=5 KV
PRESSURE - BAR
1.0
0.5
0
0
5
10
PROPAGATION DISTANCE - CM

Figure 54.

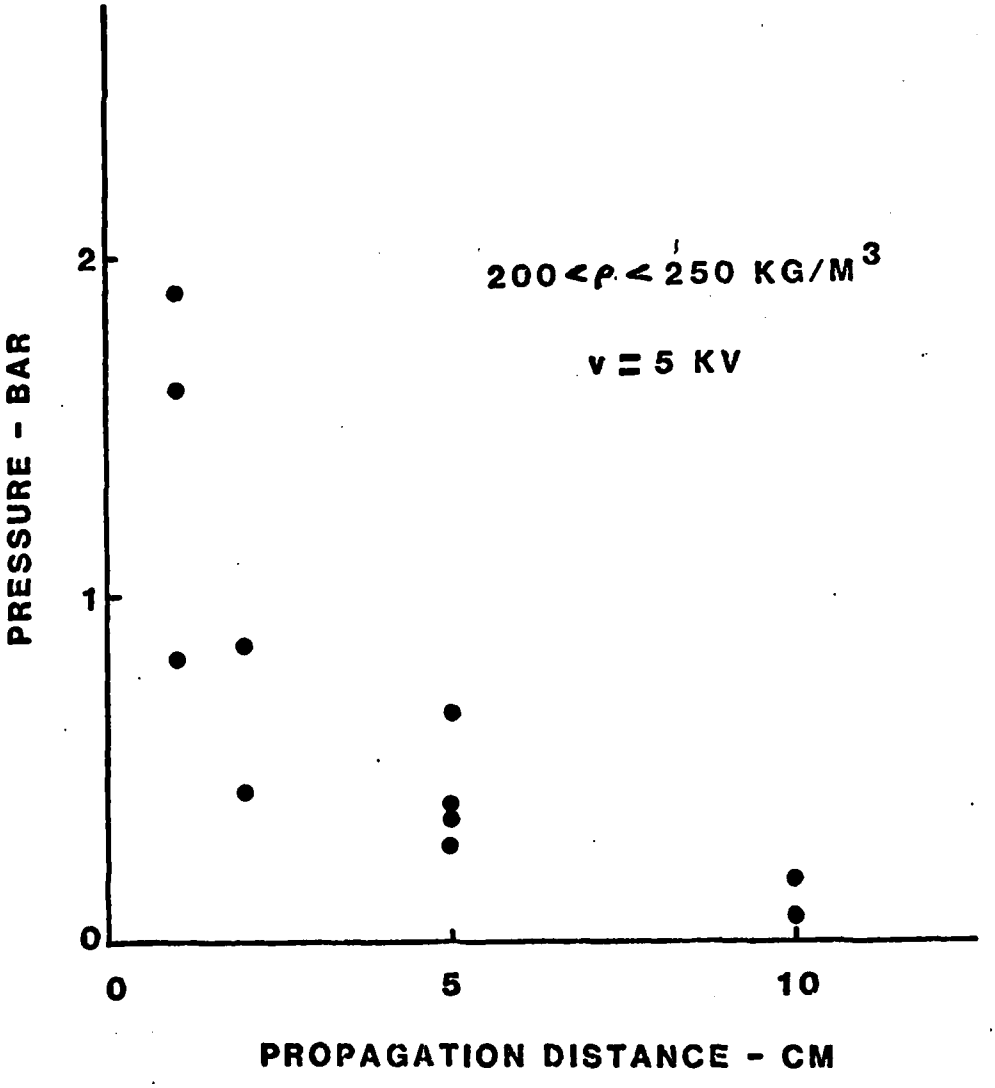
200 < ρ < 250 KG/M3
v = 5 KV
PRESSURE - BAR
2
1
0
0
5
10
PROPAGATION DISTANCE - CM

Figure 55.

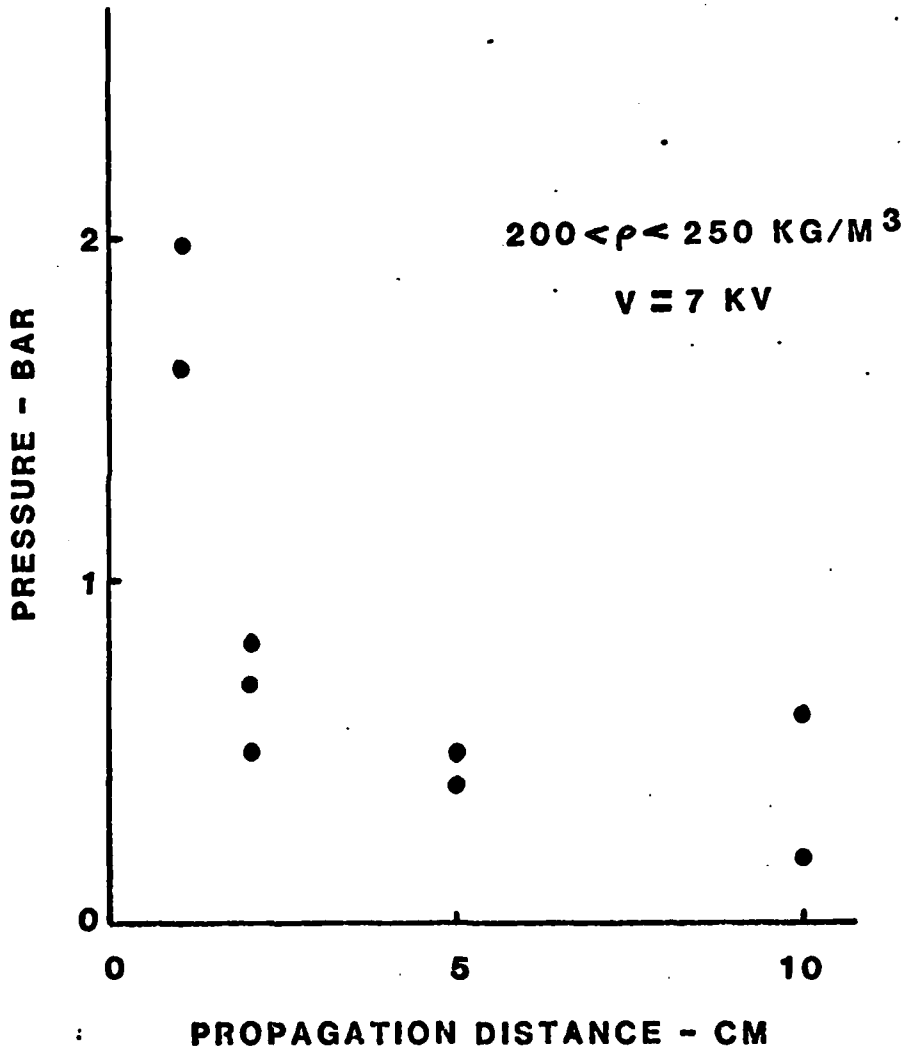
200 < ρ < 250 KG/M 3
V = 7 KV
PRESSURE - BAR
2
1
0
0
5
10
PROPAGATION DISTANCE - CM

Figure 56.

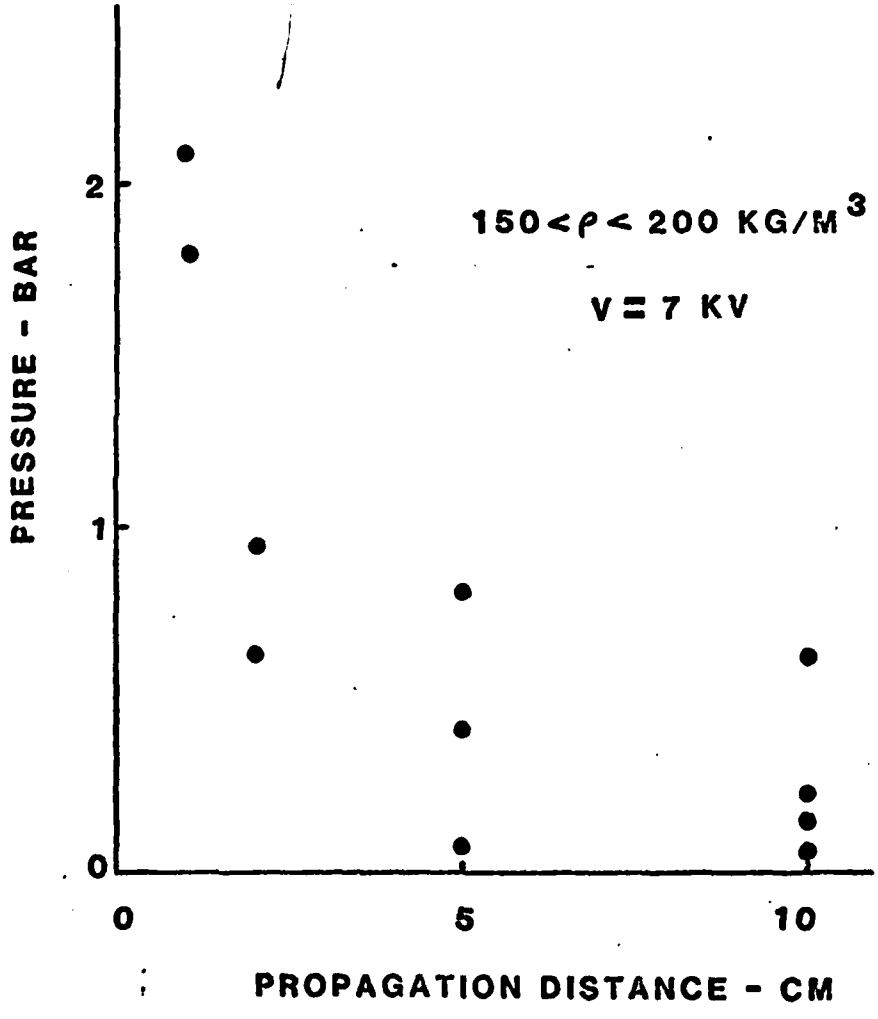
PRESSURE - BAR
2
1
0
150<ρ< 200 KG/M3
V= 7 KV
0
5
10
PROPAGATION DISTANCE - CM

Figure 57.

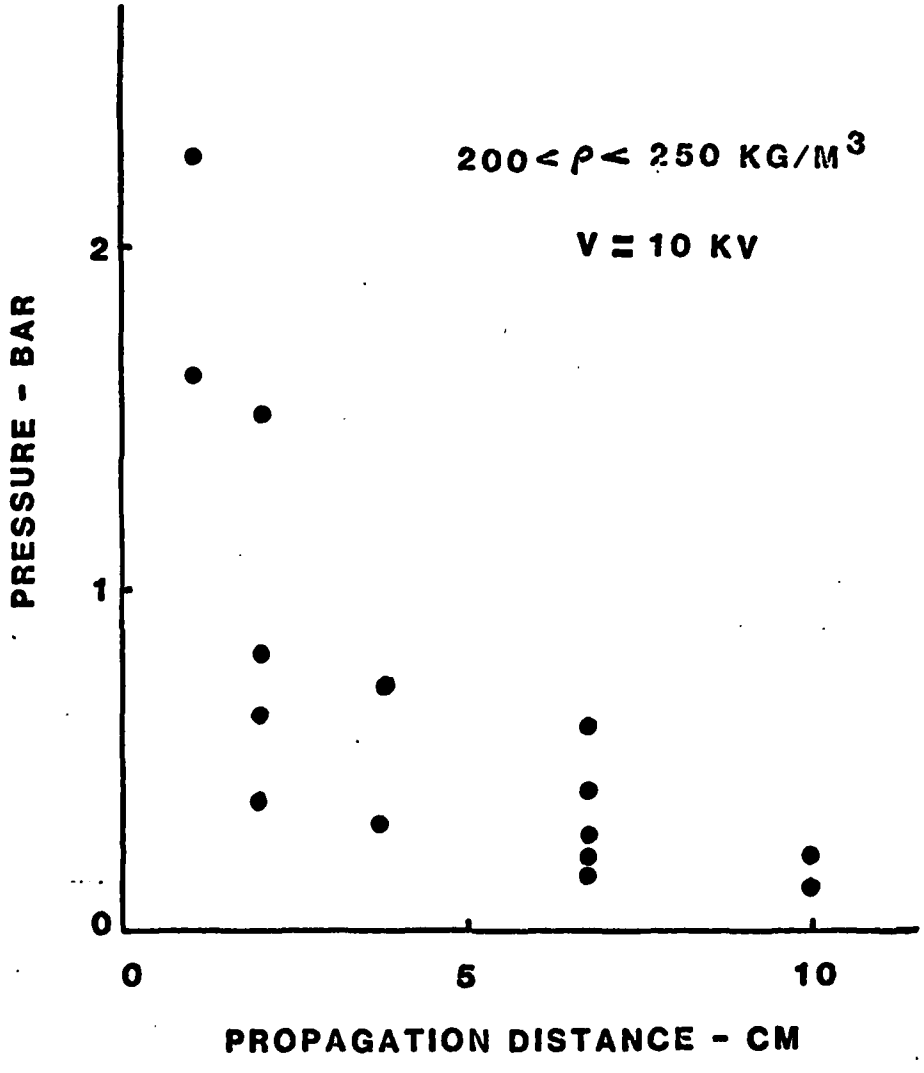
200 < ρ < 250 KG/M3
V = 10 KV
PRESSURE - BAR
2
1
0
0
5
10
PROPAGATION DISTANCE - CM

Figure 58.

specimens with initial densities ranging from 150 Kg m^{-3} to 300 kg m^{-3}. The reduced data is represented in Figures 54-58. These tests are separated into ranges of density and the pperating voltage of the stress wave generator.

As was indicated earlier, the spark gap trigger was incapable of withstanding currents in excess of 100 kA, even though the stress wave generator had the capability of producing currents as large as 460 kA. Therefore, the tests had to be run at pressures which were only about 5% of its full capability. Financial constraints would not allow the purchase of a trigger which could handle these large currents.

In all tests, natural snow gathered from the Bridger Mountains was used. Seived snow normally has densities in excess of 350 kg m^{-3} and hence could not be used. In addition seived snow has different mechanical properties than natural snow of comparable densities, since seiving alters the granular bonding and the manner in which the grains interact with each other during loading and deformation. Since interest was in natural snow, it was decided to not use seived snow.

The decision to use natural snowpack resulted with its own set of problems. For instance, natural snowpack is normally nonhomogeneous. Density tends to vary considerably, and it is also difficult to avoid finding small ice crusts, surface hoar layers or sun crust layers in the snow. Sometimes these layers are very hard to detect. However, they do affect the nature in which stress waves are propoagated through snowpack. They act as a surface which reflects part of the wave if the surface is perpendicular to the propagation direction.

Natural snow is also much more difficult to handle and test than seived snow, particularly if the density is low. Often specimen damage can occur, thereby resulting with bad test results. In addition, it is often difficult to obtain good surface contact between the specimen and loading strip and betweeen the specimen and the pressure transducers.

The difficulties cited above results with an abnormally large number of bad shockwave tests. Of the approximately 150 tests that were run, only a little more than 50 tests gave valid results, and these are shown in Figures 54-58. These tests, however, do form a basis upon which to evaluate shockwave propagation properties of low density snow.

At the time of the writing of the report, an analytical solution of nonsteady wave propagation in low density snow was being worked on but as of then, unfinished. This solution was was based on the neck growth model described earlier in this report.

The test data does show that shockwaves do attenuate rapidly in low density snow. Shockwave amplitude drops to less than 10 percent within 10 cm of propagation distance. These results are consistent with results obtained previously for higher density snow.

VI. CONCLUSIONS

Presented in this report has been the research efforts of the author during the three year period of a research grant funded by the Army Research Office, Research Triangle Park, NC. The purpose of the grant was the investigation of high rate volumetric properties of snow with special emphasis on shockwave propagation. It is felt that progress was made in gaining a better understanding of the unique properties of snow when subjected to high rate deformations. Applications of theory to such problems as vehicle mobility in snow and shockwave propagation has been shown to give results which seem realistic and reasonable. This last phrase was used, since there still does not exist enough experimental data to draw definite conclusions.

More work still needs to be done to gain a better understanding of the high rate properties of snow. For instance, a constitutive law to accurately describe the behavior of snow under multi-axial deformations needs to be developed. Such a result could find application to a number of problems, including vehicle gradeability, penetration mechanics, shear wave propagation, to name a few. In addition, there is still a need for more data, so continued shockwave testing and high rate testing should also be encouraged when possible.

VII. REFERENCES

Abele, G. and Gow, A. (1975) Compressibility Characteristics of Undisturbed Snow. USA CRREL Research Report 336.

Abele, G. and Gow, A. (1976) Compressibility Characteristics of Compacted Snow. USA CRREL Report 76-21.

Abele, G. and Haynes, F. D. (1979) Effect of Water Content on Snow-water Mixtures. USA CRREL Report 79-2.

Ames, W. F. (1965) Nonlinear Partial Differential Equations. Academic Press, New York, NY.

Bowles, D. and Brown, R. L. (1981) A Stress Wave Generator for Shockwave Studies in Snow and Ice. Journal of Glaciology (in press).

Brown, R. L. and T. E. Lang (1973). On the Mechanical Properties of Snow and Its Relation to the Avalanche Rroblem. 11th Annual Symposium on Engineering Geology, Pocatello, Idaho.

Brown, R. L. (1976) "A Thermodynamic Theory for Simple Materials Representable by Integral Expansions". International Journal of Engineering Science Vol. 14, No. 11.

Brown, R. L. (1979) "A Study of Vehicle Performanee in Snow: Journal of Terra-Mechanics, Vol. 16, No. 4.

Brown, R. L. (1979) "A Volumetric Constitutive Law for Snow Subjected to Large Strains and Strain Rates", U. S. Army Cold Regions Research & Engineering Report 79-20

Brown, R. L. (1980) "Stress Waves in Snow", Journal of Glaciology, Vol. 25, No. 91.

Brown, R. L. (1980) "An Analysis of Nonsteady Pressure Waves in Snow". Journal of Glaciology, Vol. 25, No. 92.

Brown, R. L. (1980) "A Volumetric Constitutive Law Based on a Neck Growth Model". Journal of Applied Physics, Vol. 51, No. 1.

Brown, R. L. (1981) "Application of Energetics to Vehicle Mobility Problems in Snow". (Forthcoming as a CRREL Report).

Brown, R. L. (1981) "Stress Wave Propagation in Alpine Snow", Journal of Glaciology (in press).

Brown, R. L. (1981) "An Analyses of Vehicle Power Requirements in Deep Snowpack", Journal of Terramechanics (in press).

Brown, R. L. (1981) "A Means of Evaluating Stress Wave Propagation in Snow", Cold Regions Science and Technology, (submitted).

Butcher, B. M., Carroll, A. Holt (1974) "Shockwave Compaction of porous Aluminum", Journal of Applied Physics, Vol. 45, No. 9.

Chen, P. and M. E. Gurtin (1971). "The Growth of One-dimensional Shockwaves in Elastic Nonconductors". Int. J. Solids and Structures. Vol. 7, pg. 5.

Carrol, M. and A. Holt (1973). "Steady Waves in Ductile Porous Solids. J. Appl. Physics, Vol. 44.

Coleman, B. D. and M. E. Gurtin (1967) "Thermodynamics with Internal State Variables" Journal of Chemical Physics, Vol. 47, No. 2.

Desrues, F. Darve, E., Flovigny, P., Novarre, and A. Tarllefer (1980) "An Incremental Formulation of Constitutive Equations for Deposited Snow. Journal of Glaciology, Vol. 25, No. 92.

Harrison, W. L. (1956) "Study of Snow Values Related to Vehicle Performance". U. S. Army Ordinance Corps LLRB Report No. 23.

Harrison, W. L. (1975) "Vehicle Performance Over Snow". Math Model Validation Study. USA CRREL TR 268.

Harrison, W. L. (1981) "State of the Art in Field and Terrain Evaluation" presented at 7th International Conference of ISTVS) to appear in Journal of Terramechanics.

Johnson, J. B. (1978) "Stress Waves in Snow". (Ph.D. Thesis, Univ. of Washington, Seattle, WA).

Jenkins, O. J. T. and Savage, S. B. (1981) "The Mean Stress Resulting From Interparticle Collisions in Rapid Granular Shear Flow". Proc. 4th Int. Conf. on Continum Models of Discete Systems, Stockholm, June.

Kinosita (1967) Compression of Snow at Constant Speed". Int. Conf. on Physics of Snow and Ice. Hokkaido University, Japan.

Lee, T. M. (1961) Note on Young's Modulus and Poisons Ratio of Naturally Compacted Snow and Processed Snow. USA CRREL Technical Note.

Lee, T. M. (1963) Method of Determining Dynamic Properties of Viscoelastic Solids Employing forced vibration. J. Appl. Physics, Vol. 34.

Mellor, M. (1963) Oversnow Transport. USA CRREE Report III - A4, 58 pp.

Mellor, M. and Hawks, I. (1972) "Deformation and Fracture of Ice Under Uniaxial Stress". Journal of Glaciology, Vol. 11, No. 61.

Mellor, M. (1974) A Review of Basic Snow Mechanics, International Symposium of Snow Mechanics, Grindelwald, Switzerland.

Mellor, M. (1976) The Engineering Properties of Snow. Journ. of Glaciology, Vol. 19, No. 81.

Napadensky, H. (1964) Dynamic Response of Snow to High Rates of Loading. USA CRREL Research Report 119.

Napadensky, H. (1964) Dynamic Response of Snow to High Rates of Loading. USA CRREL RR. 119.

Nunziato, J. and Walsh, E. (1978) One Dimensional Shockwaves in Uniformly Distributed Granular Materials. Int. J. Eng. Sci., Vol. 14.

St. Lawrence, W. F. and Bradley, C. C. (1974) The Deformation of Snow in Terms of a Structural Mechanism. Snow Mechanics Proceedings of the Grindelwold Conference. IAHS-AISH Pub. No. 114.

St. Lawrence, W. F. and Bradley, C. C. (1977) Spontaneous Fracture Invitation in Mountain Snowpacks. J. of Glaciology, Vol. 19, No. 81.

Salm, B. (1974) A Constitutive Equation for Creeping Snow. Proceedings of the Grindelwald Symposium on Snow Mechanics, Grindelwald Switzerland, IAHS-AISH Publication No. 114.

Salm, B. (1981) A Review of Mechanical Properties of Snow. (To appear in Reviews in Geophysics and Space Physics).

Snell, R. F. and others (1973). An Electromagnetic Plane Stress Wave Generator. Experimental Mechanics Vol. 13, No. 11.

Spence, D. A. (1974) Nonlinear Wave Propagation in Viscoelastic Materials. Nonlinear Elasticity, (R. W. Dickey, ed.) Pg. 365.

Wekahama, G. and Sato, A. (1977) Propagation of a Plastic Wave in Snow. J. of Glaciology, Vol. 19, No. 81.

Wistoski, J. and W. Snyder (1966). A Study of the Effects of Snow Cover on High Explosive Blast Parameters. University of Denver, Denver Research Institute Report 2303.

Yong, R. N. and W. L. Harrison (1978) On Vehicle Mobility in Snow Covered Terrain. Journal of Terramechanics Vol. 15, No. 4.

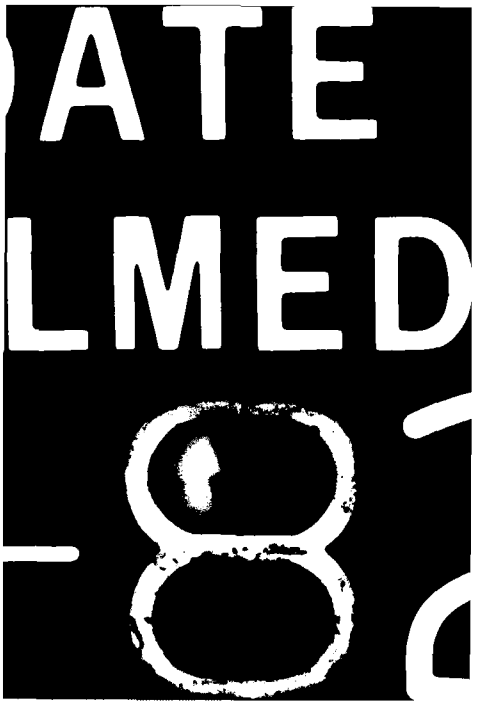
ATE
LMED